2015

Compact Quiescent Galaxies in the DEEP2 Redshift Survey

Kirsten N. Blancato
Wellesley College, kblancat@wellesley.edu

Compact Quiescent Galaxies in the DEEP2 Redshift Survey

by

Kirsten N. Blancato

Submitted to the Departments of Astronomy and Physics
in partial fulfillment of the requirements for

Honors in Astrophysics

at

WELLESLEY COLLEGE

May 2015

Advisors:

Igor Chilingarian
Harvard−Smithsonian Center for Astrophysics

Kim McLeod
Wellesley College Department of Astronomy

Compact Quiescent Galaxies in the DEEP2 Redshift Survey

by

Kirsten N. Blancato

Submitted to the Departments of Astronomy and Physics
in May 2015, in partial fulfillment of the
requirements for
Honors in Astrophysics

Abstract

Compact quiescent galaxies in the redshift range $0.5 < z < 1.1$ are the missing link needed to complete the evolutionary histories of these objects from the high-redshift $z \geq 2$ Universe to the local $z \sim 0$ Universe. We identify a sample of 52 intermediate-redshift compact quiescent galaxies, with sizes at most half of the size of their $z \sim 0$ counterparts of the same mass, by searching the DEEP2 Redshift Survey in conjunction with derived spectroscopic and structural properties. The compact quiescent galaxies have half-light radii ranging from $0.45 \leq R_{e,c} \leq 5.01$ kpc (mean $R_{e,c} = 1.62$ kpc) and dynamical masses ranging from $1.20\times10^{10} \leq M_{dyn} \leq 2.45\times10^{12}$ $M_{\odot}$ (mean $M_{dyn} = 1.35\times10^{10}$ $M_{\odot}$). In addition to having structural properties that bridge the gap between their high- and low-redshift counterparts, our sample of intermediate-redshift quiescent galaxies spans a large range of ages but is drawn from two distinct epochs of star formation quenching: quenching at $z > 2$ which suggests these objects may be the predecessors of the observed high-redshift compact galaxies and quenching at $z \leq 2$ which suggests there is an additional population of more recently formed quiescent compact galaxies. Furthermore, initial comparisons of the stellar and dynamical masses of these compact quiescent objects suggest that a bottom-heavy initial mass function (IMF) is unphysical for these galaxies. This is in tension with recent IMF developments that claim the IMF for massive, early-type galaxies becomes increasing bottom-heavy as velocity dispersion increases.

Acknowledgments

First, I would like to thank my thesis advisor Igor Chilingarian for his guidance on this project over the past year despite his busy travel schedule. I am grateful to Kim McLeod not only for her support during the thesis process but also for her invaluable mentorship throughout my entire Wellesley career. I would also like to thank my committee members, James Battat and Kaća Bradonjić, for giving feedback on writing drafts and being sources of support and encouragement. Additionally, I am grateful to Sean Moran and Ivana Damjanov at the Harvard-Smithsonian Center for Astrophysics and Ivan Katkov at the Sternberg Astronomical Institute of Moscow University for their help on the more technical parts of the project. I would also like to thank Casey Pattanayak, director of the Wellesley Quantitative Analysis Institute, for discussing the statistics of this project with me.

I am forever grateful to all my friends that have made Wellesley into a home. I'm especially thankful to Alison Nikyar, Ornela Xhori, and Sydney Butler for their love and support over the past four years - I could not have done it without you. Special thanks to Eunice Paik and Aiman Sherani for being my thesis buddies and becoming great friends along the way. You have kept me sane this year and made the process of applying to graduate school and thesising much more enjoyable. I would also like to thank Rose Gibson for her encouragement these past few months.

Lastly, I owe everything to my mother who has always been my best friend and greatest inspiration. Her combination of strong-will and open mindedness has gotten me to where I am today. This thesis and degree are just as much her accomplishments as they are mine.

Contents

Chapter 1

Introduction

1.1 The Structure of the Universe

Galaxies are the fundamental components of the Universe's structure. Made up of gravitationally bound dust, gas, stars, and dark matter, galaxies are the largest and most diverse objects in the Universe. Over the past few decades, redshift surveys have revealed that the spatial distribution of galaxies in the Universe is not uniform, with galaxies clustering into patterns of filaments and voids on the scale ten thousand times larger than the size of our own galaxy. Figure 1-1 shows slices of the three-dimensional distribution of galaxies obtained from the Sloan Digital Sky Survey (SDSS), the 2-degree Field Galaxy Redshift Survey (2dFGRS), and the Center for Astrophysics (CfA) galaxy redshift survey, which together have probed large-scale structure out to redshift $z \sim 0.2$, which corresponds to a distance of $\sim$800 Mpc[1] [Springel et al., 2006]. The leading paradigm for how large-scale structure emerged from the seemingly uniform energy distribution of the early Universe revealed by the cosmic microwave background involves small matter density fluctuations that, through the complex interaction between baryonic and dark matter, eventually evolved into the structure of the Universe observed today. While there are still many unanswered questions about the large-scale structure of the Universe, simulations of large-scale structure

[1]Throughout this work, a ΛCDM cosmology is assumed with $H_0 = 70$ km s^{-1} Mpc^{-1}, $\Omega_\Lambda = 0.7$, and $\Omega_M = 0.3$ [Bennett et al., 2013]. Additionally, magnitudes are listed in the AB system.

from the Millennium Run, which evolved the distribution of over ten billion dark matter particles over 13 billion years, have proved to match the observed distribution of galaxies quite well [Lemson and Virgo Consortium, 2006]. From these simulations, cosmological models describing the geometry and type of matter in the Universe have been developed and refined.

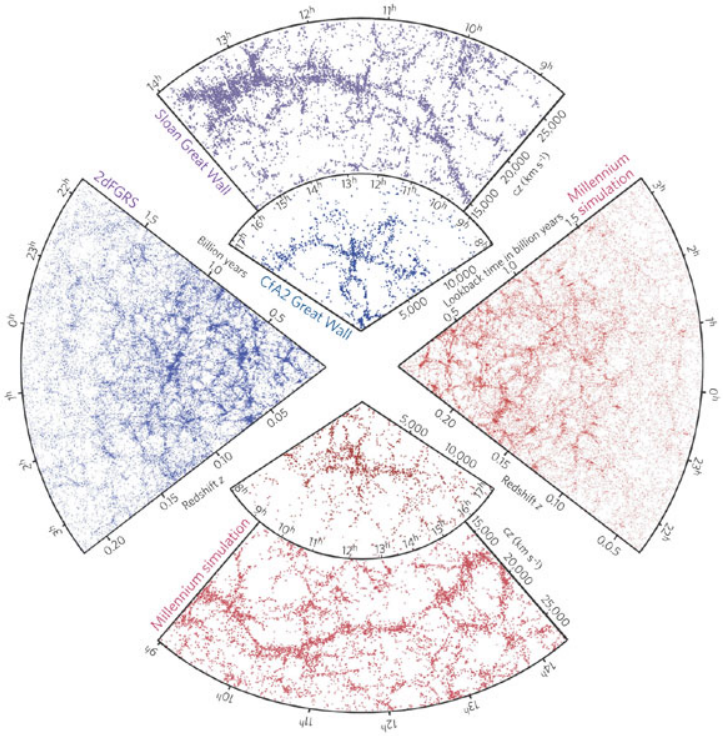

Figure 1-1 Observed and modeled distribution of galaxies in the Universe out to a redshift of $z \sim 0.2$ [Springel et al., 2006]. The top and left panel show the observations of galaxy spatial distribution from the SDSS, CfA, and 2dFGRS surveys while the bottom and right panels show simulated large-scale structure from the Millennium Run.

As the luminous tracers of large-scale structure, galaxies and the study of their observable properties are crucial to understanding the evolution of the Universe. By studying how galaxies form and evolve we can probe the physical processes that govern the formation and evolution of large-scale structure. While the Gigayear (Gyr) timescale of galaxy evolution is much larger than can be observed in real-time, we can exploit the finite speed of light to infer how populations of galaxies change throughout

cosmic time by relating their properties at different redshifts. The redshift, z, is a function of the distance which, because the speed of light is finite, allows us to observe the Universe as it appeared earlier in history. So galaxies observed at higher redshifts appear as they were in the early Universe and galaxies observed at lower redshifts appear as they are in the more recent Universe.

1.2 Galaxy Morphology and Properties

It is currently estimated that there are at least 100 billion galaxies in the observable Universe, but in the early 1900s our view of the cosmos consisted solely of the Milky Way. While the theoretical beginnings of modern cosmology were underway, there was not yet observational evidence of a Universe beyond our own galaxy. Using the Hooker telescope on Mount Washington, Edwin Hubble observed small patches of dust, termed nebulae, that most believed to be a part of the Milky Way. But by observing a Cepheid variable star, which is a standard candle, in the dust patch now known as the Andromeda galaxy Hubble was able to prove that this dust patch was far beyond the reaches of the estimated size of the Milky Way. Hubble's observation marked an important milestone in the birth of extragalactic astronomy and observational cosmology.

For the rest of his career Hubble observed numerous galaxies and established a classification scheme based on their appearance. His scheme, the Hubble sequence, divides galaxies into three distinct classes: elliptical, lenticular, and spiral. Figure 1-2 shows his classical 'tuning-fork' of galaxy morphology. Elliptical galaxies, characterized as smooth spheroids, are depicted on the left increasing in degree of ellipticity. At the node of the fork is a lenticular galaxy which is a class of transitional galaxy between elliptical and spiral. Spiral galaxies branching off into normal and barred types are shown on the left arranged by the tightness of their spiral arms. The interpretation of the Hubble Sequence as an evolutionary scenario led to the misnomer of elliptical galaxies being named early-type and spiral galaxies named late-type. As will be discussed in Section 1.3, this naming scheme is actually the opposite of what

has become the currently understood scenario of galaxy evolution.

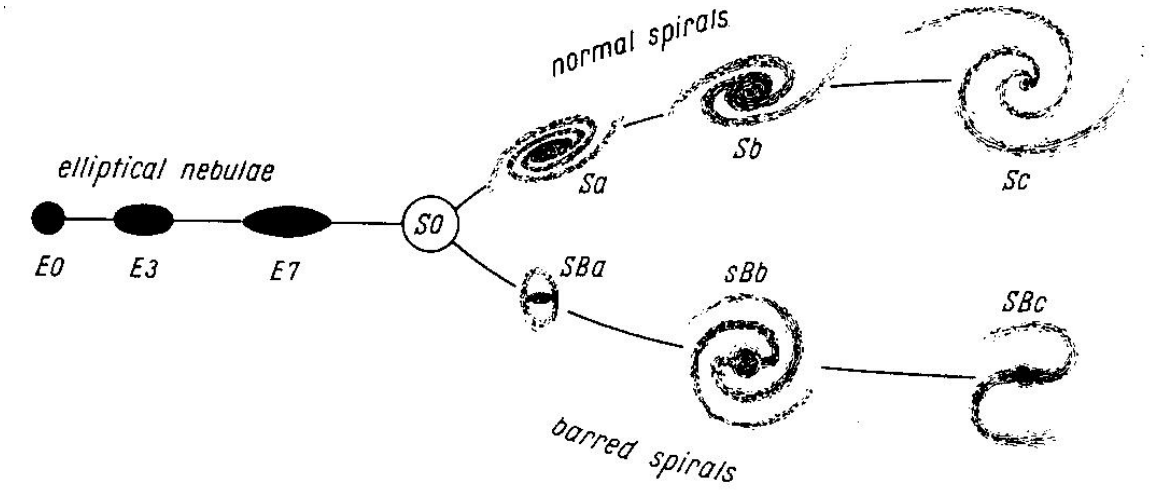

Figure 1-2 The Hubble tuning-fork of galaxy morphology [Hubble, 1936]. Early-type, elliptical galaxies are shown on the left and late-type, spiral galaxies are shown on the right. Figure from [Hubble, 1958].

Since Edwin Hubble's classifications, our knowledge of the different types of galaxies in the Universe has certainly broadened, and not all galaxies fall neatly into the categories Hubble sequence. As shown in Figure 1-3, galaxies are observed to have a wide range of morphologies with some galaxies falling into the Hubble sequence and others more irregular. Large observing programs such as the ground-based Sloan Digital Sky Survey (SDSS) have permitted detailed studies of thousands of galaxies in the local Universe with a mean redshift of $z \sim 0.1$. Observed galaxy properties, including color, luminosity, stellar mass, and star formation rate scale with Hubble classification, making the Hubble sequence and continued study of galaxy morphology still relevant.

Space telescopes such as the Hubble Space Telescope (HST) have also imaged thousands of galaxies with great resolution and have aided in studying galaxies properties, in a statistical sense, out to $z \sim 2$. But at higher redshifts, the morphology of galaxies becomes increasingly irregular suggesting that the more distinct morphological categories observed in the local Universe is something that the galaxy population evolved into over time. The continued study of galaxy morphology and properties

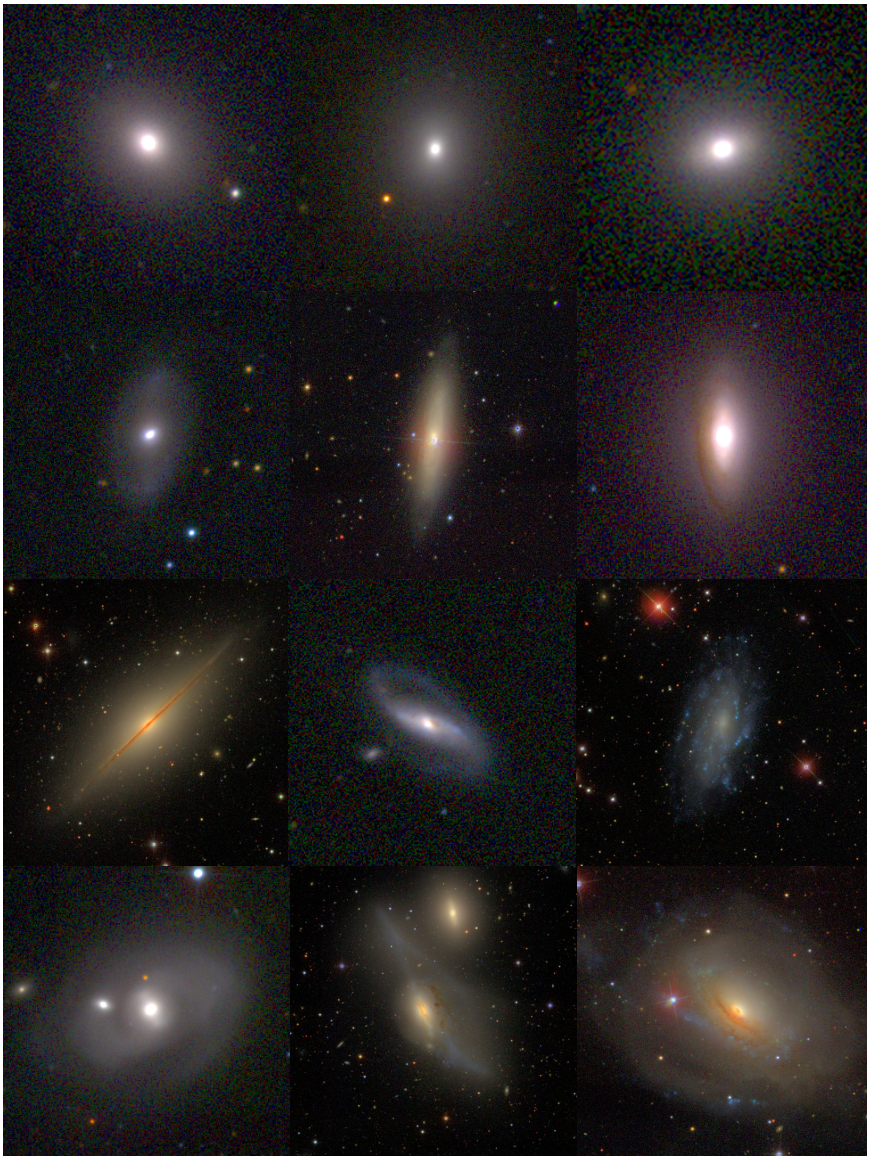

Figure 1-3 SDSS images of various galaxy types. The top row is of early-type galaxies NGC 0391, NGC 0155, and NGC 0219, the second row shows lenticular galaxies UGC 00386, NGC 0676, and NGC 2562, the third row shows various late-type galaxies NGC 7814, NGC 0291, and NGC 2541 and the last row shows irregular galaxies NGC 4795, NGC 4438, and NGC 3169. Images are taken from the NASA/IPAC Extragalactic Database.

at high-redshift will provide clues to how galaxies and the Universe evolved. In the near future, the planned James Webb Space Telescope (JWST), with a launch date of October 2018, will allow comprehensive studies of galaxy properties out to $z \sim 4$ corresponding to a Universe age of 1.5 Gyrs.

1.3 Early-type Galaxies

The subject of this thesis are early-type, elliptical galaxies. Initially, early-type galaxies were thought to be the simplest of the three main morphology classes due to their smooth appearance. But elliptical galaxies have turned out to be quite diverse and complex systems. Early-types galaxies are characterized by observable properties such as their the surface brightness profiles, kinematics, and stellar populations.

1.3.1 Structural Properties

The total luminosity of a galaxy is given by $L_{tot} = 2\pi \int_0^\infty I(r) r dr$ where $I(r)$ is the two-dimensional surface brightness profile typically measured in units of luminosity per unit area. The two-dimensional surface brightness profile describes how the intensity of light emitted from a galaxy changes as a function of position from the center of the galaxy. Early-type galaxies display varying degrees of ellipticity so radius r is the elliptical radius $(x^2 + (y/q)^2)^{1/2}$. The axis ratio, q, is given by a/b where a is the major axis and b the minor axis.

The two-dimensional surface brightness profile, $I(r)$ of an elliptical galaxy follows de Vaucouleurs' law,

$$I(r) = I_e e^{-7.669[(\frac{r}{r_e})^{1/4} - 1]}, \tag{1.1}$$

where I_e is the brightness at the half-light radius r_e [de Vaucouleurs, 1948]. The half-light radius, which is the radius containing half the total flux of the galaxy, is used to characterize a galaxy's size. Sizes of early-type galaxies typically range from a

fraction of a kiloparsec to tens of kiloparsecs[2]. As we will discuss in Chapter 3, the size of a galaxy can be measured from its image.

1.3.2 Kinematics

The stars that make up an early-type galaxy have random orbits, and thus overall the galaxy has little net rotation. The distribution of stellar velocities closely follows a Gaussian, $N(\nu) \propto e^{-\nu^2/2\sigma^2}$, where N is the number of stars at velocity ν relative to the galaxy center. The standard deviation σ of the distribution of star speeds is the velocity dispersion which is a fundamental and important property of early-type galaxies. As we discuss in Chapter 2, the velocity dispersion can be measured from the spectra of a galaxy.

While the mass of an early-type galaxy is unobservable, it can be derived from the virial theorem using the galaxy's size and velocity dispersion. As explained in [*Galaxy Formation and Evolution*, Ho 2010] the virial theorem, $2\langle T\rangle = -\langle U\rangle$, relates the time average kinetic energy T of a system to its time average potential energy U for a system with a stable moment of inertia. Under a few assumptions the virial theorem can be used to derive the dynamical mass, a measure of the gravitational mass, of early-type galaxies. The kinetic energy can be approximated under the assumptions that the stars in the galaxy are identical with equal masses and that their motion is isotropic. The velocity dispersion for all the stars that make up the system is $\sigma^2 = (1/N)\sum_i \nu_{i,LOS}^2$ where N is the total number of stars and $\nu_{i,LOS}$ is the line-of-sight velocity of each star. Thus, under the assumption that the motion of the stars is the same in all directions, the average kinetic energy of the system can be written as,

$$\langle T\rangle = \frac{3}{2}\frac{\mathrm{M}}{N}\sum_i \langle \nu_{i,LOS}^2\rangle = \frac{3\eta}{2}\mathrm{M}\sigma^2, \tag{1.2}$$

where M is the total mass of N identical stars and η is a constant determined by the specifics of the stellar population. The potential energy can be approximated by

[2] 1 kiloparsec (kpc) = 3.09×10^{19} m

assuming the system is in net equilibrium and the distribution of stellar masses is smooth. Under these two assumptions the potential energy of an early-type galaxy is approximated to be,

$$\langle U \rangle = -\alpha \frac{G\mathrm{M}^2}{\mathrm{R}} \tag{1.3}$$

where α is a constant determined by the density profile of the galaxy, R is the radius of the galaxy, and G Newton's gravitational constant. Using the virial theorem and combining Equations (1.2) and (1.3), the virial mass of an early-type galaxy is estimated to be,

$$\mathrm{M}_{\mathrm{dyn}} = \beta \frac{\sigma^2 \mathrm{R}}{G}, \tag{1.4}$$

with $\beta = (3\eta)/(4\alpha)$ being a constant that depends on the specific arrangements of the system being considered. As we will discuss in Chapter 4, the dynamical mass is the gravitational mass contained within the optical radius of the velocity dispersion measurement.

1.3.3 Stellar Populations

As galaxies are collections of stars, the properties of the underlying stellar population of a galaxy are fundamental to the overall characteristics exhibited by a galaxy. Early-type galaxies are composed mainly of stars and contain little dust and gas. In the 1930s, Annie Jump Cannon qualitatively classified over 400,000 stellar spectra based upon the ratios of absorption and emission lines. She created the classification scheme still in popular use today: OBAFGKM, which turns out to be arranged in order of decreasing temperature with O-type stars being the hottest (40,000K) and M-type stars being the coolest (3,000K). Cooler stars have many metal absorption lines while hotter stars have few metal absorption lines. This is due to hotter stars completely ionizing most metal atoms, while cooler stars may only singly ionize metal atoms.

Spectra can further be classified into luminosity classes based on spectral emission line ratios. The basic Yerkes scheme classifies stars into four main categories: dwarfs,

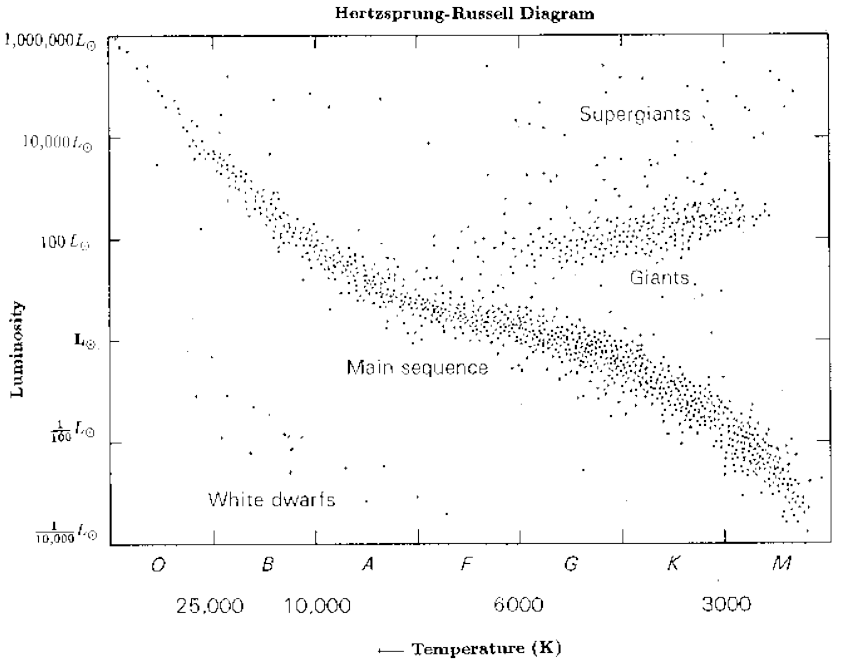

Figure 1-4 Hertzsprung-Russell diagram showing the relation between luminosity, surface temperature, and spectral class of stars. (Image credit: http://casswww.ucsd.edu/archive/)

main sequence, giants and supergiants, which corresponds to the stellar evolutionary track. Dwarf stars are the least mature stars while supergiants are stars farther along in their lifetime. Figure 1-4 shows the Hertzsprung-Russell (HR) diagram which displays how luminosity, surface temperature, and spectral class of stars are related. The different Yerkes stellar classifications are separated into distinct regions of the HR diagram.

The light from early-type galaxies primarily comes from red giant, K-type stars. Most early-type galaxies are often referred to as "red and dead" because the light from K-type stars peaks in the red part of the electromagnetic spectrum and a majority of their stars have evolved past the main sequence. Some early-type galaxies, called "young post-starbursts" have recently ended a period of active star formation and in addition to red giant K-type stars contain younger and hotter O- and B-type stars. As the stars in post-starburst, early-type galaxies continue to evolve, they become dominated by A-type supergiant stars (E+A type galaxies). When there is no longer

evidence of new star formation, a galaxy is considered to be quiescent ("dead"). In Chapter 2 we discuss how stellar populations of early-type galaxies give rise to their observed spectral characteristics.

1.4 Galaxy Evolution

Based on galaxy morphology beyond the local Universe, a paradigm of galaxy evolution has emerged but still leaves many unanswered questions. Prior to the current scenario of galaxy evolution, there were two opposing theories of evolutionary mechanisms for early-type galaxies: monolithic collapse and hierarchical merging. In the monolithic collapse scenario, galaxies form from the collapse of primordial gas as stars are made and subsequently evolve in isolation [Eggen et al., 1962]. The initial conditions of the dark matter halo of the galaxy are what influences its formation and evolution. On the other hand, in the hierarchical merging scenario, stars form only in the disks of late-type galaxies that eventually merge together to form quiescent elliptical galaxies [Toomre, 1977]. Two disk-type galaxies interact, merge, and eventually form a larger spheroidal-type galaxy. As the two disk galaxies begin to interact, star formation is induced from the compression of gas. The gas then falls towards the center of the merging galaxy, feeding the central black hole and creating an active galactic nucleus. After the two disk galaxies coalesce, all merging features disappear and a single spheroidal-type galaxy remains. Thus, it is expected that disk type galaxies and mergers were more common in the higher density early Universe and elliptical galaxies are more common in the local Universe. The difference between these two evolution scenarios is the prominent "nature versus nurture" debate of galaxy formation and evolution.

While the original nature versus nurture debate of galaxy evolution is still an open question of galaxy evolution, a general picture of galaxy evolution that is a mixture of both monolithic collapse and hierarchical merging is beginning to surface. The continued study of the properties of elliptical galaxies throughout the history of the Universe is essential for piecing together a coherent picture of galaxy evolution. There

are still many unanswered questions and puzzles concerning the complex evolution of early-type galaxies.

1.5 Compact Quiescent Galaxies

Massive ($M \geq 10^{10}$ $M_{\odot}$)[3] quiescent galaxies continue to challenge the prevailing scenarios of galaxy evolution. Observations of high-redshift early-type galaxies (ETGs) near $z \sim 2$ have shown that at least 50% of quiescent massive galaxies are compact [Szomoru et al., 2012, van Dokkum et al., 2008]. Figure 1-5 shows the mass-size distribution of a sample of high-redshift galaxies ($1.5 < z < 2.5$) from [Szomoru et al., 2012]. Larger galaxies that fall above the upper dashed line are late-type spiral galaxies, while galaxies that fall below the solid relation are early-type galaxies. Normal massive ETGs fall between the dashed lines while the ETGs below the dashed line are compact. A majority of compact early-type galaxies are quiescent, denoted by a red cross in Figure 1-5.

These compact quiescent galaxies (CQGs), characterized by small effective radii, high velocity dispersions, and little to no evidence of active star formation were first discovered at $z \geq 1.4$ and initially had no known similarly compact counterparts in the local (z$\sim$) Universe [Daddi et al., 2005]. In addition, recent studies have described the properties of even more $z \geq 1$ compact galaxies [Belli et al., 2014, van de Sande et al., 2013, Bezanson et al., 2012, Onodera et al., 2012, Toft et al., 2012, Newman et al., 2010, van Dokkum et al., 2009, van der Wel et al., 2008, Trujillo et al., 2006], CQGs have now also been confirmed to exist at lower redshifts in the range $0.2 < z < 0.6$. CQGs in the more local Universe have been found in the Sloan Digital Sky Survey (SDSS) dataset [Damjanov et al., 2013, Damjanov et al., 2014]. Initially thought to be stars, they were discovered under further inspection of the spectra, which confirmed them to be CQGs. A small number of CQGs have also been found in the local, $z \sim 0$ Universe [Trujillo et al., 2009, Taylor et al., 2010, Ferré-Mateu et al., 2012]. The discovery and characterization of CQGs in the redshift range $0.5 < z < 1.1$, from an

[3] $M_{\odot} = 1.99 \times 10^{30}$ kg, the mass of the Sun

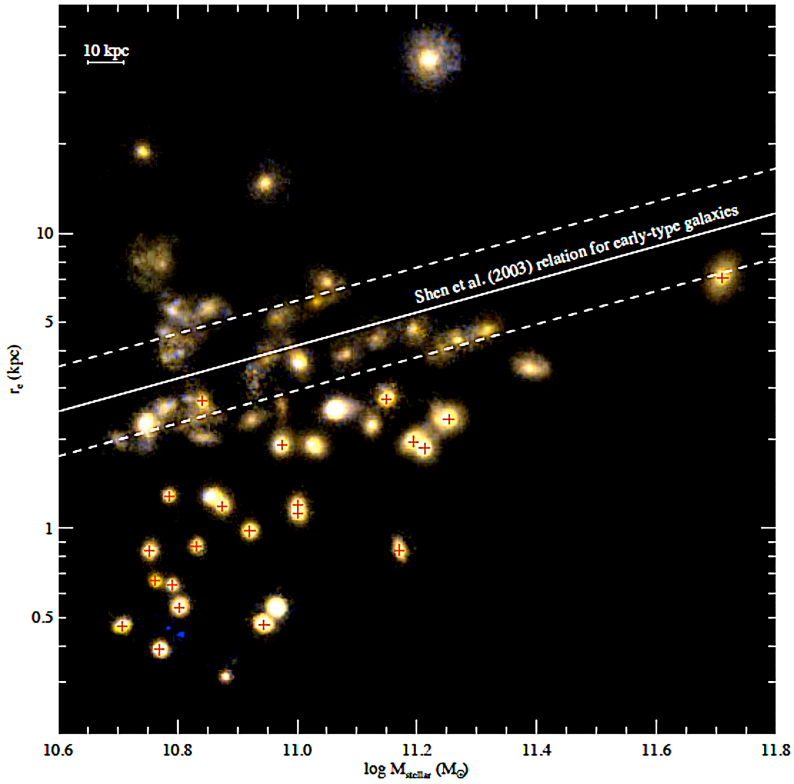

Figure 1-5 Size against mass for a sample of $1.5 < z < 2.5$ galaxies from [Szomoru et al., 2012]. Galaxies marked with red are quiescent.

age of the Universe from 5.4 to 8.4 Gyrs, will be necessary to bridge the observational gap for a comprehensive evolutionary study of ETGs beginning from their formation in the high-redshift Universe and ending in their current state in the local Universe.

1.5.1 Evolution of Massive Early-type Galaxies

Observations have shown that there is a size evolution of massive quiescent galaxies, with the high-redshift objects being 2 - 5 times smaller than their massive quiescent ETG counterparts in the local Universe [Damjanov et al., 2009, Buitrago et al., 2008, Strazzullo et al., 2010, Cassata et al., 2011, Cimatti et al., 2008, Bruce et al., 2012, Szomoru et al., 2012, Carrasco et al., 2010, Saracco et al., 2011]. This is puzzling because somehow these galaxies grow in size while remaining passive and not undergoing any new star formation. The mechanism responsible for this size evolution remains an

open question whose answer will provide insight into the field of galaxy evolution as a whole. As discussed in [Damjanov et al., 2014], the most widely accepted evolution scenario that explains the observed size increase of compact quiescent objects throughout cosmic time involves individual quiescent galaxies expanding through a number of dry (gas-poor) minor mergers [Oogi and Habe, 2013, van der Wel et al., 2009, Oser et al., 2012, Naab et al., 2009, López-Sanjuan et al., 2012]. The mergers increase the size of the size of the galaxy without the formation of new stars.

To corroborate the minor merger theory of size evolution, the fraction of massive quiescent galaxies is expected to decrease with time as quiescent objects merge with one another and form a smaller total number of larger quiescent objects. Results from semi-analytic models based on the Millennium Simulation project, which simulated the evolution of nearly twenty million galaxies [Lemson and Virgo Consortium, 2006, Quilis and Trujillo, 2013], show that a large majority of massive quiescent objects at $z > 2$ must be compact and a significant number of massive quiescent objects in the range $0 < z < 2$ must be compact as well. Observations of high-redshift galaxies near $z \sim 2$ have shown that at least 50% of quiescent massive galaxies are indeed compact [Szomoru et al., 2012, van Dokkum et al., 2008], but observations of the number density of compact quiescent systems in the local Universe are varied. Some studies report number densities much higher than the Millennium predictions [Poggianti et al., 2013] while other studies are reporting densities well below the predictions [Taylor et al., 2010, Trujillo et al., 2009].

To further piece together the evolutionary history of compact quiescent galaxies, several studies have focused on tracing the formation of high-redshift, $1 \leq z \leq 2$ massive quiescent galaxies by searching for and characterizing their progenitors at $z > 2$ [Toft et al., 2014, Williams et al., 2014, Marchesini et al., 2014]. As discussed in [Toft et al., 2014], while minor merging is believed to be the main mechanism driving the evolution of these objects, recent studies suggest that other mechanisms play a larger role than previously thought [Krogager et al., 2014, Newman et al., 2012, Carollo et al., 2013]. One such scenario involves a gas-rich major merger that induces nuclear star formation as the two objects coalesce. As gas is driven towards the cen-

ter, the generated active galactic nucleus (AGN) quenches star formation resulting in a compact, quiescent bulge [Naab et al., 2007, Naab et al., 2009, Sanders et al., 1988, Wuyts et al., 2010, Hopkins et al., 2006]. While sub-millimeter galaxies (SMGs), characterized by extreme starburst activity masked by dust, are the leading progenitor candidate of quenched, gas-rich major mergers [Coppin et al., 2008, Schinnerer et al., 2008, Blain et al., 2004, Tacconi et al., 2006, Toft et al., 2007, Cimatti et al., 2008], the epochs of formation for these objects are still being investigated. Recently, studies have shown that there are a number of SMGs that formed between $3 \leq z \leq \sim 6$, rendering them possible progenitors of the massive, compact quiescent galaxies we observe at $z \sim 2$ [Toft et al., 2014, Cappellari et al., 2009, Capak et al., 2008, Carilli et al., 2010, Combes et al., 2012, Riechers et al., 2010, Yun et al., 2012].

1.5.2 Constraining the Initial Mass Function

In addition to constraining models of galaxy evolution, the study of compact quiescent objects also has the potential to refine initial mass function (IMF) models. The IMF, $\xi(M)$, which is widely assumed to be universal for all newly formed stellar populations, describes the fraction of stars ξ at different masses in a newly formed population. The IMF is a power law,

$$d\xi(M) \propto \begin{cases} dM^{-x_1} & , \mathrm{M} < 0.5 \ \ \mathrm{M}_\odot \\ dM^{-x_2} & , \mathrm{M} \geq 0.5 \ \ \mathrm{M}_\odot \end{cases} \tag{1.5}$$

that describes the number of stars in a population that are within a mass range dM. The slopes of the IMF, x, determines whether the stellar population is more "bottom-heavy" or "top-heavy". The mass of a bottom heavy IMF, described by larger values of x, is dominated by a larger number of low mass stars. The mass of top-heavy IMF, described by smaller values of x, is dominated by the fewer number of high mass stars. The uni-modal Salpeter IMF with x=2.35 [Salpeter, 1955] and the bi-modal Kroupa IMF with $x_1 = 1.3$ and $x_2 = 2.3$ [Kroupa, 2002] are the most commonly adopted universal IMFs.

Recent IMF studies are revealing that a universal IMF is not an accurate descrip-

tion of the stellar populations of massive, early-type galaxies [Cappellari et al., 2012, Conroy et al., 2013]. The universal Salpeter and Kroupa IMFs are both based on studies of stellar populations in the Milky Way and have shown little evidence of IMF variation. But as presented in [Cappellari et al., 2012, Conroy et al., 2013], there is evidence to support that the IMF becomes increasingly bottom-heavy as the velocity dispersion and mass of early-type galaxies increases. There are many systematic uncertainties in measuring the IMF, but compact quiescent objects are proving to be the most promising stellar systems to study to reduce some of these uncertainties because they are believed to have little to no dark matter at their centers, based on the fact that their stellar masses equal their dynamical masses within the optical radius. As discussed in [Conroy et al., 2013], if these objects were to have dark matter content that rivaled the mass of the stellar population, a significant modification to the NFW dark matter density profile[4] would have to be made. Thus, the dark matter deficiency of CQGs introduces a constraint on the allowed values of the IMF slope because it would be unphysical for these galaxies to have dynamical masses lower than their stellar masses.

1.6 Outline of Thesis

For this thesis, we search for compact quiescent galaxies in the DEEP2 Redshift Survey and derive their structural and stellar properties to begin to bridge the evolutionary gap between these objects and their low- and high-redshift counterparts. We present the properties of 52 CQGs by inspecting quiescent early-type galaxies in the redshift range $0.5 < z < 1.1$. In Chapter 2 we describe the observables of galaxies, the DEEP2 Redshift Survey and our initial selection of massive, quiescent early-type galaxies. Chapter 3 describes the existing structural properties of our sample and explains the methods for performing our own size measurements on the remaining sample with available HST imaging. In Chapter 4 we pull in a comparison sample

[4]Navarro-Frenk-White (NFW) dark matter density profile as a function of radius from the center of a galaxy is described by $\rho(r) = \rho_0[(r/r_s)(1+(r/r_s))^2]^{-1}$ where ρ_0 is the critical density and r_s is the characteristic radius.

of SDSS local early-type galaxies that we use to place a compactness criterion on the quiescent early-type DEEP2 galaxies. We identify 52 CQGs, derive their stellar masses, evaluate their properties, and compute their redshifts of star formation quenching. In Chapter 5 we discuss preliminary work relating to the dynamical and stellar mass comparison of CQGs and summarize the findings of this thesis.

Chapter 2

Searching for Quiescent ETGs in DEEP2

2.1 Observations of Galaxies

The only way we can observationally study the properties of early-type galaxies described in Chapter 1 is by studying the light they emit. Spectroscopy and photometry are two critical astronomical techniques that use light to study the properties of galaxies.

2.1.1 Spectroscopy

The spectroscopic redshift, velocity dispersion, and stellar properties of a galaxy can be derived from its spectrum. The spectroscopic redshift of a galaxy is found by measuring the wavelength shift of known rest-frame emission or absorption lines. The velocity dispersion σ of an early-type galaxy, described in Section 1.2.1, is measured from the Doppler broadening of the spectral lines. Additionally, since the spectrum of a galaxy is the superposition of the spectra of the stars it contains, the properties of the underlying stellar population of a galaxy can be probed to determine the overall age and metallicity [Z/H] of a galaxy.

Figure 2-1 shows three galaxy spectra: a typical red and dead early-type spectrum,

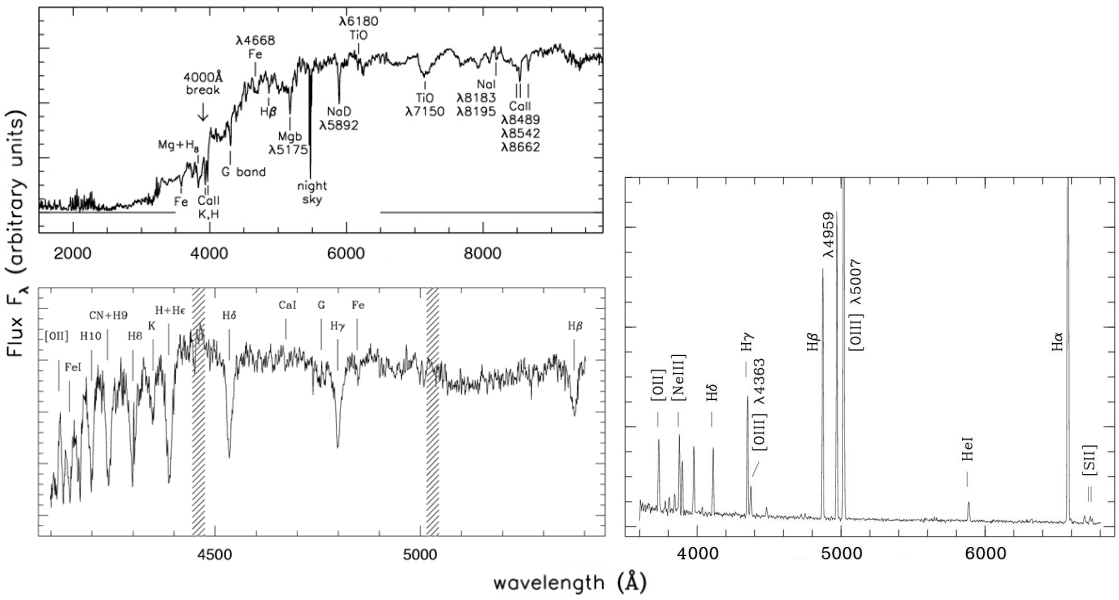

Figure 2-1 The upper left spectrum is of a typical "red and dead" early-type galaxy while the lower left spectrum is of a young post-starburst quiescent elliptical galaxy [A. Kinney "Galaxies in the Universe"]. The spectrum on the right of a late-type galaxy shows emission lines indicative of active star formation [Kniazev et al., 2002].

a quiescent young post-starburst spectra, and a late-type emission spectrum with common emission and absorption lines are labeled in each. There are two main types of quiescent ETG spectra: (1) old red galaxies, that exhibit the characteristic 4000 Å break due to the lack of hot O+B type stars, calcium H+K $\lambda\lambda$4934,3969 absorption lines, and G-band λ4304 absorption features and (2) young, bluer post-starburst galaxies, that indicate recent conclusion of star formation with their spectra displaying strong Balmer absorption lines but no strong emission. The spectra of young, post-starburst galaxies eventually evolve into the spectra of red and dead early-type galaxies.

Emission lines in a galaxy spectrum arise from the interstellar gas and dust being ionized by star formation. The right spectrum in Figure 2-1 shows a galaxy with emission lines indicative of star formation. From the emission line information the star formation rate (SFR) of a galaxy can be computed. The lack of emission lines in a galaxy spectrum indicates that the galaxy is quiescent and not undergoing active

star formation.

2.1.2 Photometry

Photometry is another essential tool for studying the light from galaxies. Imaging of galaxies by CCDs is not only useful for determining morphological characteristics (as will be discussed in Chapter 3), but also necessary for probing the stellar content and colors of galaxies. The light coming from an astronomical object is typically measured in several different filters using instrumentation that is optimized for the specific wavelength regime. Unlike stars, galaxies are extended objects so measuring their total flux requires integrating the surface brightness over the extent of the galaxy (as discussed in Section 1.3.3).

Photometric measurements are often reported in the magnitude system. The absolute magnitude M, which is a measure of the intrinsic brightness of an object, is computed from,

$$M = m - kcorr - 5(1 + \log_{10} D_L), \tag{2.1}$$

where m is the apparent magnitude of the object as measured from Earth, $kcorr$ is the K-correction to the magnitude, and D_L is the luminosity distance in parsecs. The apparent magnitude is what we measure photometrically, the K-correction corrects for the object's redshift (discussed in Section 2.4), and the luminosity distance is discussed in the following section.

2.1.3 Distance Measurements

Interpretations of measurements of distant galaxies must take into account the expansion of the Universe. The angular diameter distance D_A is the ratio of a galaxy's physical size to its angular size. To determine the physical size of our DEEP2 galaxies, as done in Chapter 3, we can measure the angular size of the galaxy from an image and compute the angular diameter distance. As explained in [Hogg, 1999], the angular diameter distance to an object, $D_A = r(\chi)(1 + z)^{-1}$, depends on the trans-

verse comoving distance χ. The factor $r(\chi)$ is determined by the chosen cosmology in the following way:

$$r(\chi) = \begin{cases} \sinh(H_0\chi\sqrt{\Omega_k})/(H_0\sqrt{|\Omega_k|}) & \Omega_k > 0 \\ \chi & \Omega_k = 0 \\ \sin(H_0\chi\sqrt{-\Omega_k})/(H_0\sqrt{|\Omega_k|}) & \Omega_k < 0 \end{cases} \tag{2.2}$$

where $\Omega_k = 1 - \Omega_\Lambda - \Omega_M$ is the curvature density and H_0 the Hubble constant.

In addition to correcting the physical sizes of our galaxies to account for the expansion of the Universe, we need to correct our measured luminosities obtained from photometry discussed in Section 2.4. The luminosity distance D_L determines what the absolute flux of the object is for a given observed flux of an object at redshift z. As discussed in [Hogg, 1999] the luminosity distance, $\mathrm{D}_L = [\mathrm{L}/(4\pi\mathrm{S})]^{1/2}$, is dependent on the bolometric luminosity L and bolometric flux S and is larger than the angular diameter distance D_A by a factor of $(1+z)^2$. Both the angular diameter distance and luminosity distance are needed to obtain the physical sizes and intrinsic luminosities of galaxies.

2.2 The DEEP2 Redshift Survey

2.2.1 Overview

In this study, we mine Data Release 4 (DR4) of the DEEP2 (Deep Extragalactic Evolutionary Probe) Galaxy Redshift Survey which covers 52,989 objects from $z = 0$ to $z \approx 1.4$ to a limiting apparent magnitude of $R_{\mathrm{AB}} = 24.1$ [Newman et al., 2013]. The DEEP2 Survey is the largest of its kind, probing galaxy properties, environments and large-scale structure at $z \sim 1$.

Based on the DEIMOS (DEep Imaging Multi-Object Spectrograph) spectrograph on the Keck II telescope over the course of ∼90 nights [Faber et al., 2003], the survey covers a total of 2.8 square degrees spread across four separate, rectangular fields as shown in Figure 2-2. A grating with 1200 line/mm and a central wavelength of 7800

Å was used to ensure the coverage of at least one prominent spectral feature for all objects in the range $0.0 < z < 1.4$. The typical wavelength range covered is 6500 Å - 9100 Å and the resulting resolution is R $\sim$ 6000 with slit width of $1''$.

2.2.2 DEEP2 Target Selection

The initial target pool for DEEP2 was composed by selecting objects from Canada-France-Hawaii Telescope (CFHT) *BRI* photometry based on magnitude, probable object type, and surface brightness criteria [Coil et al., 2004]. The first criterion limited the selection to those objects with R-band apparent magnitude between $R_{AB} = 18.5$ and $R_{AB} = 24.1$. With regard to object type, the selected objects included those with extended sizes and peculiar colors, as well as objects that have sizes similar to stars but have a high probability of being a galaxy determined by the methods described in [Coil et al., 2004]. Finally, the last criterion restricted the selection to those objects with surface brightness (SB) above the size-magnitude relation,

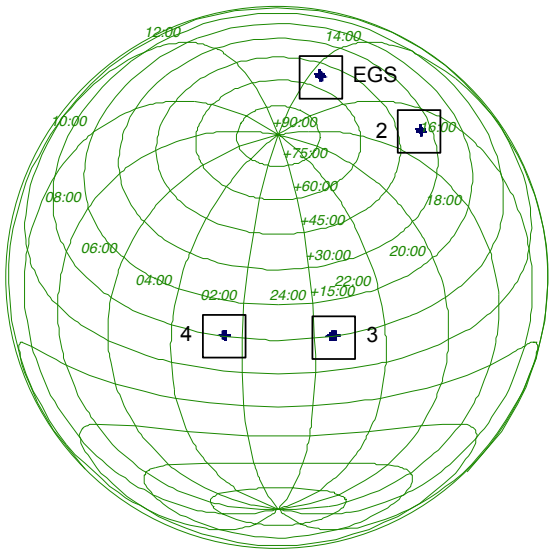

Figure 2-2 The four DEEP2 fields on the celestial sphere.

$$\mathrm{SB} = R_{AB} + 2.5\log_{10}[\pi(3r_g)^2] \;\leq\; 26.5, \tag{2.3}$$

where r_g is the Gaussian radius, determined by the 2D circular Gaussian fit to the object's image, in arcseconds. A majority of the low-SB objects excluded by this selection criterion are multiple objects that were misclassified as a single object in the CFHT photometry catalog.

Field 1, the Extended Groth Strip (EGS) field (Figure 2-3), was designed to cover

Table 2.1. Summary of DEEP2 Fields[†]

Field	α	δ	z selected	Area planned	Area completed	Masks planned	Masks completed	Objects covered
(1)	(2)	(3)	(4)	(5)	(6)	(7)	(8)	(9)
EGS	14:19	52:50	No	0.60	0.60	120	104	17745
2	16:52	34:55	Yes	0.93	0.62	120	85	10201
3	23:30	00:00	Yes	0.93	0.90	120	103	12472
4	02:30	00:00	Yes	0.93	0.66	120	103	12494

Note. — (1) DEEP2 field; (2) Right ascension of field center; (3) Declination of field center; (4) Objects selected to be $z > 0.7$; (5) Planned coverage area in square degrees; (6) Obtained coverage area in square degrees; (7) Planned number of slitmasks; (8) Obtained number of slitmasks; (9) Number of objects covered (including duplicates)

[†]Coverage information from [Newman et al., 2013]

$0°.25 \times 2°$ whereas Fields 2,3, and 4 (Figure 2-4) were designed to cover $0°.5 \times 2°$. The width of the EGS field is half of that of the other three fields due to the photometric redshift selection: galaxies with redshifts $z < 0.7$ (see below) were rejected in Fields 2, 3, and 4 but included in the EGS field. As described in [Newman et al., 2013], a single DEIMOS slitmask typically covers 130-150 objects and without excluding $z < 0.7$ galaxies using BRI photometry, the sample of $z \sim$1 galaxies obtained would be diluted. To keep the number density of high-redshift objects covered constant in all four fields, the width of the EGS field is halved. While the main target population of DEEP2 is $z \sim 1$ galaxies, observations in the EGS field were designed to preserve $z < 0.7$ galaxies to take full advantage of the field's extensive multi-wavelength HST coverage and to test the selection methods enforced in the other three fields.

Using CFHT BRI photometry, galaxies in Fields 2, 3, and 4 with $z < 0.7$ were removed based on their color, which reduced the percentage of galaxies brighter than $R_{AB} = 24.1$ to 45%. Redder galaxies display the significant 4000 Å break in their spectra, which produces a division in color-color space between galaxies. This redshift selection is found to increase the efficiency of covering $z \sim 1$ galaxies by a factor of 2.2. While low-redshift galaxies are not removed in the EGS field, galaxies that are nearby and faint are weighted less in the selection process. In each field, 60% of eligible objects had planned slitmask coverage. Table 1 summarizes the planned and

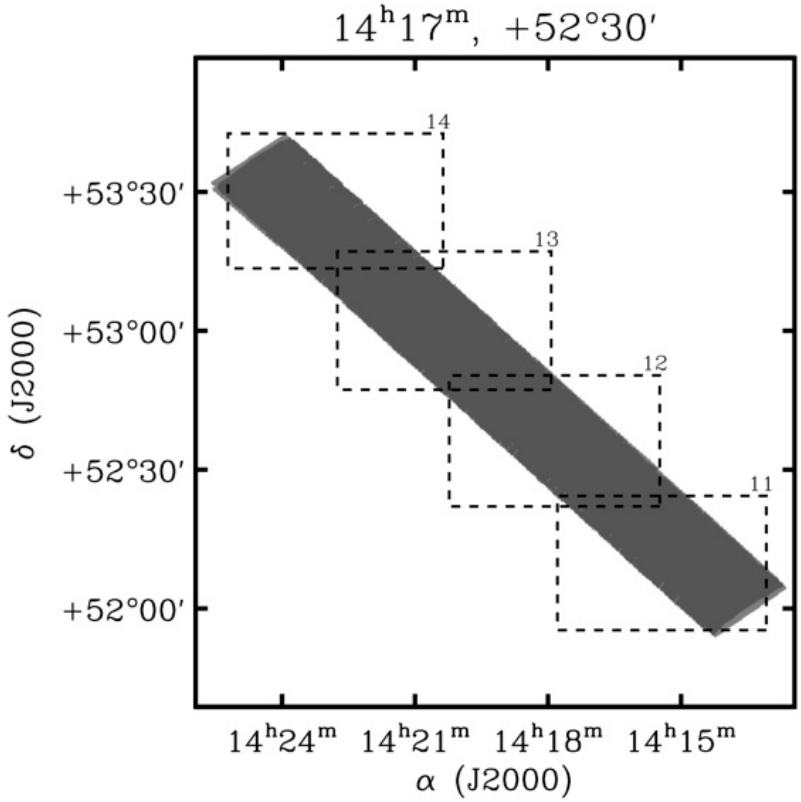

Figure 2-3 DEEP2 coverage in the Extended Groth Strip (EGS). Light grey regions indicate planned coverage and dark grey regions are the obtained spectroscopic coverage. The dashed lines indicate CFHT *BRI* photometry coverage (image from DEEP2 project).

obtained coverage, including the number of masks used and number of targets, in each of the four DEEP2 fields.

2.2.3 Selection Effects

As described in [Newman et al., 2013] there are several known selection effects in the DEEP2 sample. First, selection based on a constant R-band magnitude results in the survey being biased towards redder galaxies at $z < 0.5$ and biased towards bluer galaxies at $z > 0.5$. This selection bias is well understood and can be corrected [Willmer et al., 2006]. The final DEEP2 sample is also known to contain incorrect classifications of faint stars as galaxies because the probability methods described in

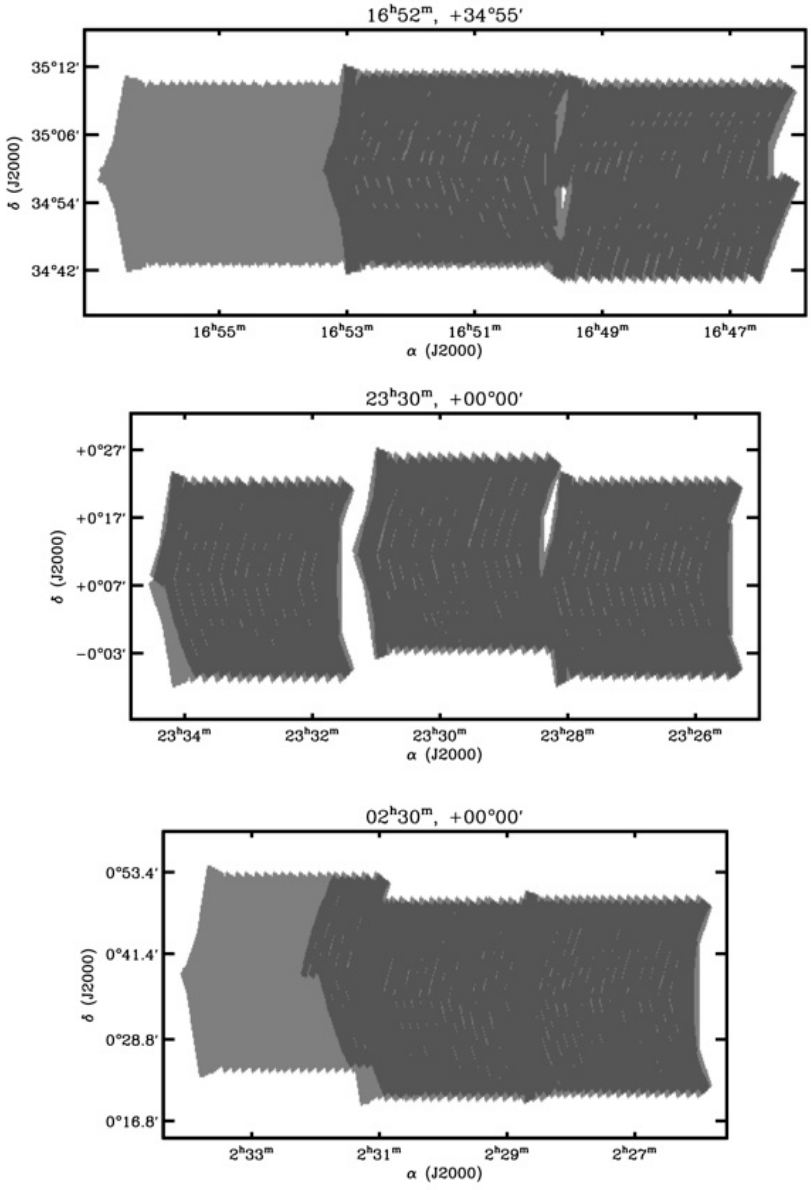

Figure 2-4 DEEP2 Field 2, 3, and 4 coverage (top to bottom). Light grey regions indicate planned coverage and dark grey regions are the obtained spectroscopic coverage. All objects have CFHT *BRI* photometry coverage (image from DEEP2 project).

[Coil et al., 2004] overestimate the probability that a faint object is a galaxy. Additionally, the methods used to separate galaxies from faint stars leads to $\sim 13\%$ of the dimmest red sequence galaxies to be excluded uniformly for galaxies at $z > 0.75$. The complexity of the selection effects of the DEEP2 Redshift Survey make computing the number densities of galaxies particularly challenging, but in general the survey is likely biased towards massive compacts in its target selection because a flux-limited spectroscopic survey will tend to identify the most concentrated objects with higher signal-to-noise ratios.

2.2.4 Data Catalogs

The full DEEP2 redshift catalog includes 52,989 entries. The catalog includes position information, CFHT photometry from [Coil et al., 2004], the estimated R-band radius, r_g, ellipticity object position angle derived from R-band image moment analysis, the slitmask and slitlet the object was observed with, the best-fit redshift and redshift quality, and the object class which indicates the best redshift fit (star, galaxy, or AGN). Additionally, a redshift catalog that removes duplicated objects, containing 50,319 unique entries, is provided. The spectral catalog includes the spectra for each object in the redshift catalog. The reduction of these spectra were performed using the DEEP2 DEIMOS data pipeline, *spec2d*, described in [Cooper et al., 2012].

2.3 Spectral Fitting

The spectra of the DEEP2 galaxies with sufficient signal-to-noise ratios were modeled and fit by our collaborator Ivan Katkov according to the procedure described in [Damjanov et al., 2013, Damjanov et al., 2014]. Assuming a simple stellar population (SSP), which describes a population of chemically homogenous stars that formed at the same time, and we fit the spectra against a grid of `PEGASE.HR` (Projet d'Etude des GAlaxies par Synthese Evolutive) [Le Borgne et al., 2004] SSP models based on the MILES stellar library [Sánchez-Blázquez et al., 2006] using the `NBURSTS` pixel space fitting technique [Chilingarian et al., 2007b, Chilingarian et al., 2007a].

For each spectrum, the SSP model grid, which covers a wide range of ages and metallicities, is convolved with the instrumental response of the DEIMOS spectrograph. The minimization procedure convolves the SSP model once more with a Gaussian line-of-sight velocity distribution, and multiplies the model by a low-order continuum polynomial to absorb calibration errors in both model and data. The best-fitting SSP (or combination of two) is chosen by interpolating a grid in age and metallicity. The resulting fit returns the radial velocity, mean age, metallicity [Z/H], and velocity dispersion σ for each DEEP2 object. Figure 2-5 shows one of the modeled DEEP2 spectra.

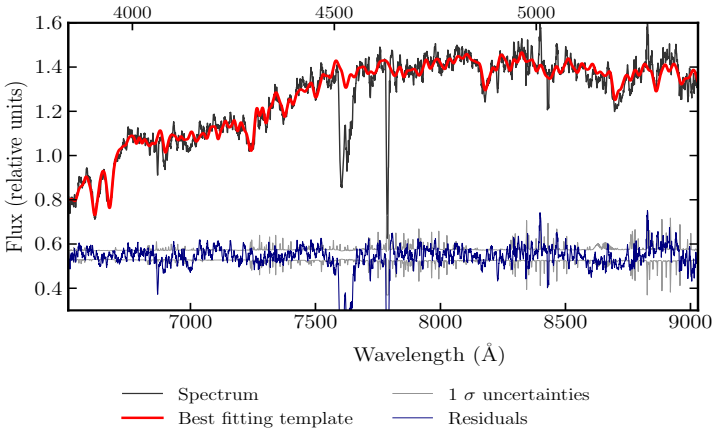

Figure 2-5 Example spectra fit of a DEEP2 galaxy at $z = 0.682$. The spectra for each object displays the smoothed flux in black, best fitting SSP template spectra in red, the residuals of the fit in blue, and the $\pm$ 1 sigma uncertainties, scaled to the smoothing, in grey. The lower x-axis indicates the observed wavelength and the upper x-axis indicates the rest-frame wavelength ($\lambda_{rest} = \lambda_{obs}[1+z]^{-1}$). As made evident by the residuals, the atmospheric absorption band is masked and not fit.

2.4 Photometric Catalog

To determine stellar masses we compiled a multi-band photometric catalog for the DEEP2 galaxies from Spitzer/IRAC [Barmby et al., 2008], Palomar/WIRC [Bundy et al., 2006], CFHT Legacy Survey [Gwyn, 2012], NEWFIRM Medium-band Survey [Whitaker et al., 2011],

and GALEX photometry accessed through CasJobs[1] [Martin et al., 2005]. In this study, rest-frame K-band magnitudes are used to calculate stellar masses. The K-band is optimal for probing the stellar mass content of our compact, quiescent candidates because it is less sensitive to dust, more sensitive to late-type giant stars whose spectral energy distribution (SED) is peaked in the near-IR, and mass-to-light ratio models (that will be discussed in Section 4.2) based on the K-band vary less with SSP age than B-band mass-to-light ratios.

The K-correction

As explained in [Hogg et al., 2002], to meaningfully compare a source's measured magnitude to the magnitudes of sources at different redshifts it is necessary to apply a K-correction, which converts the observed magnitude of an object at redshift z to its rest-frame magnitude. To transform the observed IRAC apparent magnitudes for our DEEP2 galaxies to rest-frame, K band apparent magnitudes the functional form of the K-correction is determined using a multi-wavelength SED fitting procedure explained in [Chilingarian et al., 2010] and [Chilingarian and Zolotukhin, 2012]. Our adopted functional form for the K-correction,

$$kcorr(z) = 5.63 - 25.35z + 40.03z^2 - 29.4z^3 + 8.13z^4, \tag{2.4}$$

depends only on redshift. The color dependence of the K-correction is negligible and thus is excluded from the function. The determined uncertainties of the K-correction range from 0.02 - 0.055 mag.

2.5 Initial Selection of Quiescent ETGs

To begin our search for CQGs in the redshift range $0.5 \leq z \leq 1.1$, we first select for massive quiescent ETGs. We determine the sizes of these quiescent ETGs in Chapter 3 and in Chapter 4 we evaluate compactness and select for CQGs.

[1] http://galex.stsci.edu/casjobs/

To begin the search for massive quiescent ETGs, we place cuts on the derived velocity dispersions σ, obtained from the spectral fitting, of the DEEP2 objects. We select objects with velocity dispersions $\sigma > 80$ km s^{-1}, indicative of high dynamical mass, and $\sigma < 350$ km s^{-1}, which is the upper limit on realistic velocity dispersion measurements determined by the spectral fitting. We also place a velocity dispersion quality cut to ensure fit quality and exclude objects with $\sigma/\sigma_{err} < 6$ where σ_{err}, the error on the velocity dispersion, has been weighted by the χ^2 of the fit. Of the 29,879 DEEP2 objects whose spectra have been fit, 1,742 are in the desired redshift range and meet these two velocity dispersion criteria.

We first select for quiescence spectroscopically by excluding objects with significant emission line equivalent widths (EW), indicative of active star formation. We fit the emission line spectra for each DEEP2 object using similar techniques described in Section 2.3 to determine the EWs and fluxes of the emission lines present in each spectrum. We select objects with EW[O II]$\lambda\lambda$3727,3730 < 5 Å, EW Hβ λ4863 < 5 Å, EW[O III]$\lambda\lambda$4960,5008 < 5 Å, and EW[O III]λ4364 < 5 Å. 1,487 galaxies meet both velocity dispersion criteria and the quiescence criteria. After reducing the sample size based on the availability of structural parameters, we visually evaluate the spectra to further ensure quiescence (described in Chapter 4).

In summary, the initial selection criteria are:

- $0.5 \leq z \leq 1.1$
- $\sigma/\sigma_{err} \geq 6$
- $80 < \sigma < 350$ km s^{-1}
- EW[O II]$\lambda\lambda$3727,3730, EW Hβ λ4863, EW[O III]$\lambda\lambda$4960,5008, and EW[O III]λ4364 all < 5 Å

Figure 2-6 shows the distribution of spectroscopic redshifts, velocity dispersions, metallicies, and ages of the initial selection. For the initial sample of quiescent ETGs the median redshift is $\tilde{z} = 0.765$, the median velocity dispersion is $\tilde{\sigma} = 201.$ km s^{-1},

the median metallicity is $[\tilde{Z/H}] = 0.102$ dex, and the median SSP age is $\tilde{Age} = 2.27$ Gyrs. The size measurements, including the effective half-light radius, for this initial sample and selection for CQGs continues in Chapter 3 and 4.

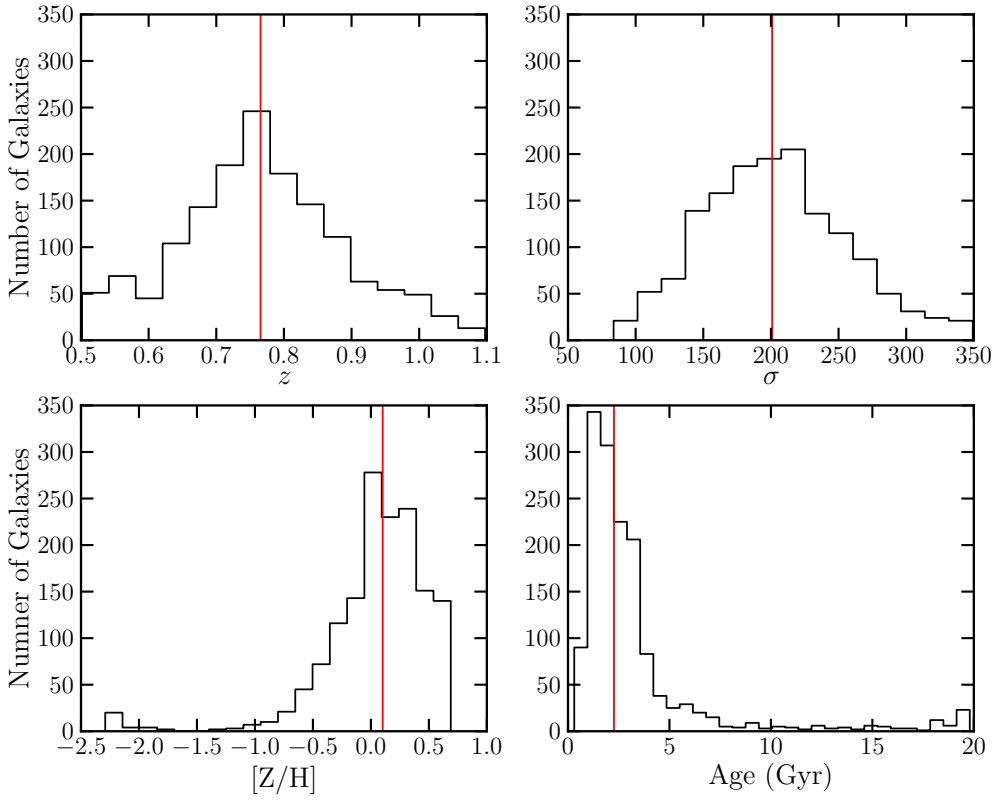

Figure 2-6 Redshift, velocity dispersion, metallicity, and SSP age distributions of the 1,487 quiescent ETGs that meet the initial selection criteria. The red line in each histogram indicated the median ($\tilde{z} = 0.765$, $\tilde{\sigma} = 201.$ km s^{-1}, $[\tilde{Z/H}] = 0.102$ dex, $\tilde{Age} = 2.27$ Gyrs).

Chapter 3

Size Measurements

Structural properties are central to the study of CGQs. To evaluate the compactness of our sample of 1,487 quiescent ETGs we need to determine their physical sizes in addition to other structural parameters including their Sérsic indices and ellipticities. In this Chapter, we first discuss the Hubble Space Telescope (HST) imaging used to measure structural properties and we next describe the program `GALFIT` and explain how it is used to fit the surface brightness profile of a galaxy. In preparation for fitting the galaxies in our sample that do not already have size measurements, we perform point spread function (PSF) test on a sub-sample of 10 objects. Finally, we fit the remaining galaxies in our sample and obtain the structural properties of a total of 257 galaxies, 33 that are newly measured.

3.1 HST Imaging

The structural properties of a galaxy can be extracted from its image. To obtain the properties necessary to evaluate the compactness of our initial sample of DEEP2 massive quiescent galaxies we both utilize existing structural catalogs and make new measurements of galaxies not previously measured. Both the existing size measurements from [van der Wel et al., 2012] and [Griffith et al., 2012] and our size measurements utilize HST imaging.

The Hubble Space Telescope is a space-based 2.4-meter telescope that has been

Table 3.1. ACS and WFPC2 Instrument Properties

	CCD	Wavelength Range Å	FOV	Pixel Scale ″/pix	Saturation Value e^-	Zeropoint mag
	(1)	(2)	(3)	(4)	(5)	(6)
ACS	WFC	3700-11000	202″ x 202″	0.05	80,000	25.954
WFPC2	WF2,3,4	1150-11000	150″ x 150″	0.1	53,000	25.033

Note. — (1) CCD used for size measurement; (2) Wavelength range covered by instrument; (3) Camera field of view; (4) Number of arcseconds covered by pixel; (5) Number of electrons to saturate a pixel; (6) The magnitude photometric zeropoint calculated from the image headers

†Instrument information from the Wide Field and Planetary Camera 2 Instrument Handbook

collecting data for nearly 25 years. Designed to operate in the near-IR, optical, and ultraviolet wavelength regimes HST has used four primary instruments: the Advanced Camera for Surveys (ACS), the Wide Field Planetary Camera 2 (WFPC2), the Wide Field Camera 3 (WFC3), and the Near Infrared Camera and Multi-Object Spectrometer (NICMOS) to image the sky both broadly and deeply. Imaging from HST is preferred to ground-based imaging due to the increased angular resolution that is necessary for measuring the sizes of distant, compact objects. For our own size measurements we download images from the Hubble Legacy Archive[1] (HLA). The HLA, jointly maintained by the Space Telescope Science Institute (STScI), the Canadian Astronomy Data Centre[2] (CADC), and the Space Telescope European Coordinating Facility (ST-ECF), provides enhanced HST data products for imaging completed by the four primary HST cameras.

Since the SEDs of the early-type galaxies we are studying peak in the red and are redshifted to $z \sim 0.7$ we want to measure the sizes in the reddest filter possible. While the F125W bandpass of WFC3 would be ideal at a wavelength of 12500 Å, the WFC3 coverage of the DEEP2 fields is limited compared to ACS and WFPC2 coverage. To maximize our sample size we choose the reddest filter, F814W at a wavelength of 8140 Å, available for ACS and WFPC2. In the following section we show that the difference in size measurements based on F125W and F814W is actually quite small,

[1]http://hla.stsci.edu/

[2]http://www.cadc-ccda.hia-iha.nrc-cnrc.gc.ca/en/hst/

justifying our choice of using the reddest filter with the largest coverage area. Table 3.1 summarizes the basic ACS and WFPC2 instrument properties[3] and information needed for the size measurements.

In selecting F814W images for either the PSF test described in Section 3.4 or measuring the sizes of our sample we choose the deepest images with the greatest exposure time available. Additionally, we only use the images of the highest level of calibration. We are grateful to the Canadian Astronomy Data Centre staff members Patrick Dowler and Daniel Durand for their help in setting up our HST image access scripts.

3.2 GALFIT

Both the size measurements we use and our own measurements employ `GALFIT`, which is a two-dimensional, galaxy profile fitting algorithm. `GALFIT` is particularly versatile in that it allows for simultaneous fitting with multiple components. While `GALFIT` can model several different functions including an exponential disk profile, Nuker law, Gaussian profile, and Moffat/Lorentzian profile, we utilize the Sérsic surface brightness profile [Sersic, 1968]. The Sérsic surface brightness profile, which is a generalization of de Vaucouleurs' law (Equation 1.1), is given by,

$$\sum(r) = \sum_e e^{-\kappa[(\frac{r}{r_e})^{1/n}-1]}, \tag{3.1}$$

where r_e is the effective radius containing half the total flux, $\sum_e$ is the surface brightness at r_e, κ is a constant of normalization, and n is the Sérsic power-law index. The Sérsic index determines the curvature of the profile where smaller n describes a galaxy that is less centrally concentrated. A Sérsic index of $n = 1$ gives the exponential disk profile that describes spiral galaxies while a Sérsic index of $n = 4$ is the de Vaucouleurs profile (Equation 1.1) that describes elliptical galaxies.

As described by [Peng et al., 2002], the best-fit Sérsic profile is attained by minimizing the χ^2 between the model convolved with the PSF and the galaxy image.

[3] http://documents.stsci.edu/hst/wfpc2/documents/handbooks/cycle17/wfpc2_ihb.pdf

First GALFIT prepares the user inputted PSF for convolution and then it creates a model image based on the inputted image to be fit and initial parameters. Over the set convolution region, GALFIT convolves the model with the PSF using a Fast Fourier Transform Technique. This convolved image is then compared to the data image and the residuals between the two, weighted by the sigma image, are minimized using the Levenberg-Marquardt downhill-gradient method [Press and Teukolsky, 1997]. This process is iterated until χ^2 remains constant to 5 parts in 10,000 for 5 iterations.

The main input to GALFIT is the parameter file which includes the data image, sigma image, PSF, and initial parameter guesses for the components being fit. While the user can opt to supply GALFIT with a sigma image, GALFIT will create a sigma image, which is the standard deviation of counts at each pixel, based on Poisson statistics of the data image and the information found in the image header including the exposure time, CCD gain, read noise, and the number of images that have been added together. The data image needs to be in units of counts, instead of counts/sec, for GALFIT to create the sigma image.

There are several methods of creating a PSF: (1) empirically from image extraction, (2) modeled using the TinyTim software for HST imaging [Krist et al., 2011], or (3) or analytically based on the FWHM of the seeing. If available, the best method for creating a PSF is by extracting it from the data image. A good PSF image has a high signal-to-noise (but is not saturated), is isolated from other objects, is centered in the PSF cutout image, is large enough to contain all of the light (typically 20-50 times the FWHM), has a FWHM of at least 2 pixels i.e. Nyquist sampled, has a zero background, and matches the shape of the star including possible diffraction rings [Peng et al., 2002]. Following these guidelines, a PSF can be empirically extracted and prepared for the GALFIT convolution in a number of ways. A single extracted PSF can be used or several PSFs can be simply combined by averaging the images together. The IRAF package DAOPHOT can be used to combine multiple PSF stars in the data image weighted by their magnitudes [Stetson, 1987].

3.3 Existing Size Measurements

For some of the galaxies in our sample, there are previously existing size measurements from HST data. Based on HST ACS imaging, [Griffith et al., 2012] provides a structural catalog for nearly half a million galaxies in five fields including the EGS. In the EGS field, where there is overlap with the DEEP2 survey, there is extensive ACS/F814W coverage compromised of 63 pointings at an exposure time of 2100 seconds each. [Griffith et al., 2012] uses F814W mosaics produced by the STSDAS *multidrizzle* package[4] that have a final pixel scale of 0.03″/pix. To fit the 55,808 objects in EGS with F814W coverage, [Griffith et al., 2012] employs the automated fitting routine `GALAPAGOS` (Galaxy Analysis over Large Areas: Parameter Assessment by GALFITting Objects from SExtractor) which batch fits the structural parameters of galaxies using `GALFIT` in conjunction with `SExtractor`. Fitting the objects with a single-component Sérsic profile, [Griffith et al., 2012] uses $n = 2.5$ for the initial Sérsic index guess whereas for the other input parameters the `SExtractor` values are used. A single high signal-to-noise PSF is used for all of the EGS/F814W fitting.

Structural properties based on HST WFC3 imaging are provided by [van der Wel et al., 2012] from the CANDELS (Cosmic Assembly Near-infrared Deep Extragalactic Legacy Survey) project. The CANDELS project is the largest of its kind: probing more then 250,000 galaxies in the IR from z = 1.5 to 8 using the high resolution Wide Field Camera 3 on the Hubble Space Telescope [Koekemoer et al., 2011, Grogin et al., 2011]. [van der Wel et al., 2012] also employ `GALAPAGOS` to batch fit 41,457 EGS galaxies based on WFC3/F125W mosaics with a pixel scale of 0.13″. All of the initial parameter guesses for the single-component Sérsic fits were supplied by the `SExtractor` output. Described in greater detail in [van der Wel et al., 2012], a hybrid PSF model combining both stars extracted from the mosaics and a synthetic PSFs created from `TinyTim` is used for the fitting.

As discussed in [van der Wel et al., 2014], the measured size of a galaxy depends on the evolution of the color gradients. While the effect of the color gradient on

[4] http://stsdas.stsci.edu/multidrizzle/

measured size is most significant for late-type galaxies that have bluer extended disks, the smaller effect on the size measurement of compact early-type galaxies is significant for determining their mass-size evolution.

The effective radius, $R_{\rm eff}$ at a rest-frame wavelength of 5000Å is estimated to be,

$$R_{\rm eff} = R_{\rm eff,F}\Big(\frac{1+z}{1+z_p}\Big)^{\frac{\Delta \log R_{\rm eff}}{\Delta \log \lambda}}, \tag{3.2}$$

where z_p is the pivot redshift and $R_{\rm eff,F}$ is the size of the object measured in a specific filter. The pivot redshift is determined from $z_p = (\lambda_{\rm obs}/\lambda_{\rm filter})$ - 1 where $\lambda_{\rm obs}$ = 5000Å. For the F125W filter with $\lambda_{\rm filter}$ = 12500Å the pivot redshift is 1.500 and for the F814W filter with $\lambda_{\rm filter}$ = 8140Å the pivot redshift is 0.628. For a sample of 122 early-type galaxies from $0 < z < 2$ in the COSMOS field, the average size gradient based on F814W, F160W and F125W size measurements is found to be $\Delta \log R_{\rm eff}/\Delta \log R_\lambda$ = -0.25 independent of redshift and mass [van der Wel et al., 2014].

Of our initial sample of 1,487 quiescent ETGs, 226 are included in the [Griffith et al., 2012] ACS catalog and 63 are included in the [van der Wel et al., 2012] WFC3 catalog. All 63 objects in the WFC3 catalog are also contained in the ACS catalog. To justify using the bluer filter for size measurements because of the increased coverage we compare the structural properties of 352 objects with both F814W and F125W measurements (not necessarily in our DEEP2 sample). Figure 3-1 shows how the ratio of the F814W to F125W properties change as a function of the F125W properties. The circularized effective radius $\rm R_{e,c}$ in kiloparsecs is computed as,

$$\rm R_{e,c} = (pix\ scale\ ''/pix) R_{pix} \sqrt{q} \Big[\frac{D_A(z, H_0, \Omega_M, \Omega_\Lambda)}{206.265}\Big] \tag{3.3}$$

where pix scale is the pixel scale appropriate for each camera (WFC3 or ACS), $\rm R_{pix}$ is the size of the object measured by `GALFIT` in pixels, q is the axis ratio measured by `GALFIT`, and D_A is the angular diameter distance as a function of cosmology and spectroscopic redshift, and the factor of 1/206.265 is the kiloparsec conversion.

As made evident by Figure 3-1 the difference between the structural properties of the F814W and F125W measurements is minimal. To characterize the difference be-

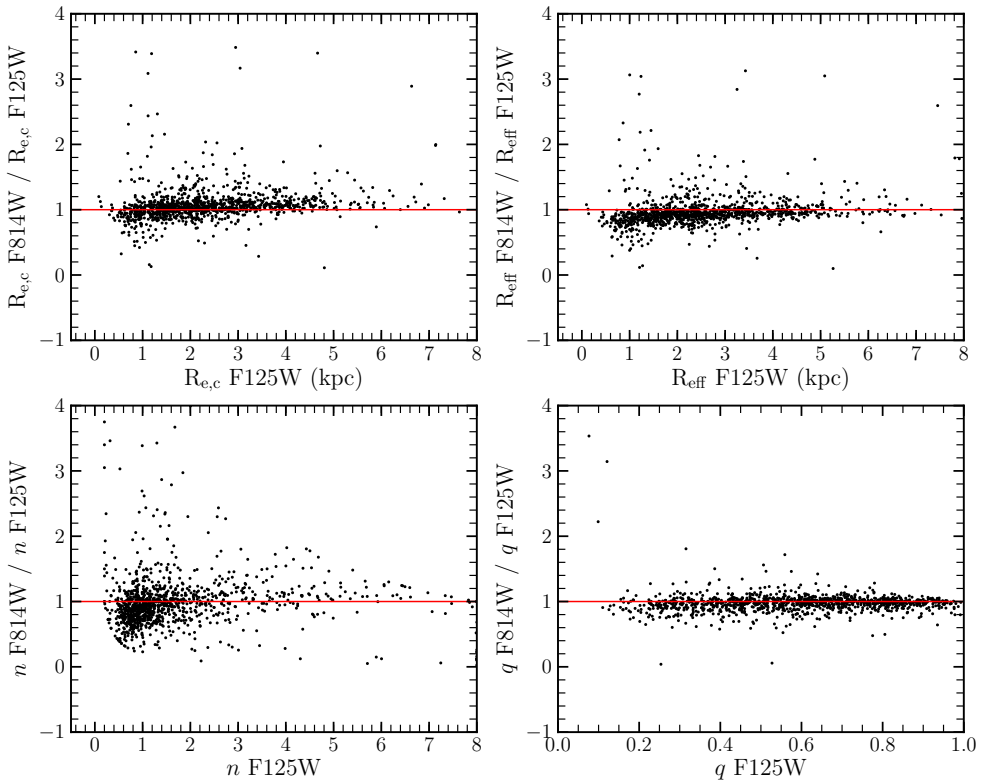

Figure 3-1 The ratio of the F814W [Griffith et al., 2012] to F125W [van der Wel et al., 2012] structural properties as a function of the F125W structural properties. The mean deviation from unity for the uncorrected size, $R_{e,c}$, is 9%, for the color-corrected size is 10%, for the Sérsic profile n is 18%, and for the ellipticity q is 5%.

tween the measurements made in the two filters we first reject the outliers by removing the upper 5% of objects with the greatest deviation from unity for each parameter and then compute the mean deviation for points lying within three standard deviations from unity. For the uncorrected circularized radii the mean difference between the F814W and F125W measurements is 9% and for the color-corrected sizes the mean difference is 10%. The difference between the uncorrected and corrected radii is negligible compared the estimated `GALFIT` uncertainties so it is not imperative that we apply this correction to our measurements. The mean difference between the F814W and F125W measurements for the Sérsic index is 18% and for the ellipticity is 5%.

Table 3.2. Structural Parameters of PSF Investigation Galaxies[†]

Object Number	α [°]	δ [°]	z	$R_{e,c}$ [kpc]	R_{pix} [pix]	$n^{single}_{Sérsic}$	q^{single}
(1)	(2)	(3)	(4)	(5)	(6)	(7)	(8)
13019294	214.90053	52.9062	0.850	0.68 ± 0.01	3.64 ± 0.04	3.77 ± 0.09	0.67 ± 0.01
13041525	215.30159	53.0889	0.998	1.04 ± 0.03	5.3 ± 0.1	4.3 ± 0.2	0.66 ± 0.01
12019899	214.68509	52.6372	0.932	1.59 ± 0.06	10.3 ± 0.3	8.0 ± 0.2	0.43 ± 0.01
13056838	215.50250	53.1813	0.678	2.54 ± 0.06	13.0 ± 0.3	5.73 ± 0.09	0.86 ± 0.01
13033496	215.16406	53.0343	0.750	3.53 ± 0.04	18.8 ± 0.2	2.71 ± 0.02	0.73 ± 0.01
12012898	214.30675	52.5372	0.834	4.53 ± 0.05	21.4 ± 0.2	3.41 ± 0.03	0.86 ± 0.01
13026215	215.09784	52.9597	0.745	5.3 ± 0.2	27.7 ± 0.8	4.0 ± 0.1	0.75 ± 0.01
13050585	215.13156	53.1489	0.736	6.4 ± 0.1	32 ± 0.50	2.93 ± 0.03	0.84 ± 0.01
12008254	214.35280	52.4797	0.744	7.7 ± 0.3	41 ± 1.0	7.1 ± 0.1	0.73 ± 0.01
13025494	215.20267	52.9784	0.738	10.2 ± 0.4	50 ± 2.0	5.4 ± 0.1	0.87 ± 0.01

Note. — (1) DEEP2 identification number; (2) Right ascension; (3) Declination; (4) Redshift; (5) Circularized effective radius give by Equation 3.3; (6) `GALFIT` radius in pixels; (7) Single-profile Sérsic index; (8) Axis ratio (b/a)

[†]Structural measurements from [Griffith et al., 2012] and spectroscopic redshifts from DEEP2

All of the mean differences are small compared to the estimated `GALFIT` errors so we conclude that using the bluer F814W for the increased sample size has little effect on our compactness determinations discussed in Chapter 4.

3.4 PSF Investigation

The fitting program `GALFIT` is particularly sensitive to the PSF model used for convolution so it is worth investigating how the structural properties vary as a function of PSF. For a sub-sample of 10 galaxies with structural properties measured by [Griffith et al., 2012] we re-measure their parameters with `GALFIT` using various PSFs. We select the sub-sample to have a range of sizes (as reported by [Griffith et al., 2012]) from 0.68 kpc to 10.3 kpc. The [Griffith et al., 2012] structural properties of these 10 galaxies are listed in Table 3.3.

We use three different techniques to extract PSFs from each objects 200″ x 200″ tile downloaded through the CADC HLA: (1) extracting 2-3 good PSF stars from the tile depending on availability, (2) taking the average of 2 extracted PSFs, and (3) using the `IRAF` (the Image Reduction and Analysis Facility) package `DAOPHOT` to

construct a magnitude weighted PSF model based on several extracted stars in the tile.

In searching for PSF stars to extract we ensure to abide by the GALFIT PSF guidelines described in Section 3.2. We use the IRAF[5] package *imexamine* to inspect radial profiles of candidate PSF stars to ensure they are below the saturation limit and Nyquist sampled. IRAF is a suite of routines written to reduce and analyze astronomical images and data. We use *imexamine* routine to examine the radial profiles of PSF star candidates by fitting their profiles with a Moffat distribution and determining the full width at half maximum (FWHM). To take the average of two PSFs we use the IRAF routine *imcombine*. We use a set of IRAF routines in the package DAOPHOT to create magnitude weighted PSF models for each galaxy in our sub-sample [Stetson, 1987]. First, we use the routine $daofind$ create a list of all sources in each tile and then use the routine *phot* to perform aperture photometry on all of the sources found. Using the routine *pstselect* we interactively select isolated, non-saturated stars to be used in the routines psf and $seepsf$ which create an image of the magnitude weighted PSF model that can be used for the GALFIT fitting. For each object we select 5-15 stars (not all necessarily bright enough to be extracted as a single PSF star) for the DAOPHOT PSF model. Figure 3-2 shows the images of the stars used for each galaxy in the PSF investigation. For each galaxy we create a DAOPHOT PSF and an average PSF based on two image extracted PSFs. For 5 of the galaxies we find 3 suitable single stars to be used in the fitting and for 4 of the galaxies we find 2. One of the galaxies has only one bright star suitable to be used for the fitting, but we create an average PSF with a lower signal-to-noise star. We also use one of the image extracted PSF stars to fit every galaxy.

Using GALFIT we fit the structural properties of each of the ten galaxies 4-6 times using the various PSFs constructed for each. In the GALFIT parameter file we must specify the initial guesses for the magnitude, half-light radius, axis ratio, and Sérsic index. To provide an initial guess for the magnitude we use the *imexamine* aperture photometry routine to compute the flux of the galaxy within the aperture and

[5]http://iraf.noao.edu/

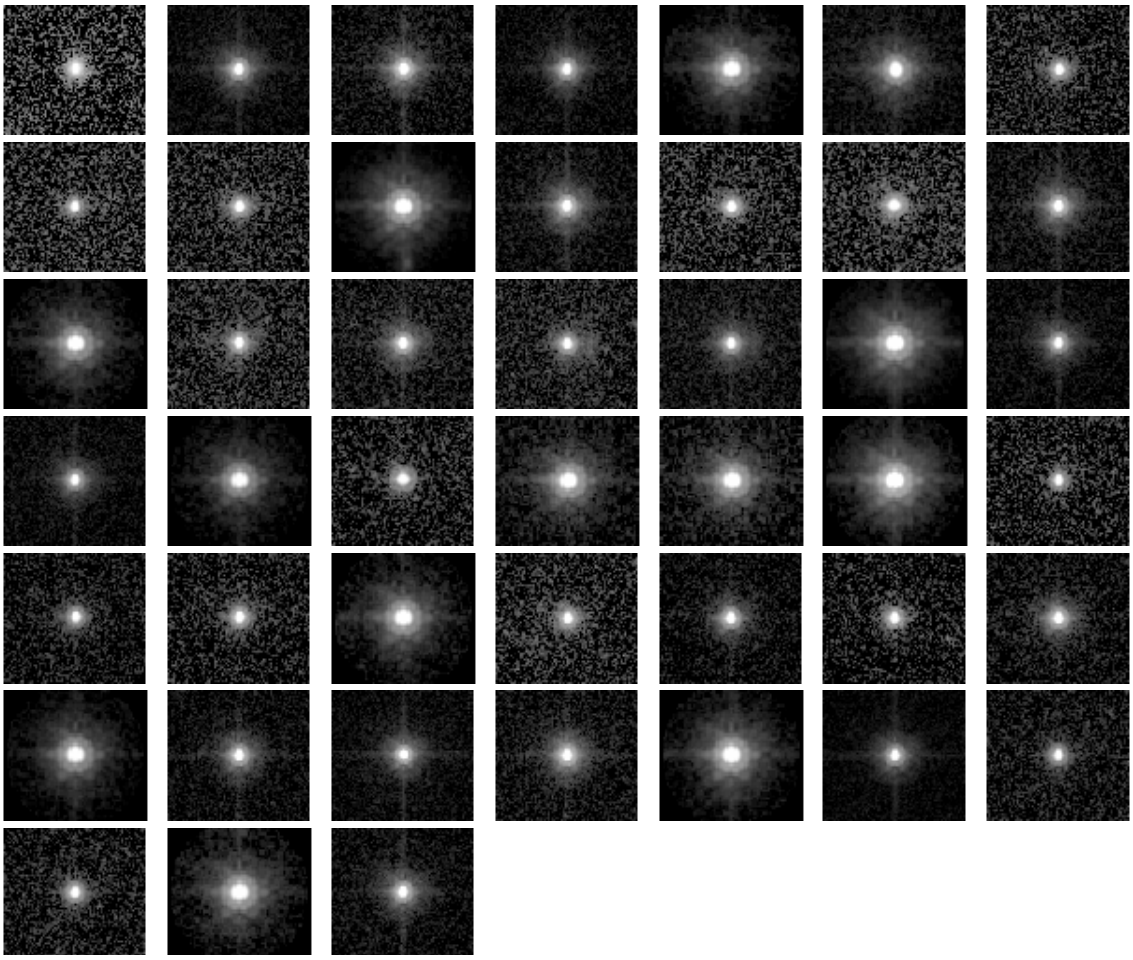

Figure 3-2 Stars used for the PSF investigation. The last star is the single PSF used to fit all 10 of the galaxies in the sub-sample.

compute the magnitude as,

$$m = -2.5\log_{10}\left(\frac{\text{flux}}{exptime}\right) + mgzpt, \tag{3.4}$$

where *exptime* is the exposure time of the image and *mgzpt* is the zeropoint magnitude for ACS F814W given in Table 3.1. For the half-light radius and axis ratio initial guess we adopt values of $\mathrm{R_{e,guess}} = 10$ pixels and $q_{\mathrm{guess}} = 0.7$ after varying the initial guesses for each and finding the final fitting results do not significantly depend on these guesses as long as they are reasonable. For the initial guess Sérsic index we adopt $n_{guess} = 2.5$ following [Griffith et al., 2012]. In addition to the galaxies in our sub-sample, we fit all bright objects in the fitting area and the background sky.

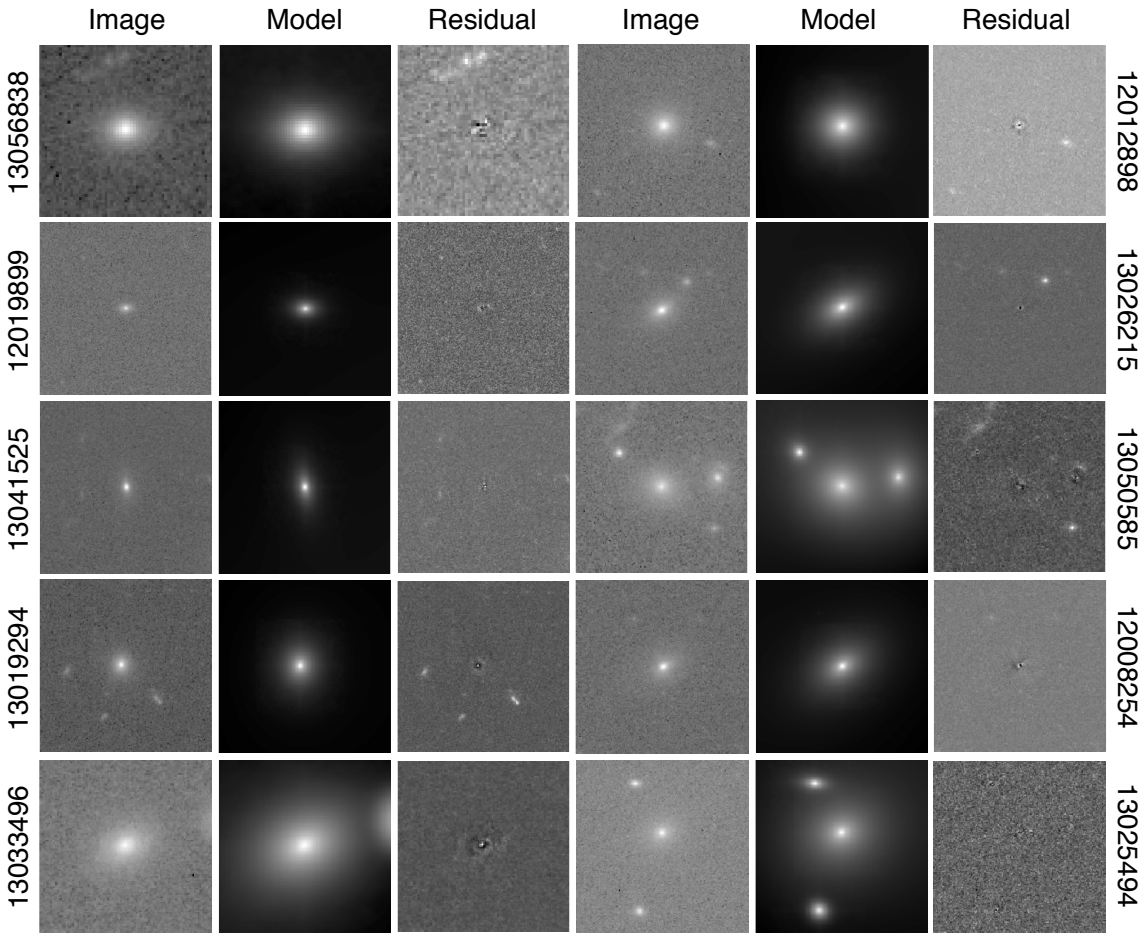

Figure 3-3 Data image, single Sérsic `GALFIT` model, and residual image for the ten PSF test galaxies based on the single PSF used to fit all objects.

Figure 3-3 shows the data image, `GALFIT` model, and residual image of the ten test galaxies fit with the same PSF. Some of the single Sérsic fits, including the fits for objects 12012898 and 13033496, leave behind residual flux that is not taken into account in the model. For these objects we experiment with fitting multiple Sérsic components simultaneously and find these fits leave behind less residual flux but to compare our new structural property measurements to those in [Griffith et al., 2012] we want to use only a single Sérsic fit. Additionally, the interpretation of the structural properties of multi-Sérsic component fits is not straight-forward or well standardized. Even

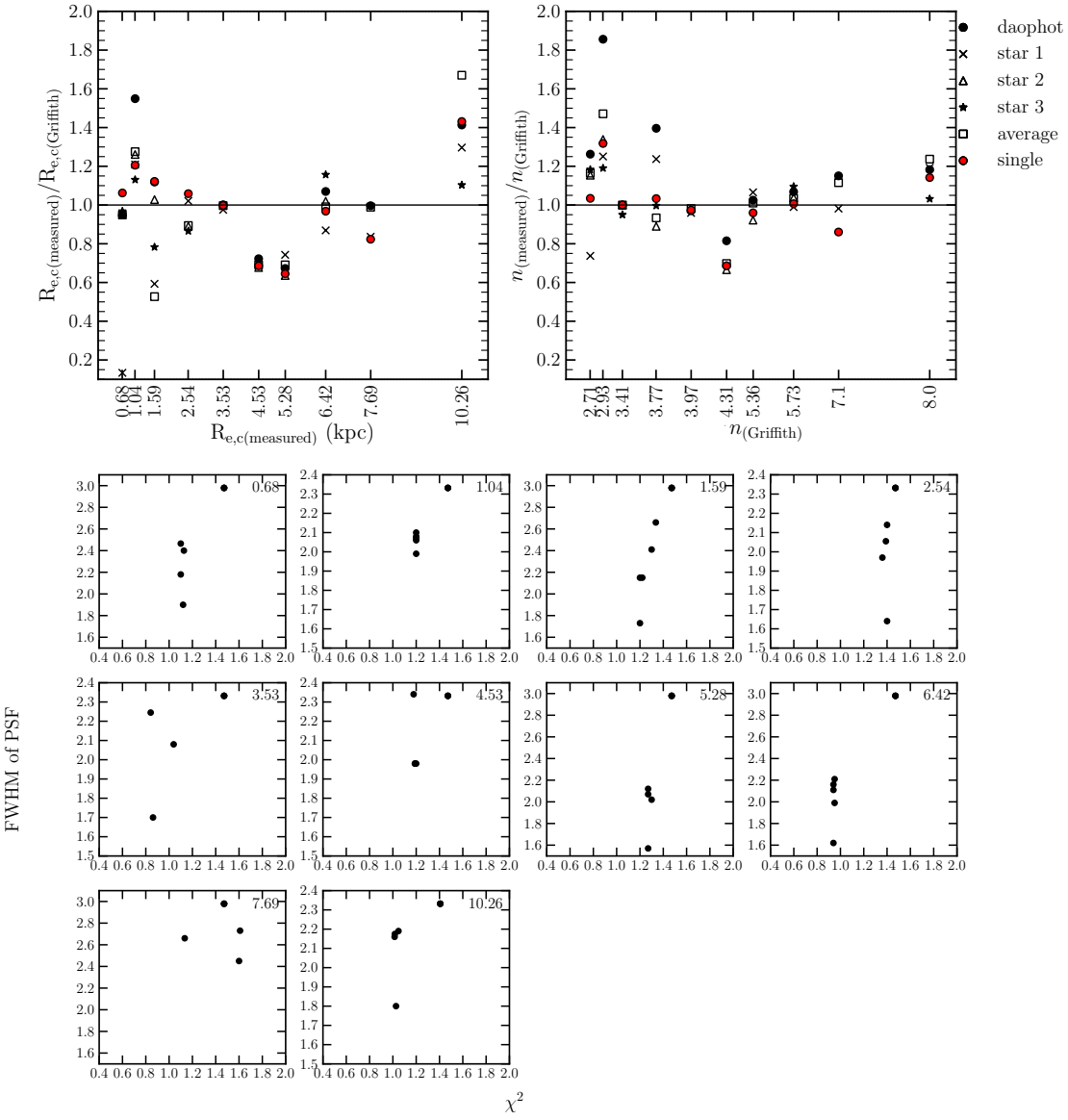

Figure 3-4 The spread in GALFIT parameters half-light radius and Sérsic index using the various PSFs for each galaxy (top plots). The red point is the same PSF star used to fit all galaxies. The bottom set of plots shows how the χ^2 of the fit changes as a function of the PSF FWHM for each galaxy.

though some of the objects we fit leave behind residual flux we use a single component Sérsic fit so that our measurements are directly comparable to measurements in the literature.

Comparing the FWHM of each PSF used to fit each galaxy to the χ^2 of the fit we find that for a majority of the galaxies only the PSF with the greatest FWHM vary the most significantly from the average χ^2 (Figure 3-4). This suggests that the higher FWHM PSFs, which are the fainter stars (or possibly extended objects) in Figure 3-2, are not ideal PSF stars. Additionally, the objects with larger χ^2 scatters including 13022496, 12008254, and 12012898 are objects that are better fit with multiple Sérsic profiles. The upper two plots of Figure 3-4 show how the measured half-light radius and Sérsic index changes depending on the PSF used which shows that there is no trend with increasing size or Sérsic index. Together with the χ^2-FWHM scatter we decide that using a single good, high signal-to-noise PSF is adequate, as done in [Griffith et al., 2012] and other studies, for the fitting performed in the next section.

3.5 Our Fits

Altogether, 226 galaxies of our initial selection of quiescent ETGs have F814W size measurements from [Griffith et al., 2012]. To take full advantage of the DEEP2 data set as possible, we search for F814W ACS or WFPC2 coverage of the remaining unmeasured 1261 galaxies. Figure 3-5 shows the ACS footprint (blue) and WFPC2 footprint (red) overlayed on the positions of the unmeasured quiescent DEEP2 galaxies in EGS, Field 3, and Field 4. There is no HST coverage of Field 2. Table 3.2 summarizes the size measurement coverage for the 1,487 quiescent ETGs in the HST footprint. In addition to the 226 publicly available size measurements, an additional 87 galaxies are in either the ACS or WFPC2 F814W footprint.

Downloading images from the CADC HLA, we find that of the 18 DEEP2 galaxies in the ACS footprint, 10 have the highest level of calibrated imaging available. Of 69 DEEP2 galaxies in the WFPC2 footprint 23 either have the highest level of calibrated imaging available or are sufficiently far away from the edge of the pointing to be fit.

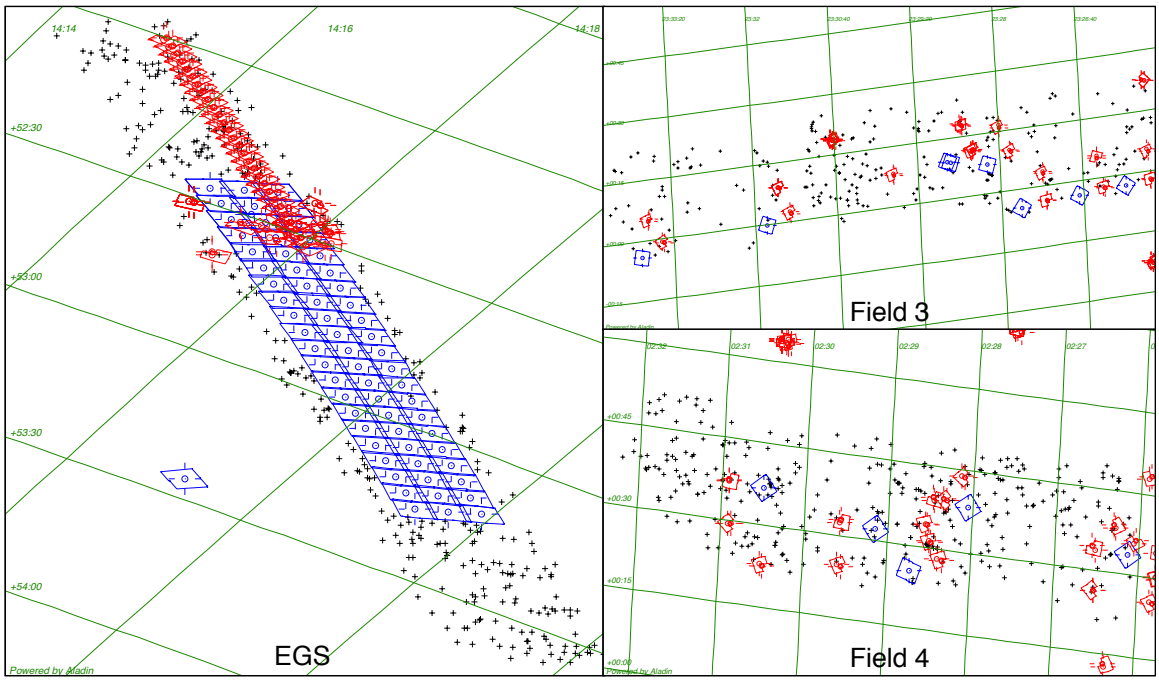

Figure 3-5 DEEP2 objects with ACS (blue) or WFPC2 (red) F814W coverage not measured in [Griffith et al., 2012]. The black points are the DEEP2 galaxies that meet the initial selection criteria. There is no coverage in DEEP2 Field 2.

We search the downloaded ACS and WFPC2 tiles for a high signal-to-noise PSF in each to be used in the fitting. Figure 3-6 shows the radial plot and image of both the ACS and WFPC2 PSFs. We follow the same fitting procedure described in the previous section. We specify `GALFIT` initial guess of $R_{e,guess} = 10$ pixels, $q_{guess} = 0.7$, and $n_{guess} = 2.5$ and compute the magnitude guess using `IRAF` and Equation 3.4. We fit all bright objects in the fitting area and the background sky. Table 3.4 displays the measured structural properties for 33 DEEP2 objects to be added to the sample of 224 objects with [Griffith et al., 2012] measurements. Now that we have size measurements for our sample of quiescent ETGs, we can evaluate compactness and search for CGQs.

Table 3.3. Summary of DEEP2 F814W Size Measurements

Camera	DEEP2 Field	# Galaxies Measured	# Galaxies Not Measured
ACS	EGS	226†	1
	2	0	0
	3	0	2
	4	0	15
WFPC2	EGS	-	47
	2	-	0
	3	-	5
	4	-	17

†Size measurements from [Griffith et al., 2012].

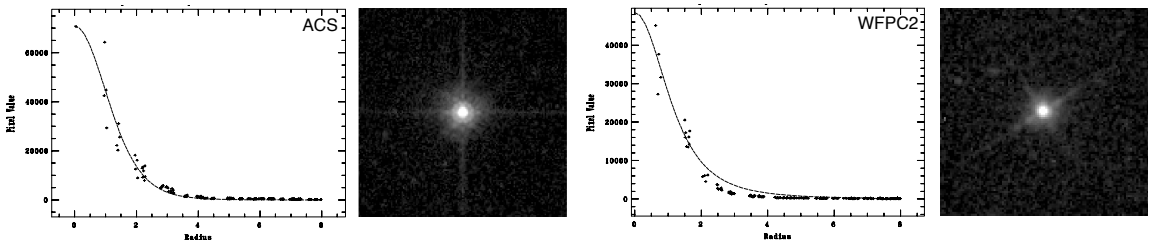

Figure 3-6 The PSFs used for ACS and WFPC2 image fits.

Table 3.4. New DEEP2 Structural Properties

Object Number	α [°]	δ [°]	z	Camera	$R_{e,c}$ [kpc]	R_{pix} [pix]	$n_{Sérsic}^{single}$	q^{single}
(1)	(2)	(3)	(4)	(5)	(6)	(7)	(8)	(9)
41032729	36.53966	0.5809	0.77	ACS	2.6 ± 0.2	7.4 ± 0.5	5.4 ± 0.2	0.92 ± 0.01
42037361	37.60525	0.6191	0.869	ACS	3.5 ± 0.3	9.9 ± 0.5	3.1 ± 0.1	0.8 ± 0.1
42037703	37.60768	0.6304	0.854	ACS	2.2 ± 0.4	7 ± 1	3.7 ± 0.5	0.72 ± 0.04
42029812	37.61381	0.5932	0.858	ACS	0.96 ± 0.02	3.08 ± 0.06	2.7 ± 0.1	0.66 ± 0.01
42033566	37.28237	0.5626	0.84	ACS	2.7 ± 0.4	10 ± 2	6.1 ± 0.6	0.48 ± 0.02
42025784	37.28803	0.5125	0.718	ACS	5 ± 1	21 ± 4	14 ± 1	0.47 ± 0.01
42037462	37.60567	0.6275	0.867	ACS	6.7 ± 0.7	20 ± 2	2.5 ± 0.2	0.75 ± 0.02
13101995	215.05671	52.8985	0.574	ACS	0.60 ± 0.01	3.19 ± 0.02	3.19 ± 0.05	0.33 ± 0.01
42025202	37.29991	0.5281	0.842	ACS	2.8 ± 0.2	9.7 ± 0.8	4.2 ± 0.2	0.59 ± 0.01
42029421	37.63844	0.5904	0.699	ACS	2.9 ± 0.1	10.2 ± 0.4	3.5 ± 0.1	0.64 ± 0.01
11013870	213.87992	52.0745	0.649	WFPC2	0.92 ± 0.02	2.96 ± 0.03	5.31 ± 0.09	0.20 ± 0.01
11019658	213.90904	52.124	0.572	WFPC2	1.05 ± 0.04	3.9 ± 0.1	5.7 ± 0.2	0.17 ± 0.01
11026452	213.94858	52.1456	0.619	WFPC2	2.46 ± 0.04	4.73 ± 0.06	2.72 ± 0.04	0.59 ± 0.01
11038492	214.20786	52.3026	0.807	WFPC2	4.1 ± 0.1	7.0 ± 0.2	2.80 ± 0.07	0.62 ± 0.01
11038770	214.14831	52.2719	0.682	WFPC2	2.42 ± 0.08	3.9 ± 0.1	2.07 ± 0.09	0.75 ± 0.02
11038987	214.15464	52.2510	0.682	WFPC2	4.8 ± 0.4	9.9 ± 0.9	6.0 ± 0.3	0.47 ± 0.01
11039150	214.15499	52.2695	0.682	WFPC2	6.1 ± 0.4	9.6 ± 0.7	4.8 ± 0.2	0.81 ± 0.01
11045101	214.22139	52.3446	0.507	WFPC2	1.4 ± 0.4	4 ± 1	20 ± 4	0.39 ± 0.02
11051653	214.27355	52.3761	0.818	WFPC2	4.4 ± 0.6	6.6 ± 0.9	7.7 ± 0.6	0.77 ± 0.02
11051667	214.25162	52.3628	0.551	WFPC2	2.6 ± 0.2	4.6 ± 0.3	7.9 ± 0.3	0.78 ± 0.01
12003615	214.49862	52.4519	0.744	WFPC2	3.47 ± 0.06	5.06 ± 0.08	3.79 ± 0.08	0.88 ± 0.01
12021090	214.35249	52.6599	0.901	WFPC2	3.4 ± 0.2	4.8 ± 0.3	3.8 ± 0.2	0.81 ± 0.02
31008760	351.60017	-0.0330	0.809	WFPC2	0.88 ± 0.04	2.35 ± 0.06	2.0 ± 0.2	0.25 ± 0.02
32034718	352.15393	0.3131	0.738	WFPC2	0.68 ± 0.02	1.90 ± 0.03	2.4 ± 0.1	0.24 ± 0.01
41019260	37.12902	0.5079	0.721	WFPC2	0.93 ± 0.03	3.12 ± 0.05	3.5 ± 0.1	0.17 ± 0.01
41019373	37.13189	0.5085	0.723	WFPC2	1.54 ± 0.08	3.6 ± 0.2	4.9 ± 0.3	0.35 ± 0.01
41019532	37.12726	0.5021	0.722	WFPC2	3.6 ± 0.2	5.9 ± 0.3	4.0 ± 0.1	0.72 ± 0.01
41019598	37.13491	0.5123	0.723	WFPC2	4.4 ± 0.2	6.9 ± 0.3	4.5 ± 0.1	0.80 ± 0.01
41020051	37.11260	0.5353	0.708	WFPC2	2.16 ± 0.04	5.24 ± 0.06	2.99 ± 0.04	0.33 ± 0.01
41020361	37.12607	0.5078	0.721	WFPC2	4.0 ± 0.3	6.2 ± 0.4	7.7 ± 0.3	0.81 ± 0.01
41039730	36.58362	0.6283	0.746	WFPC2	2.75 ± 0.03	4.17 ± 0.04	7.64 ± 0.02	0.81 ± 0.01
42009843	37.39804	0.4211	0.763	WFPC2	13 ± 2	8 ± 3	9.4 ± 0.5	0.76 ± 0.01
42036165	37.72227	0.6234	0.967	WFPC2	0.88 ± 0.09	2.0 ± 0.2	1.3 ± 0.2	0.32 ± 0.04

Note. — (1) DEEP2 identification number; (2) Right ascension; (3) Declination; (4) Redshift; (5) HST camera F814W image was taken with (6) Circularized effective radius give by Equation 3.3; (7) `GALFIT` radius in pixels; (8) Single-profile Sérsic index; (9) Axis ratio (b/a)

Chapter 4

Compact Quiescent Galaxies in DEEP2

Now that we have the structural properties of 257 quiescent ETGs we can select for compactness and identify a sample of CQGs. First we visually examine the spectra to ensure they are high quality and don't display significant emission line flux. After examining the spectra of our 257 ETGs, we are left with 222 quiescent ETGs from which we select for compactness. After selecting for compactness using a mass-size criterion, we compare the spectroscopic properties of the non-compact and compact samples of quiescent ETGs and report our constraints on the number density of CQGs in the range $0.5 < z < 1.1$. Lastly, we compute the redshifts of star formation quenching for the sample of CQGs to begin tracing the evolutionary histories of these objects.

4.1 Visual Inspection of Spectra

To further ensure quiescence we visually examine the spectra of all 257 quiescent ETGs with structural measurements. Despite placing quiescence cuts on our initial sample in Section 2.5 by restricting the emission line EWs of the spectra, we also want to place cuts on the emission line fluxes. We visually examine the spectra and remove galaxies with significant emission line flux above the spectrum continuum. We

find 35 galaxies to have significant [O II]$\lambda\lambda$3727,3730, Hβ λ4863, [O III]$\lambda\lambda$4960,5008, or [O III]λ4364 fluxes and remove these objects from the sample of quiescent ETGs. The final sample of quiescent ETGs includes 222 galaxies that have all been visually confirmed to be quiescent. It is from this sample that we select for compactness.

4.2 Stellar Mass Derivation

To derive the stellar masses of our quiescent ETGs, we calculate the luminosity of the objects in the K band and utilize Maraston stellar mass-to-light ratios [Maraston, 2003, Maraston and Strömbäck, 2011]. We first compute the absolute K band magnitude is given by Equation 2.1 based on the IRAC λ3.6 micron bandpass. Of our full DEEP2 sample of 222 quiescent ETGs, 204 have IRAC λ3.6 micron coverage and for these galaxies we are able to compute stellar masses. For a given IMF and metallicity, the mass-to-light ratio of a galaxy with a certain stellar population age is modeled. For the initial stellar mass calculations we assume the Kroupa IMF and solar metallicity [Kroupa, 2002]. A solar metallicity is adopted even though our objects have varying metallicities, some sub-solar and some super-solar, because the mass-to-light ratios for varying metallicities yielded negligible differences within the errors of the computed stellar masses.

We interpolate Maraston's tabulated age-$(M/L)_*$ values[1] using the SSP ages determined from the spectral fitting and determine the K band mass-to-light ratio for our quiescent ETGs. To derive the stellar masses we compute the luminosity from the absolute K band magnitude,

$$L_K = L_\odot 10^{0.4(M_\odot - M_K + 1.9)}, \tag{4.1}$$

where $M_\odot$=3.28 in the K band[2] and 1.9 is the Vega to AB K band magnitude offset in the UKIDSS system [Hewett et al., 2006]. The 2005 Maraston mass-to-light ratios are normalized to solar units, so $L_\odot$ is set to unity. Finally, the stellar mass of each

[1] www-astro.physics.ox.ac.uk/∼maraston/SSPn/ml/ml_SSP.tab
[2] www.ucolick.org/∼cnaw/sun.html

galaxy is computed as $M_* = (M/L)_{*K}$ x L_K and the obtained stellar masses for CQGs (as selected for in the next section) with IRAC λ3.6 micron coverage are listed in Table B.3.

4.3 Evaluating Compactness

4.3.1 Comparison Samples

SDSS ($z \sim 0$)

We construct a sample of quiescent, elliptical galaxies from the Sloan Digital Sky Survey DR7 (SDSS) as a local Universe reference sample for our massive compact candidates [Abazajian et al., 2009]. To select for elliptical galaxies, we use the results of SDSS Galaxy Zoo[3] morphological classifications, which relies on the efforts of citizen scientists to classify large numbers of galaxies based on their images [Lintott et al., 2008, Willett et al., 2013]. For our sample, we choose galaxies with a minimum of 10 classifiers where the percentage of classifiers that determined the object to be elliptical is at least 80% as proposed by [Saulder et al., 2013]. The structural parameters, including the circularized effective radius, single component Sérsic index, and axis ratio are taken from [Simard et al., 2011]. The ellipticity of our reference sample was further ensured by only selecting galaxies with axis ratios ≥ 0.7.

The spectroscopic parameters for the SDSS objects were fit for using the same method described in Section 2.3. The velocity dispersions are aperture corrected via

$$\sigma_e = \sigma_r \left(\frac{1.5''}{R_{\rm e,c}} \right)^{.066 \pm .035}, \tag{4.2}$$

[Cappellari et al., 2006], where $1.5''$ is the aperture radius of the SDSS spectrograph, $R_{\rm e,c}$ is the circularized effective radius in arcseconds, and σ_r is the measured velocity dispersion from the spectroscopic fit. Similar to our DEEP2 selection, only galaxies with $\sigma_r < 350$ km s^{-1} and $\sigma_r/\sigma_{error} > 6$ are included in the SDSS comparison sample.

[3] www.galaxyzoo.org

Placing cuts on the equivalent widths of emission lines that usually indicate active star formation ensures the quiescence of the sample. Spectra with equivalent widths > 5 Å of [O II]$\lambda\lambda$3727,3730, [O III]λ5008, Hβ λ4861, and Hα λ6565 are not included in the final SDSS reference sample of 28,802 objects.

We obtain K band photometry for the reference sample from the 10th data release of the UKIRT Infrared Deep Sky Survey (UKIDSS) project [Lawrence et al., 2007]. UKIDSS uses the UKIRT Wide Field Camera [Casali et al., 2007] and the photometric system described in [Hewett et al., 2006]. The pipeline processing and science archive are described in [Irwin, 2008] and [Hambly et al., 2008]. SDSS g and r band magnitudes are K-corrected and used to compute B band and V band absolute magnitudes using the photometric transformations, $B = g + .033(g\text{-}r) + 0.2$ and $V = g$ - $0.58(g\text{-}r)$ - 0.01, as given in [Jester et al., 2005].

Low-redshift CQGs

To place our intermediate redshift, quiescent ETGs into an evolutionary context we compare our sample to their high- and low-redshift counterparts. A low-redshift sample of 23 objects, between $z = 0.2$ and $z = 0.6$, comes from [Damjanov et al., 2013] and [Damjanov et al., 2014] which uses the Baryon Oscillation Spectroscopic Survey (BOSS), which is a spectroscopic survey within SDSS, to identify CQGs by searching for objects photometrically identified as point sources with sizes less than the PSF of $1.5''$. The structural properties of these galaxies are measured by [Damjanov et al., 2013, Damjanov et al., 2014] using `GALFIT`. The stellar masses for the low-redshift sample are computed based on the V band luminosities. To compare the V band derived stellar masses of the low-redshift sample to the K band derived stellar masses of our DEEP2 sample, we add a 0.2 dex offset to the V band stellar masses. As we discuss in Section 5.1.1, we find a 0.2 dex offset between the V band and K band stellar masses of both our $z \sim 0$ SDSS reference sample and our DEEP2 sample.

The candidates are spectroscopically selected for quiescence by requiring the emission doublet EW[O II]$\lambda\lambda$3726,3729 < 5 Å. The spectroscopic parameters of this low-redshift sample are computed in the same way our DEEP2 spectroscopic parameters

are determined as described in Section 2.3. Furthermore, HST imaging of the objects are examined to confirm they are indeed early-type galaxies.

High-redshift Quiescent ETGs

We obtain a sample of 40 high-redshift quiescent galaxies, between $z = 1.0$ and $z = 2.4$, from [van de Sande et al., 2013] who adds quiescent ETGs from their own study to a compiled sample of $z > 1$ quiescent ETGs. Details of the different selection criteria for these 40 quiescent objects can be found in the compilation references in [van de Sande et al., 2013]. The sample of 40 high-redshift quiescent galaxies is not preselected for compactness, but as discussed in Section 1.5, up to 50% of high-redshift massive quiescent galaxies are compact. The stellar masses of the high-redshift sample, given in [van de Sande et al., 2013], are not considered for comparison. Their ages, which are needed to calculate stellar mass, are determined via SED fitting which is likely to yield stellar masses which are offset compared to the stellar masses based on ages determined by `PEGASE.HR` for our DEEP2 sample and low-redshift SDSS/BOSS comparison sample.

4.3.2 Compactness Selection

There are several measures that can be used to determine the compactness of an ETG. We consider three different methods for defining compactness that have been utilized in previous studies. In [Barro et al., 2013], compactness is defined by $M^*/R_{e,c}^{1.5}$, which is in between $M^*/R_{e,c}$ and the stellar mass surface density, $M^*/R_{e,c}^2$, both of which exhibit strong correlation with the star formation rate (SFH) and color [Franx et al., 2008]. Objects with $\log(M^*/R_{e,c}^{1.5}) \geq 10.3$ $M_\odot$ $kpc^{-1.5}$ are defined as compact. Placing a constant effective radius cuts another method of defining compactness. A commonly used radius boundary, as adopted in [van der Wel et al., 2011], is that an ETG is considered compact if $R_{e,c} \leq 2.0$ kpc. But the most widely used and robust compactness cut is one in the M_{dyn}-$R_{e,c}$ plane as demonstrated in studies such as [Damjanov et al., 2013, Damjanov et al., 2014]. While we consider the other

two methods for defining compactness, we ultimately decide to adopt the mass-size cut to select our final sample of CQGs. To make a mass-size cut on compactness we use the SDSS reference sample of $z \sim 0$ massive elliptical galaxies described in the previous section.

As discussed in Section 1.3.2, the dynamical mass of an ETG can be derived from the virial theorem. For our sample of quiescent DEEP2 ETGs with measured velocity dispersions and sizes, we compute the dynamical masses using Equation 1.4 where the scaling factor β is found to be 5.0 ± 0.1 based on calibrating the virial mass estimate to more complex dynamical modeling of low-redshift early-type galaxies with spatially resolved spectroscopy and kinematic information [Cappellari et al., 2006]. As described in Section 1.3.2 this formulation of dynamical mass assumes a purely pressure supported system; therefore, the dynamical mass for objects that may also have a disk component, which are rotationally supported, will be underestimated.

Figure 4-1 displays the velocity dispersion σ, sizes $R_{e,c}$, and dynamical M_{dyn} and stellar M^* masses of the DEEP2 quiescent ETGs, the SDSS $z\sim0$ reference sample, and high- and low-redshift comparison samples. Panel a of Figure 4-1 shows $M^*/R_{e,c}^{1.5}$ against velocity dispersion σ where objects falling above the relation at $\log(M^*/R_{e,c}^{1.5}) \geq 10.3$ $M_\odot$ $kpc^{-1.5}$ are defined as compact. When applied to the DEEP2 sample, this cut defines 76 of the 222 DEEP2 quiescent ETGs as compact. Panel b of Figure 4-1 shows that while the velocity dispersion range of our quiescent ETGs is similar to that of the SDSS sample of local normal ETGs, there is a greater spread in the sizes of our DEEP2 quiescent ETGs at $0.5 < z < 1.1$. In addition to there being normal ETGs in our sample with sizes greater than $\sim$ 2 kpc, there are a number of ETGs in the sample with smaller sizes. Applying the compactness cut in this plane at $R_{e,c} \leq 2.0$ kpc, as adopted in [van der Wel et al., 2011], 62 of the 222 DEEP2 quiescent ETGs are rendered compact.

Panel c of Figure 4-1 shows the effective radius, $R_{e,c}$, against dynamical mass, M_{dyn}, of the DEEP2 quiescent ETGs and comparison samples. Note the offset between the SDSS sample and DEEP2 and comparison samples. While there is a population of the DEEP2 quiescent ETGs that fall along the local ETG relation, a

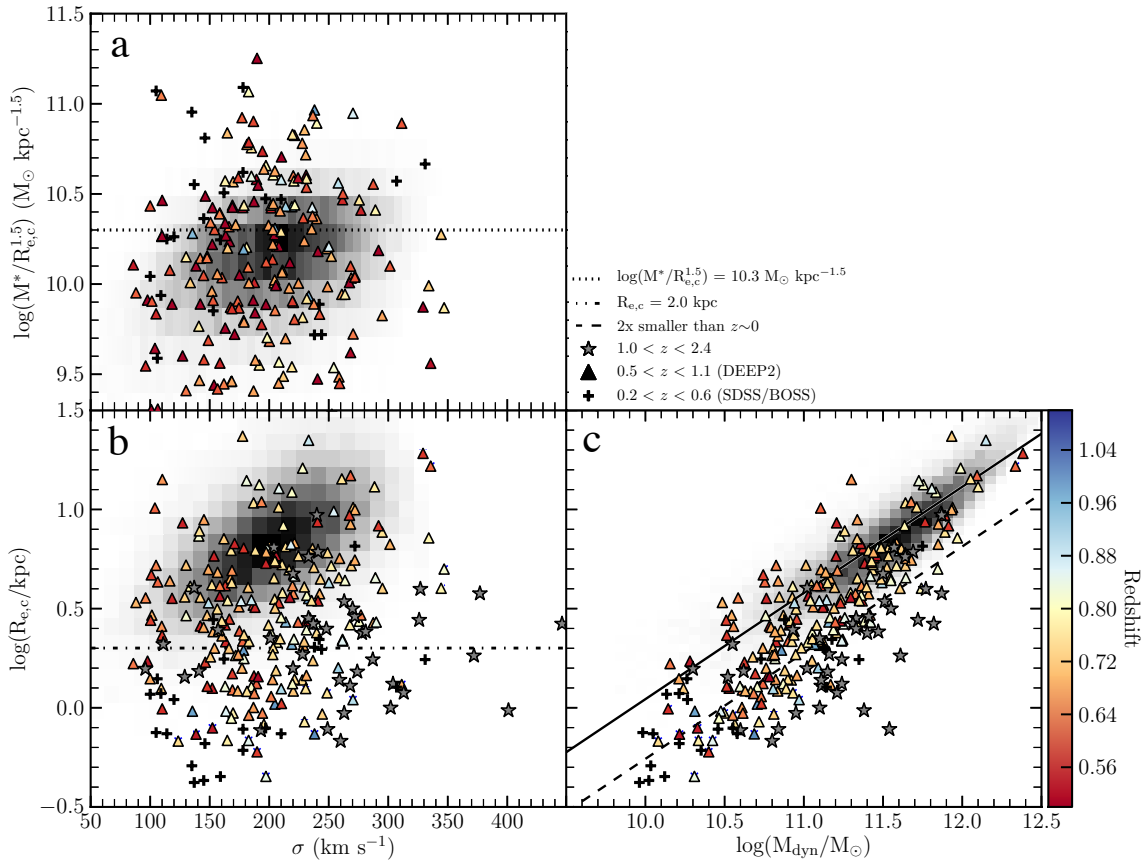

Figure 4-1 Derived properties of our DEEP2 quiescent ETGs and comparison samples. Throughout the three plots, the triangles are our DEEP2 massive compact candidates colored by redshift, the grey histogram is the SDSS reference sample at $z \sim 0$, the black pluses are the low-redshift SDSS/BOSS comparison sample of CQGs, and the grey stars are the high-redshift comparison sample from the compilation presented in [van de Sande et al., 2013]. For visual clarity, we do not include the error bars. Panel a shows the log of $M^*/R_{e,c}^{1.5}$ against velocity dispersion with galaxies above the horizontal line at $\log(M^*/R_{e,c}^{1.5}) = 10.3$ $M_\odot$ $kpc^{-1.5}$ defined as compact. Panel b displays the log of the effective radius against velocity dispersion with a compactness boundary line at $R_{e,c} = 2.0$ kpc. Panel c shows the log of the effective radius against log of the dynamical mass where the solid line is the best fit to the SDSS, $z \sim 0$ reference sample and the dashed line is the compactness boundary as defined by being two times smaller than the $z \sim 0$ reference sample in the M_{dyn}-$R_{e,c}$ plane.

number of our DEEP2 galaxies are offset from this relation along with the high- and low-redshift comparison samples. To define compactness in this parameter space we fit a linear relation to the local SDSS sample of massive ETGs that we find to be,

$$\log R_{e,c} = 0.54 \times \log M_{dyn} - 5.31, \tag{4.3}$$

and define compactness as being two times smaller than this relation, informed by observations of high-redshift CQGs being 2-5 times smaller than local massive ETGs (as discussed in Section 1.5.1). This definition of compactness renders 52 of the 222 quiescent ETGs as compact. The spectroscopic and structural properties of the 52 DEEP2 CQGs are listed in Table B.1 and B.2 respectively.

While the number of compact, quiescent galaxies yielded depends on the chosen definition of compactness, Figure 4-1 demonstrates that our intermediate redshift DEEP2 galaxies bridge the gap between all of the displayed structural properties of low- and high-redshift compact galaxies. We give preference to the mass-size cut because it is the most widely used cut and therefore our sample can be compared to a larger number of studies. Additionally, this formulation of compact defines compactness for a given dynamical mass, which is particularly favorable for evolutionary studies where the characteristic mass of compact galaxies may vary with redshift.

4.4 Number Density Constraints

Of the population of 222 DEEP2 quiescent ETGs in the redshift range $0.5 < z < 1.1$ we find 52 galaxies to be compact under the M_{dyn}-$R_{e,c}$ criterion (Equation 4.3), which is $(23 \pm 3)\%$ of the parent population. The error is computed assuming a binomial distribution where the number of observations is the total number of galaxies in the parent sample and the 'success' rate is the fraction of compacts in the sample. This percentage of CQGs is likely an upper limit on the percentage of CQGs at $0.5 < z < 1.1$. As discussed in Section 2.2.3, the DEEP2 survey is likely biased towards massive compacts in its target selection because a flux-limited spectroscopic survey will tend to identify the most concentrated objects with the highest signal-

to-noises. Additionally, bias towards massive compacts could have been introduced in the spectral fitting. The higher the age and metallicity of an object the more precisely `PEGASE.HR` is able to determine velocity dispersion. This lends itself to excluding galaxies with younger SSP ages from our DEEP2 parent population due to the σ/σ_{error} cut. If a majority of these younger, excluded galaxies are not quiescent, then this is likely a source that could be inflating our compact percentage.

While we are unable, at this time, to formally determine the number density of CGQs in the range $0.5 < z < 1.1$ due to the complexity of our selection criteria, we are able to compare our percentage of compact galaxies in the DEEP2 parent sample of massive quiescent galaxies to the percentages found in other studies. Defining compactness as one standard deviation below the mass-size relation of a local Universe SDSS sample, [Cassata et al., 2011] finds $\sim 60\%$ of massive quiescent galaxies at $z = 1.1$ and $\sim 35\%$ of massive quiescent galaxies at $z = 0.5$ to be compact. The study also defines ultra-compactness as being 0.4 dex (or 2.5 times) below the mass-size relation of the SDSS sample, where $\sim 20\%$ of massive quiescent galaxies at $z = 1.1$ and $\sim 10\%$ of massive quiescent galaxies at $z = 0.5$ are found to be ultra compact. Our definition of mass-size compactness being 2 times below the local Universe SDSS reference sample falls between the compact and ultra-compact definitions in [Cassata et al., 2011] but is closer to the ultra-compact definition. While the percentage of compacts we find in our parent sample of DEEP2 massive quiescent galaxies is greater than the percentage of compacts found in other survey fields, this is consistent with our result of $(23 \pm 3)\%$ being an upper limit on the percentage of CQGs in the redshift range $0.5 < z < 1.1$.

4.5 Property Comparison

Now that we have identified a sample of CQGs in the redshift range $0.5 < z < 1.1$ we can begin to compare their spectroscopic properties to the spectroscopic properties of their non-compact parent sample from which they were drawn. To compare the distributions of redshift, SSP ages, and metallicities of the compact versus non-compact

DEEP2 quiescent ETG samples we utilize the Mann-Whitney rank-sum test, which is the nonparametric equivalent to the t-test. The nonparametric Mann-Whitney rank-sum test is appropriate to account for the discrepancy in the sample sizes (52 compacts versus 199 non-compacts) and for the non-normal distributions of the spectroscopic properties, especially age and metallicity, as seen in Figure 2-6. Figure 4-2 shows the redshift, age, and metallicity box plots of the compact and non-compact samples.

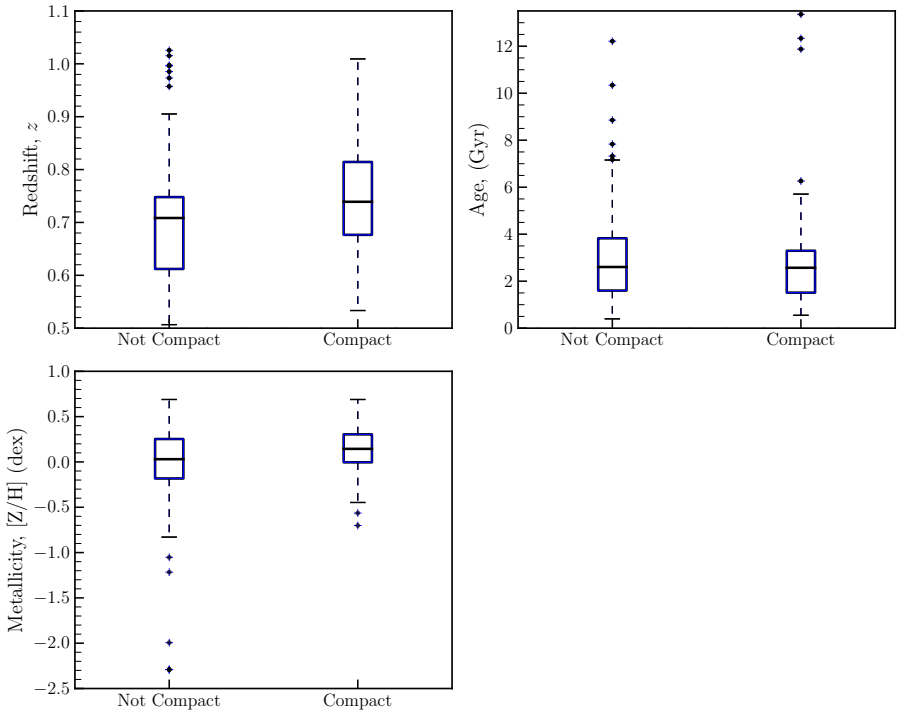

Figure 4-2 Box plots showing the distributions of redshift (z), age, and metallicity ([Z/H]) of the compact and non-compact samples. The distribution non-compact versus compact redshifts and metallicities is statistically significant.

The median redshifts of the compact and non-compact sample are $z = 0.739$ and $z = 0.708$ respectively. Comparing the non-compact and compact samples, the U-statistic is -3.0 and the p-value is .003 indicating that there is only a .3% chance the two distributions were drawn from the same sample. The difference in redshift distributions of the non-compact and compact sample is statistically significant with the compact sample redshifts being higher on average. This result supports the

expectation discussed in Section 1.5.1 that there are a larger number of compact ETGs in the early Universe than in the more local Universe.

The median ages of the ages of the compact and non-compact sample are 2.57 Gyr and 2.60 Gyr respectively. Comparing the non-compact and compact samples, the U-statistic is 0.6 and the p-value is .5 indicating that there is 50% chance the two distributions were drawn from the same sample. So there is no significant difference between the SSP ages of the compact and non-compact samples. The median metallicities of the compact and non-compact sample are 0.14 dex and 0.03 dex respectively. Comparing the non-compact and compact samples, the U-statistic is -2.0 and the p-value is .02 indicating that there is 2% chance the two distributions were drawn from the same sample. The difference in metallicities distributions of the non-compact and compact sample is statistically significant with the compact sample having a higher metallicity on average. Further investigation of the metallicities of CQGs is left for future work.

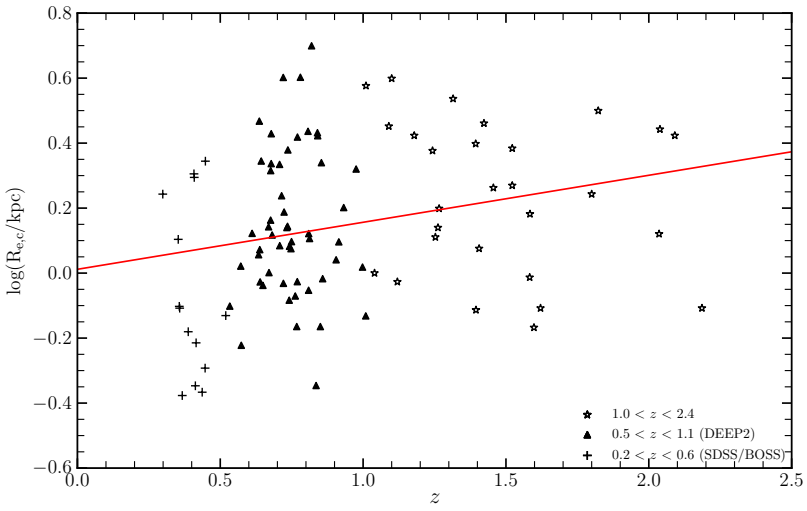

Figure 4-3 Redshift, z, versus size, $R_{e,c}$, for CQGs in the range $0.2 < z < 2.4$. The triangles are our DEEP2 CQGs, the black pluses are the low-redshift SDSS/BOSS comparison sample of CQGs, and the grey stars are the high-redshift CQGs from the compilation presented in [van de Sande et al., 2013].

Now that we've identified a sizable population of CQGs at intermediate redshifts $0.5 < z < 1.1$ we can begin preliminary studies of the evolution of CQGs themselves. Applying our mass-size compactness criterion (Equation 4.2) we define 14 of the 23 $0.2 < z < 0.6$ SDSS/BOSS [Damjanov et al., 2013, Damjanov et al., 2014] galaxies as compact and 28 of the 40 $1.0 < z < 2.4$ from [van de Sande et al., 2013] as compact. Figure 4-3 shows the size, $R_{e,c}$, against redshift, z, of CGQs from $z = 0.2$ to $z = 2.4$.

$$\log R_{e,c} = 0.14 \times z + 0.012. \tag{4.4}$$

There is only a weak correlation ($R^2 = 0.25$) of CQG size with the high-redshift CQGs being larger than the low-redshift CQGs. The continued study of the properties of CQGs across the range $z = 0.2$ to $z = 2.4$ is the subject of future work.

4.6 Redshift of Quenching

To begin to trace the evolutionary history of CQGs we determine the redshifts of star formation quenching, which is indicative of when these CQGs became quiescent, of the DEEP2 and SDSS/BOSS CQGs. The redshift of quenching is calculated by subtracting the SSP age of each galaxy from the age of the Universe at each galaxy's redshift of observation. The redshifts corresponding to the age of the Universe at galaxy formation is found using a redshift-age interpolation function[4].

As shown in Figure 4-4, our sample of CQGs is appears to be drawn from two epochs of star formation quenching: quenching at $z > 2$ which suggests these objects may be the descendants of the observed high-redshift CQGs and quenching at $z \leq 2$ which suggests there is an additional population of CQGs that formed analogously to the CQGs observed at $z \sim 2$. Only 7 of our 52 DEEP2 CQGs quenched at redshifts large enough to be possible descendants. We observe a similar epoch sampling for the SDSS/BOSS $0.2 < z < 0.6$ CQGs; of the 23 low-redshift CQGs, 3 formed at redshifts large enough to be descendants of $z \sim 2$ massive compact galaxies. While the low-redshift compact quiescent sample is, on average, younger than the DEEP2

[4]http://roban.github.com/CosmoloPy/

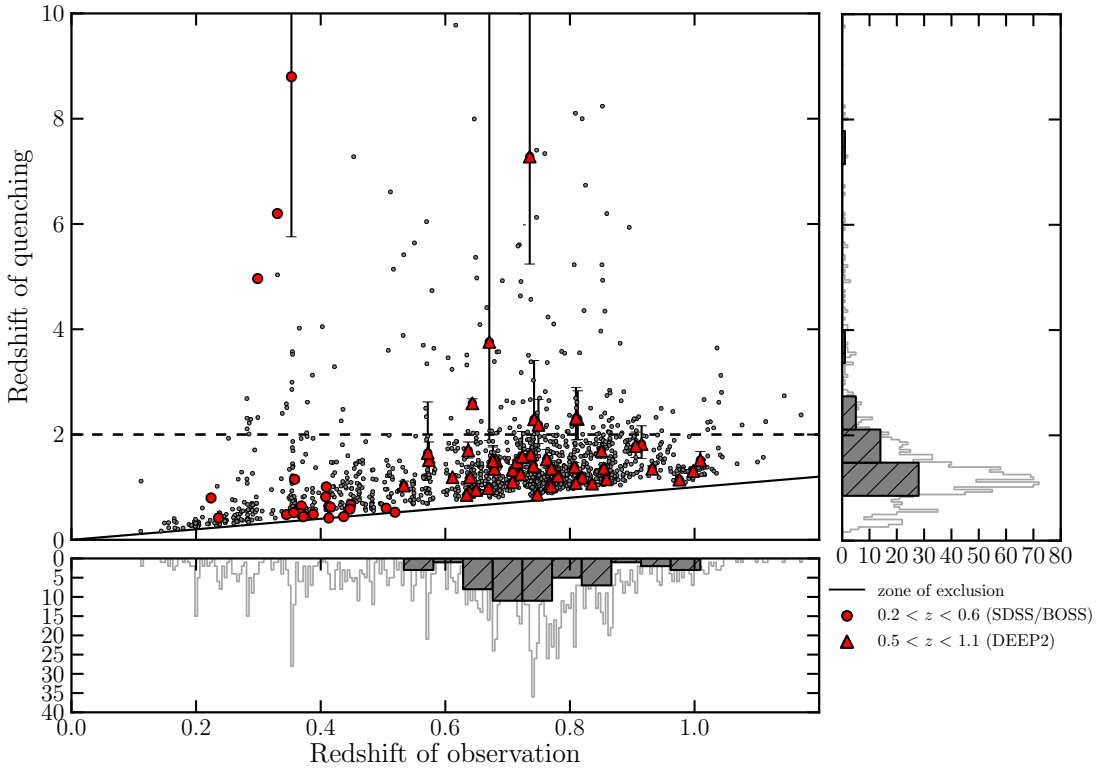

Figure 4-4 Redshift of star formation quenching against redshift of observation. The solid line indicates where the redshift of quenching and observation are equal (below which is the zone of exclusion). Objects above the dashed line at $z_{quench} = 2$ are possible descendants of the high-redshift compact population. The 52 DEEP CQGs are indicated by triangles (and solid grey histogram) and the circles are the 23 SDSS/BOSS CQGs. The grey points (and grey historgram) represent objects from the full DEEP2 sample that meet $\sigma/\sigma_{error} > 6$ and $10 < \sigma < 350$ km s^{-1} (1427 galaxies are in the final sample). The plot shows that our compact candidates in the range $0.5 < z_{obs} < 1.1$ appear to uniformly sample the epoch of quenching range of the DEEP2 galaxies in the same observation bin. The few galaxies whose stars formed very close to when they are observed are younger, post-starburst galaxies.

sample, there are older outliers in the sample. Further study of the stellar populations of CQGs intermediate to the two observed epochs of quenching is an opportunity to constrain the evolutionary histories massive quiescent ETGs.

The epochs of quenching for the DEEP2 and SDSS/BOSS samples are dependent on the best fit SSP ages determined by the spectroscopic fitting. To ensure that a SSP model appropriately describes the stellar populations of the galaxies, we additionally fit the DEEP2 spectra with an exponentially declining model of star formation history. Exponentially declining models of star formation history are generally more realistic and give a more nuanced description of stellar systems than SSP models. For each CQG we assume that star formation began at high-redshift, soon after the Big Bang, and after the star formation rate declined exponentially with the timescale τ. From these fits we determine, similar to the SSP fits, a metallicity [Z/H] and velocity dispersion σ for each galaxy. Long exponentially declining timescales τ correspond to young SSP ages, so galaxies with young SSP ages had their star formation quenched more rapidly than galaxies with older SSP ages. As demonstrated by Figure 4-5, initial comparisons of the SSP and exponentially declining models for our DEEP2 galaxies in agreement; therefore, the redshift of star formation quenching based on the SSP ages place the galaxies at reliable epochs of quenching.

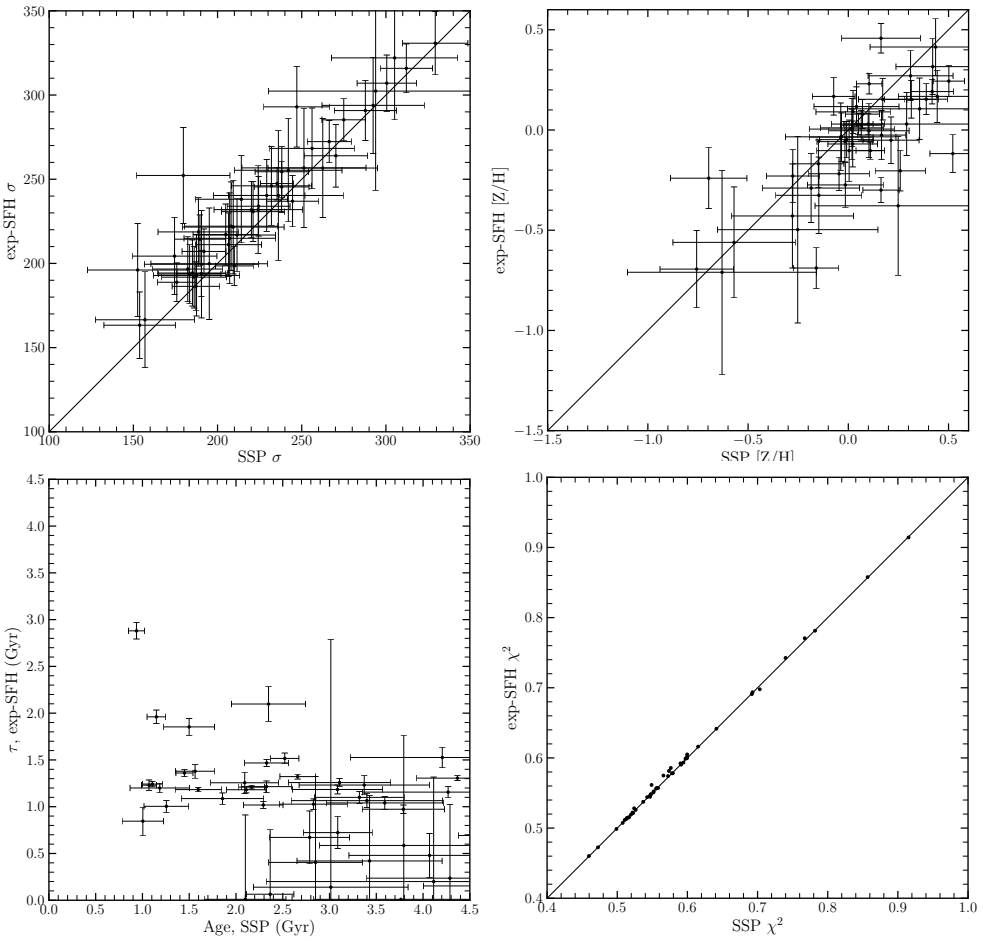

Figure 4-5 Comparison of SSP and exponentially declining SFH velocity dispersions σ, metallicities [Z/H], age measures, and χ^2 of the spectral fit for the 52 CQGs in our DEEP2 sample.

Chapter 5

Conclusions

5.1 Preliminary and Future Work

5.1.1 Stellar versus Dynamical Mass: Constraining the IMF

With the initial goal of investigating the dark matter content at the center of our CQGs, we compare the computed virial masses to the stellar masses derived from Maraston models. Figure 5-1 displays the dynamical mass against the stellar mass of the 43 DEEP2 CQGs with stellar mass estimates and the $z \sim 0$ SDSS reference sample. While some of our candidates lie along the dynamical-stellar mass one-to-one line, suggesting these galaxies do not contain dark matter within one effective radius, our SDSS reference also appears to contain little dark matter. While the distribution of the reference sample does lie slightly above the one-to-one line, previous studies show that these types of non-compact elliptical galaxies have higher dynamical masses [Belli et al., 2014].

One possibility for the low dark matter content implied for the SDSS reference sample is that an inherent bias in the Galaxy Zoo classification may lead to more compact ellipticals being preferentially selected, but the separation of the reference sample and compact objects in the other parameter plots (Figure 4-1) suggests this is likely not the case.

We compute the stellar mass for the SDSS reference sample based on the B band

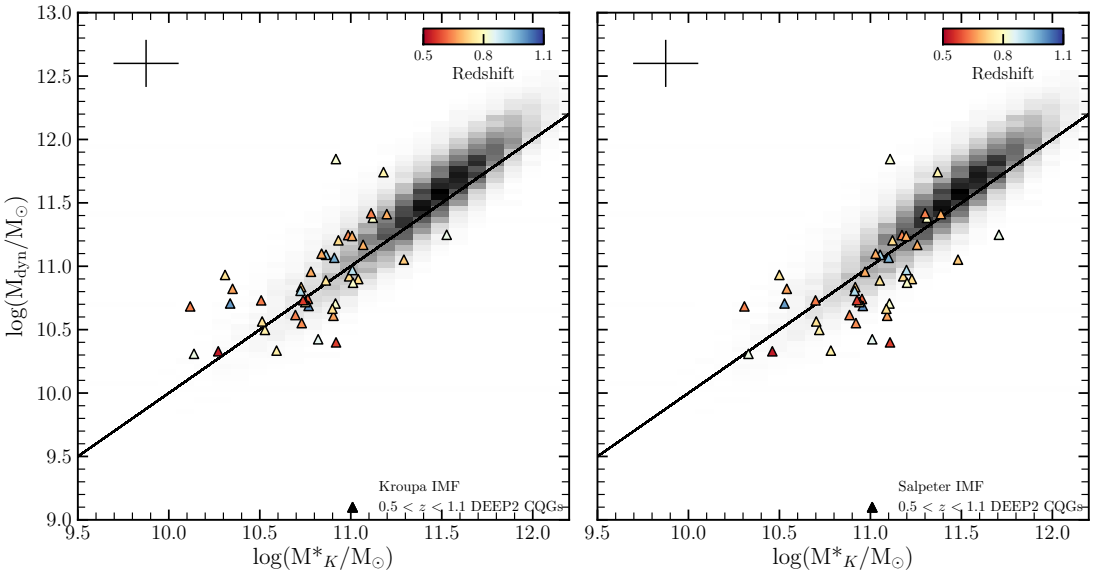

Figure 5-1 Log of dynamical mass, M_{dyn} against log of stellar mass, M^*_K, where the black line indicates the one-to-one relation. The grey histogram shows the distribution of the SDSS, $z \sim 0$ reference sample and the triangles are the 43 DEEP2 CQGs, colored according to redshift, with stellar mass estimates. The plot on the left shows the DEEP2 CQG stellar masses computed using a Kroupa IMF while the plot on the right shows the stellar masses computed with a Salpeter IMF. The median error bars are shown in the upper left corner.

and V band stellar masses by transforming the g and r band photometry (Section 3.1) and using the appropriate Maraston mass-to-light ratios. We find that the stellar masses computed from the B band and V band agree very well with one another, but there is a significant discrepancy between the B, V band and K-band stellar masses. Our stellar masses based on the K band are approximately 0.2 dex larger than the B band and V band based stellar masses. To determine whether or not this discrepancy is due to our photometry or the UKIDDS to SDSS K band magnitude offset, we also compute the stellar masses of the DEEP2 sample based on the B band and V bands. Just as with the SDSS reference sample, the B band and V band stellar masses agree very well for the DEEP2 candidates and the K band stellar mass is approximately 0.2 dex larger than both the B band and V band stellar masses.

This same discrepancy between the stellar masses computed using B band, V band and K band in both the DEEP2 and SDSS sample suggests the problem may not

lie with the photometry or magnitude offsets, but with the chosen Maraston models not being representative of the true star formation history or stellar content of these galaxies. Mass-to-light ratio modeling that is more realistic to the stellar properties of our massive quiescent galaxies may be needed to resolve these discrepancies.

Despite the unresolved separation between the $z \sim 0$ sample and our DEEP2 sample of massive quiescent galaxies in the stellar and dynamical mass plane, our results suggest that a more bottom-heavy IMF is unphysical for our sample of DEEP2 CQGs. As shown in Figure 5-1, adopting the bottom-heavy Salpeter IMF results in the CQGs having stellar masses larger than their dynamical masses. Therefore, a bottom-heavy IMF is unphysical for our massive quiescent galaxies because it suggests they contain negative dark matter. This preliminary result is in tension with [Cappellari et al., 2012] and [Conroy et al., 2013] that claim the IMF becomes increasing bottom heavy for massive, early-type galaxies.

5.2 Summary

In this thesis, we identify a sample of 222 massive quiescent ETGs at intermediate redshifts, $0.5 < z < 1.1$, by mining the DEEP2 Redshift Survey. From the spectra, fit against a grid of `PEGASE.HR` SSP models based on the MILES stellar library, the velocity dispersions, SSP ages, and metallicities of the DEEP2 galaxies are determined. Quiescence is selected for by requiring EW[O II]$\lambda\lambda$3727,3730, EW Hβ λ4863, EW[O III]$\lambda\lambda$4960,5008, and EW[O III]λ4364 all < 5 Å and by visually selecting objects without strong emission line fluxes. The structural properties, including the half-light radii, axis ratios, and Sérsic indices, of this sample of 222 ETGs are derived from HST ACS and WFPC2 F814W imaging. Aditionally, we derive the stellar masses of the sample based on IRAC/SPIZTER photometry and K Band Maraston mass-to-light ratios. From the study of these intermediate-redshift quiescent ETGs, we find:

- 222 quiescent ETGs with half-light radii ranging from $0.45 < \mathrm{R_{e,c}} < 36.75$ kpc (mean $\mathrm{R_{e,c}} = 2.59$ kpc) and dynamical masses between $1.20{\times}10^{10}$ and $2.47{\times}10^{12}$ $\mathrm{M_\odot}$ (mean $\mathrm{M_{dyn}} = 2.50{\times}10^{11}$ $\mathrm{M_\odot}$).

- of 222 ETGs, 52 are compact with sizes less than half the size of their SDSS $z \sim 0$ counterparts. Their half-light radii range from $0.45 \leq \mathrm{R_{e,c}} \leq 5.01$ kpc (mean $\mathrm{R_{e,c}} = 1.62$ kpc) and dynamical masses range from $1.20{\times}10^{10} \leq \mathrm{M_{dyn}} \leq 2.45{\times}10^{12}$ $\mathrm{M_\odot}$ (mean $\mathrm{M_{dyn}} = 1.35{\times}10^{10}$ $\mathrm{M_\odot}$).

- the sample of CGQs is drawn from two epochs of star formation quenching: 5 quenched at $z > 2$ making them possible descendants of the observed high-redshift CQGs and 47 quenched at $z \leq 2$ which suggests there is a larger population of CQGs that joined the quiescent population analogous to observations of high-redshift CQGs at $z \sim 2$.

- the comparison of stellar and dynamical mass for the DEEP2 CQGs shows that a more bottom-heavy, Salpeter IMF is unphysical for these objects. This result, which merits further study, is in tension with recent IMF developments

that claim the IMF becomes increasing bottom-heavy for massive, early-type galaxies.

Appendix A

Acronym Glossary

ACS	Advanced Camera for Surveys
AEGIS	All-Wavelength Extended Groth Strip International Survey
AGN	Active Galactic Nucleus
BOSS	Baryon Oscillation Spectroscopic Survey
CADC	Canadian Astronomy Data Centre
CANDELS	Cosmic Assembly Near-IR Deep Extragalactic Legacy Survey
CHFT	Canada France Hawaii Telescope
CQG	Compact Quiescent Galaxy
DEEP	Deep Extragalactic Evolutionary Probe
EGS	Extended Groth Strip
HLA	Hubble Legacy Archive
HST	Hubble Space Telescope
IMF	Initial Mass Function
IRAC	The Infrared Array Camera
PSF	Point Spread Function
SDSS	Sloan Digital Sky Survey
SED	Spectral Energy Distribution
SFH	Star Formation History
SMG	Sub-millimeter Galaxy

SSP	Simple Stellar Population
UKIDSS	The UKIRT Infrared Deep Sky Survey
UKIRT	The UK Infrared Telescope
WFC3	Wide Field Camera 3
WFPC2	Wide Field Planetary Camera 2

Appendix B

DEEP2 CQG Property Tables

Table B.1. Spectroscopic Parameters of DEEP2 CQGs

Object Number	α [°]	δ [°]	z	σ [km s^{-1}]	SSP Age [Gyr]	[Z/H] [dex]	Spectral Class
(1)	(2)	(3)	(4)	(5)	(6)	(7)	(8)
12004492	214.32658	52.4276	0.533	152 ± 21	2.57 ± 0.30	-0.02 ± 0.32	Old
12007960	214.51040	52.4690	0.708	220 ± 24	2.48 ± 0.26	0.03 ± 0.22	Old
12015693	214.65143	52.5960	0.835	197 ± 24	0.98 ± 0.04	0.65 ± 0.14	Old
12016013	214.57689	52.6178	0.643	262 ± 17	5.02 ± 0.08	0.69 ± 0.00	Old
12016769	214.40033	52.5986	0.612	189 ± 18	2.62 ± 0.23	-0.06 ± 0.25	Old
12019899	214.68512	52.6372	0.932	258 ± 20	1.44 ± 0.15	0.20 ± 0.10	Old
12019978	214.63535	52.6720	0.733	228 ± 16	2.94 ± 0.23	-0.02 ± 0.18	Old
12023935	214.78560	52.6827	0.841	240 ± 31	12.3 ± 5.9	-0.45 ± 0.32	Old
12024057	214.74437	52.7128	0.736	221 ± 16	6.26 ± 0.38	0.16 ± 0.13	Old
12025292	214.50116	52.7079	0.813	185 ± 17	3.76 ± 0.56	-0.02 ± 0.15	Old
12028330	214.79457	52.7840	0.820	347 ± 33	1.46 ± 0.15	0.62 ± 0.15	Old
12028633	214.64512	52.7639	0.682	311 ± 15	3.07 ± 0.18	0.22 ± 0.11	Old
13010942	214.92454	52.8562	0.671	187 ± 21	5.7 ± 1.8	-0.09 ± 0.24	Old
13011281	214.81655	52.8704	0.807	276 ± 22	2.10 ± 0.23	0.37 ± 0.15	Old
13011501	214.83094	52.8817	1.009	238 ± 36	1.55 ± 0.36	0.14 ± 0.34	Old
13011780	214.80840	52.8707	0.810	220 ± 22	3.80 ± 0.60	0.01 ± 0.15	Old
13011811	214.79813	52.8479	0.640	194 ± 15	2.43 ± 0.21	0.00 ± 0.20	Old
13019286	214.84968	52.9108	0.737	240 ± 15	3.04 ± 0.16	0.28 ± 0.14	Old
13019294	214.90051	52.9063	0.850	183 ± 23	2.62 ± 0.30	-0.70 ± 0.27	Post-starburst
13019956	214.80987	52.9196	0.780	344 ± 18	1.75 ± 0.12	0.38 ± 0.11	Old
13025465	215.19902	52.9984	0.677	229 ± 19	3.14 ± 0.58	0.01 ± 0.15	Old
13027468	214.90422	52.9913	0.768	165 ± 27	1.30 ± 0.24	0.44 ± 0.33	Old
13033804	215.20167	53.0384	0.742	181 ± 17	4.12 ± 0.99	-0.01 ± 0.18	Old
13033944	215.14857	53.0283	0.763	230 ± 29	2.70 ± 0.41	0.28 ± 0.26	Old
13033965	215.14324	53.0153	0.749	231 ± 17	3.94 ± 0.56	0.14 ± 0.11	Old
13034447	215.06028	53.0239	0.748	249 ± 17	0.55 ± 0.03	0.32 ± 0.15	Post-starburst
13034602	215.03830	53.0428	0.715	237 ± 9	2.83 ± 0.10	-0.05 ± 0.10	Old
13035280	215.01947	53.0481	0.915	210 ± 26	2.57 ± 0.55	0.26 ± 0.33	Old
13041525	215.30160	53.0890	0.998	205 ± 24	1.06 ± 0.14	0.32 ± 0.42	Old
13041606	215.30910	53.1176	0.678	262 ± 13	2.73 ± 0.13	0.10 ± 0.12	Old
13042259	215.21909	53.0765	0.770	170 ± 10	1.11 ± 0.06	0.15 ± 0.09	Post-starburst
13043062	215.10056	53.0814	0.976	219 ± 9	0.63 ± 0.02	0.29 ± 0.10	Post-starburst
13049589	215.23905	53.1617	0.638	187 ± 15	1.41 ± 0.10	0.69 ± 0.00	Old
13049865	215.24372	53.1455	0.678	287 ± 18	2.69 ± 0.12	0.03 ± 0.12	Old
13057571	215.39590	53.2023	0.676	231 ± 21	3.09 ± 0.58	0.09 ± 0.24	Old
13057979	215.23158	53.2030	0.741	196 ± 24	2.50 ± 0.47	0.31 ± 0.21	Old

Table B.1 (cont'd)

Object Number	α [°]	δ [°]	z	σ [km s^{-1}]	SSP Age [Gyr]	[Z/H] [dex]	Spectral Class
(1)	(2)	(3)	(4)	(5)	(6)	(7)	(8)
13058221	215.31695	53.1961	0.634	202 ± 14	1.15 ± 0.07	-0.07 ± 0.14	Old
13058803	215.21206	53.2069	0.637	277 ± 13	3.77 ± 0.31	0.15 ± 0.08	Old
13064321	215.40909	53.2475	0.669	203 ± 18	1.52 ± 0.18	0.25 ± 0.12	Old
13064634	215.30968	53.2586	0.906	270 ± 36	2.55 ± 0.45	0.13 ± 0.38	Old
41032729	36.53967	0.58090	0.770	268 ± 30	2.21 ± 0.41	0.30 ± 0.19	Old
42037703	37.60768	0.63040	0.854	262 ± 25	1.81 ± 0.21	0.37 ± 0.23	Old
42029812	37.61381	0.59320	0.858	164 ± 23	1.16 ± 0.12	0.37 ± 0.34	Old
42033566	37.28237	0.56260	0.840	290 ± 19	13.3 ± 3.0	-0.31 ± 0.17	Old
13101995	215.05671	52.8985	0.574	190 ± 24	3.76 ± 0.71	0.16 ± 0.15	Old
11013870	213.87992	52.0745	0.649	183 ± 14	1.48 ± 0.10	0.12 ± 0.10	Old
11019658	213.90904	52.1240	0.572	210 ± 23	4.08 ± 1.41	0.00 ± 0.22	Old
31008760	351.60017	-0.0330	0.809	168 ± 24	1.14 ± 0.17	0.15 ± 0.26	Old
41019260	37.12902	0.5079	0.721	245 ± 37	11.9 ± 5.7	-0.56 ± 0.35	Old
41019373	37.13189	0.5085	0.723	206 ± 32	3.02 ± 0.88	-0.16 ± 0.44	Old
41020051	37.11260	0.5353	0.708	229 ± 23	1.75 ± 0.18	0.10 ± 0.15	Old
41020361	37.12607	0.5078	0.721	295 ± 18	2.16 ± 0.22	0.38 ± 0.12	Old

Note. — (1) DEEP2 identification number; (2) Right ascension; (3) Declination; (4) Redshift; (5) Velocity dispersion; (6) Age of the best fit simple stellar population model; (7) Metallicity of the best fit simple stellar population model; (8) Spectral class based on visual inspection

†Metallicities outside of the range -0.50 < [Z/H] dex < 0.40 are close to the SSP model limits where determined ages are less reliable

Table B.2. Structural Parameters of DEEP2 CQGs

Object Number	$R_{e,c}$ [kpc]	$n_{Sérsic}^{single}$	q^{single}	$\log(M_{dyn}/M_{\odot})$
(1)	(2)	(3)	(4)	(5)
12004492	0.791 ± 0.008	3.34 ± 0.06	0.38	10.33 ± 0.28
12007960	1.21 ± 0.02	4.13 ± 0.08	0.48	10.84 ± 0.22
12015693	0.45 ± 0.01	3.3 ± 0.1	0.26	10.31 ± 0.25
12016013	2.21 ± 0.02	2.48 ± 0.02	0.63	11.25 ± 0.13
12016769	1.32 ± 0.01	4.48 ± 0.05	0.32	10.74 ± 0.19
12019899	1.59 ± 0.05	8.0 ± 0.2	0.43	11.09 ± 0.16
12019978	1.38 ± 0.01	3.07 ± 0.04	0.3	10.92 ± 0.14
12023935	2.64 ± 0.03	2.44 ± 0.03	0.49	11.25 ± 0.26
12024057	1.39 ± 0.02	3.89 ± 0.06	0.46	10.90 ± 0.14
12025292	1.23 ± 0.02	4.39 ± 0.09	0.56	10.71 ± 0.19
12028330	5.01 ± 0.08	3.51 ± 0.04	0.62	11.85 ± 0.19
12028633	1.31 ± 0.01	3.75 ± 0.04	0.32	11.17 ± 0.10
13010942	1.00 ± 0.01	4.15 ± 0.08	0.36	10.61 ± 0.23
13011281	2.73 ± 0.05	3.78 ± 0.05	0.73	11.38 ± 0.17
13011501	0.739 ± 0.007	2.56 ± 0.05	0.15	10.69 ± 0.30
13011780	1.32 ± 0.01	2.27 ± 0.04	0.27	10.87 ± 0.20
13011811	0.940 ± 0.008	4.79 ± 0.05	0.27	10.62 ± 0.15
13019286	2.39 ± 0.05	5.28 ± 0.09	0.59	11.20 ± 0.13
13019294	0.685 ± 0.009	3.77 ± 0.09	0.67	10.42 ± 0.26
13019956	4.01 ± 0.05	3.90 ± 0.04	0.77	11.74 ± 0.11
13025465	2.07 ± 0.02	2.49 ± 0.03	0.53	11.10 ± 0.17
13027468	0.69 ± 0.01	3.1 ± 0.1	0.79	10.33 ± 0.33
13033804	1.21 ± 0.02	3.80 ± 0.07	0.34	10.66 ± 0.19
13033944	0.85 ± 0.01	3.08 ± 0.05	0.5	10.72 ± 0.25
13033965	1.25 ± 0.01	2.75 ± 0.04	0.32	10.89 ± 0.15
13034447	1.19 ± 0.01	3.05 ± 0.03	0.4	10.93 ± 0.14
13034602	1.73 ± 0.03	5.26 ± 0.07	0.52	11.05 ± 0.08
13035280	1.25 ± 0.04	4.0 ± 0.1	0.73	10.81 ± 0.25
13041525	1.04 ± 0.02	4.3 ± 0.2	0.66	10.71 ± 0.24
13041606	2.17 ± 0.03	5.87 ± 0.06	0.65	11.24 ± 0.10
13042259	0.941 ± 0.006	3.71 ± 0.05	0.5	10.50 ± 0.12
13043062	2.09 ± 0.02	4.49 ± 0.04	0.89	11.07 ± 0.08
13049589	1.18 ± 0.02	2.52 ± 0.04	0.52	10.68 ± 0.17
13049865	2.69 ± 0.01	2.36 ± 0.01	0.76	11.41 ± 0.13
13057571	1.45 ± 0.03	5.64 ± 0.09	0.37	10.96 ± 0.18
13057979	0.82 ± 0.01	3.76 ± 0.09	0.39	10.56 ± 0.25

Table B.2 (cont'd)

Object Number	$R_{e,c}$ [kpc]	$n_{\rm Sérsic}^{\rm single}$	$q^{\rm single}$	$\log(M_{\rm dyn}/M_\odot)$
(1)	(2)	(3)	(4)	(5)
13058221	1.139 ± 0.008	4.79 ± 0.04	0.44	10.73 ± 0.14
13058803	2.94 ± 0.03	4.95 ± 0.04	0.83	11.42 ± 0.10
13064321	1.39 ± 0.02	3.62 ± 0.06	0.73	10.82 ± 0.18
13064634	1.10 ± 0.02	5.7 ± 0.1	0.3	10.97 ± 0.27
41032729	2.6 ± 0.2	5.4 ± 0.2	0.92	11.34 ± 0.24
42037703	2.2 ± 0.4	3.7 ± 0.5	0.72	11.24 ± 0.26
42029812	0.96 ± 0.02	2.7 ± 0.1	0.66	10.48 ± 0.29
42033566	2.7 ± 0.4	6.1 ± 0.6	0.48	11.42 ± 0.20
13101995	0.60 ± 0.01	3.19 ± 0.05	0.33	10.40 ± 0.25
11013870	0.92 ± 0.02	5.31 ± 0.09	0.2	10.55 ± 0.16
11019658	1.05 ± 0.04	5.7 ± 0.2	0.17	10.73 ± 0.22
31008760	0.89 ± 0.04	2.0 ± 0.2	0.25	10.46 ± 0.29
41019260	0.93 ± 0.03	3.5 ± 0.1	0.17	10.81 ± 0.30
41019373	1.54 ± 0.08	4.9 ± 0.3	0.35	10.88 ± 0.31
41020051	2.16 ± 0.04	2.99 ± 0.04	0.33	11.12 ± 0.20
41020361	4.0 ± 0.3	7.7 ± 0.3	0.81	11.61 ± 0.14

Note. — (1) DEEP2 identification number; (2) Circularized effective radius given by Equation 3.3; (3) Single-profile Sérsic index; (4) Axis ratio (b/a); (5) Log of the dynamical mass given by Equation 4.1

Table B.3. Photometric Properties of DEEP2 CQGs

Object Number (1)	K-correction [mag] (2)	$\log(M_*/M_\odot)$ (3)	M_{dyn}/M_* (4)
12004492	-0.306	10.27 ± 0.29	1.14 ± 0.46
12007960	-0.643	10.73 ± 0.27	1.28 ± 0.45
12015693	-0.791	10.14 ± 3.74	1.48 ± 5.55
12016013	-0.547	10.99 ± 0.03	1.82 ± 0.25
12016769	-0.489	10.76 ± 0.21	0.95 ± 0.27
12019899	-0.890	10.86 ± 0.65	1.69 ± 1.12
12019978	-0.676	10.99 ± 0.17	0.85 ± 0.19
12023935	-0.797	11.53 ± 0.44	0.53 ± 0.27
12024057	-0.678	11.04 ± 0.09	0.72 ± 0.12
12025292	-0.766	10.92 ± 0.26	0.62 ± 0.20
12028330	-0.774	10.92 ± 0.61	8.46 ± 5.39
12028633	-0.606	11.07 ± 0.12	1.26 ± 0.20
13010942	-0.590	10.90 ± 0.41	0.51 ± 0.24
13011281	-0.760	11.12 ± 0.35	1.82 ± 0.70
13011501	-0.965	10.77 ± 1.20	0.83 ± 1.03
13011780	-0.763	11.01 ± 0.28	0.72 ± 0.25
13011811	-0.540	10.70 ± 0.23	0.83 ± 0.23
13019286	-0.680	10.93 ± 0.12	1.87 ± 0.33
13019294	-0.806	10.82 ± 0.28	0.40 ± 0.15
13019956	-0.731	11.18 ± 0.28	3.65 ± 1.11
13025465	-0.599	10.84 ± 0.37	1.82 ± 0.74
13027468	-0.717	10.59 ± 1.63	0.55 ± 0.92
13033804	-0.687	10.90 ± 0.39	0.58 ± 0.26
13033944	-0.711	10.75 ± 0.36	0.93 ± 0.41
13033965	-0.695	10.86 ± 0.24	1.06 ± 0.30
13034447	-0.693	10.31 ± 0.20	4.19 ± 1.02
13034602	-0.652	11.29 ± 0.09	0.58 ± 0.07
13035280	-0.872	10.72 ± 0.53	1.21 ± 0.70
13041525	-0.954	10.34 ± 5.80	2.34 ± 13.59
13041606	-0.601	11.01 ± 0.11	1.70 ± 0.25
13042259	-0.719	10.53 ± 1.14	0.93 ± 1.07
13043062	-0.933	10.91 ± 0.19	1.44 ± 0.29
13049589	-0.538	10.12 ± 0.48	3.68 ± 1.87
13049865	-0.602	11.20 ± 0.11	1.63 ± 0.28
13057571	-0.599	10.78 ± 0.38	1.50 ± 0.63
13057979	-0.686	10.51 ± 0.48	1.13 ± 0.61

Table B.3 (cont'd)

Object Number (1)	K-correction [mag] (2)	$\log(M_*/M_\odot)$ (3)	M_{dyn}/M_* (4)
13058221	-0.531	10.51 ± 1.02	1.67 ± 1.73
13058803	-0.535	11.11 ± 0.14	2.02 ± 0.35
13064321	-0.588	10.35 ± 0.65	2.96 ± 1.99
13064634	-0.863	11.01 ± 0.44	0.91 ± 0.47
13101995	-0.409	10.92 ± 0.33	0.30 ± 0.13
11013870	-0.556	10.73 ± 0.39	0.66 ± 0.28
11019658	-0.405	10.74 ± 0.57	0.99 ± 0.60

Note. — (1) DEEP2 identification number; (2) Calculated K-correction (Equation 2.1); (3) Log of the calculated stellar mass based on a Kroupa IMF; (4) Dynamical mass to stellar mass ratio

Bibliography

[Abazajian et al., 2009] Abazajian, K. N., Adelman-McCarthy, J. K., Agüeros, M. A., Allam, S. S., Allende Prieto, C., An, D., Anderson, K. S. J., Anderson, S. F., Annis, J., Bahcall, N. A., and et al. (2009). The Seventh Data Release of the Sloan Digital Sky Survey. *ApJS*, 182:543–558.

[Barmby et al., 2008] Barmby, P., Huang, J.-S., Ashby, M. L. N., Eisenhardt, P. R. M., Fazio, G. G., Willner, S. P., and Wright, E. L. (2008). A Catalog of Mid-Infrared Sources in the Extended Groth Strip. *ApJS*, 177:431–445.

[Barro et al., 2013] Barro, G., Faber, S. M., Pérez-González, P. G., Koo, D. C., Williams, C. C., Kocevski, D. D., Trump, J. R., Mozena, M., McGrath, E., van der Wel, A., Wuyts, S., Bell, E. F., Croton, D. J., Ceverino, D., Dekel, A., Ashby, M. L. N., Cheung, E., Ferguson, H. C., Fontana, A., Fang, J., Giavalisco, M., Grogin, N. A., Guo, Y., Hathi, N. P., Hopkins, P. F., Huang, K.-H., Koekemoer, A. M., Kartaltepe, J. S., Lee, K.-S., Newman, J. A., Porter, L. A., Primack, J. R., Ryan, R. E., Rosario, D., Somerville, R. S., Salvato, M., and Hsu, L.-T. (2013). CANDELS: The Progenitors of Compact Quiescent Galaxies at z ˜ 2. *ApJ*, 765:104.

[Belli et al., 2014] Belli, S., Newman, A. B., Ellis, R. S., and Konidaris, N. P. (2014). MOSFIRE Absorption Line Spectroscopy of z >2 Quiescent Galaxies: Probing a Period of Rapid Size Growth. *ApJL*, 788:L29.

[Bennett et al., 2013] Bennett, C. L., Larson, D., Weiland, J. L., Jarosik, N., Hinshaw, G., Odegard, N., Smith, K. M., Hill, R. S., Gold, B., Halpern, M., Komatsu, E., Nolta, M. R., Page, L., Spergel, D. N., Wollack, E., Dunkley, J., Kogut, A., Limon, M., Meyer, S. S., Tucker, G. S., and Wright, E. L. (2013). VizieR Online Data Catalog: Nine-year WMAP point source catalogs (Bennett+, 2013). *VizieR Online Data Catalog*, 220:80020.

[Bezanson et al., 2012] Bezanson, R., van Dokkum, P., and Franx, M. (2012). Evolution of Quiescent and Star-forming Galaxies since z ˜ 1.5 as a Function of their Velocity Dispersions. *ApJ*, 760:62.

[Blain et al., 2004] Blain, A. W., Chapman, S. C., Smail, I., and Ivison, R. (2004). Clustering of Submillimeter-selected Galaxies. *ApJ*, 611:725–731.

[Bruce et al., 2012] Bruce, V. A., Dunlop, J. S., Cirasuolo, M., McLure, R. J., Targett, T. A., Bell, E. F., Croton, D. J., Dekel, A., Faber, S. M., Ferguson, H. C., Grogin, N. A., Kocevski, D. D., Koekemoer, A. M., Koo, D. C., Lai,

K., Lotz, J. M., McGrath, E. J., Newman, J. A., and van der Wel, A. (2012). The morphologies of massive galaxies at 1 <z <3 in the CANDELS-UDS field: compact bulges, and the rise and fall of massive discs. *MNRAS*, 427:1666–1701.

[Buitrago et al., 2008] Buitrago, F., Trujillo, I., Conselice, C. J., Bouwens, R. J., Dickinson, M., and Yan, H. (2008). Size Evolution of the Most Massive Galaxies at 1.7 <z <3 from GOODS NICMOS Survey Imaging. *ApJL*, 687:L61–L64.

[Bundy et al., 2006] Bundy, K., Ellis, R. S., Conselice, C. J., Taylor, J. E., Cooper, M. C., Willmer, C. N. A., Weiner, B. J., Coil, A. L., Noeske, K. G., and Eisenhardt, P. R. M. (2006). The Mass Assembly History of Field Galaxies: Detection of an Evolving Mass Limit for Star-Forming Galaxies. *ApJ*, 651:120–141.

[Capak et al., 2008] Capak, P., Carilli, C. L., Lee, N., Aldcroft, T., Aussel, H., Schinnerer, E., Wilson, G. W., Yun, M. S., Blain, A., Giavalisco, M., Ilbert, O., Kartaltepe, J., Lee, K.-S., McCracken, H., Mobasher, B., Salvato, M., Sasaki, S., Scott, K. S., Sheth, K., Shioya, Y., Thompson, D., Elvis, M., Sanders, D. B., Scoville, N. Z., and Tanaguchi, Y. (2008). Spectroscopic Confirmation of an Extreme Starburst at Redshift 4.547. *ApJL*, 681:L53–L56.

[Cappellari et al., 2006] Cappellari, M., Bacon, R., Bureau, M., Damen, M. C., Davies, R. L., de Zeeuw, P. T., Emsellem, E., Falcón-Barroso, J., Krajnović, D., Kuntschner, H., McDermid, R. M., Peletier, R. F., Sarzi, M., van den Bosch, R. C. E., and van de Ven, G. (2006). The SAURON project - IV. The mass-to-light ratio, the virial mass estimator and the Fundamental Plane of elliptical and lenticular galaxies. *MNRAS*, 366:1126–1150.

[Cappellari et al., 2009] Cappellari, M., di Serego Alighieri, S., Cimatti, A., Daddi, E., Renzini, A., Kurk, J. D., Cassata, P., Dickinson, M., Franceschini, A., Mignoli, M., Pozzetti, L., Rodighiero, G., Rosati, P., and Zamorani, G. (2009). Dynamical Masses of Early-Type Galaxies at z ˜ 2: Are they Truly Superdense? *ApJL*, 704:L34–L39.

[Cappellari et al., 2012] Cappellari, M., McDermid, R. M., Alatalo, K., Blitz, L., Bois, M., Bournaud, F., Bureau, M., Crocker, A. F., Davies, R. L., Davis, T. A., de Zeeuw, P. T., Duc, P.-A., Emsellem, E., Khochfar, S., Krajnović, D., Kuntschner, H., Lablanche, P.-Y., Morganti, R., Naab, T., Oosterloo, T., Sarzi, M., Scott, N., Serra, P., Weijmans, A.-M., and Young, L. M. (2012). Systematic variation of the stellar initial mass function in early-type galaxies. *Nature*, 484:485–488.

[Carilli et al., 2010] Carilli, C. L., Daddi, E., Riechers, D., Walter, F., Weiss, A., Dannerbauer, H., Morrison, G. E., Wagg, J., Davé, R., Elbaz, D., Stern, D., Dickinson, M., Krips, M., and Aravena, M. (2010). Imaging the Molecular Gas in a Submillimeter Galaxy at z = 4.05: Cold Mode Accretion or a Major Merger? *ApJ*, 714:1407–1417.

[Carollo et al., 2013] Carollo, C. M., Bschorr, T. J., Renzini, A., Lilly, S. J., Capak, P., Cibinel, A., Ilbert, O., Onodera, M., Scoville, N., Cameron, E., Mobasher, B., Sanders, D., and Taniguchi, Y. (2013). Newly Quenched Galaxies as the Cause for the Apparent Evolution in Average Size of the Population. *ApJ*, 773:112.

[Carrasco et al., 2010] Carrasco, E. R., Conselice, C. J., and Trujillo, I. (2010). Gemini K-band NIRI Adaptive Optics Observations of massive galaxies at 1 <z <2. *MNRAS*, 405:2253–2259.

[Casali et al., 2007] Casali, M., Adamson, A., Alves de Oliveira, C., Almaini, O., Burch, K., Chuter, T., Elliot, J., Folger, M., Foucaud, S., Hambly, N., Hastie, M., Henry, D., Hirst, P., Irwin, M., Ives, D., Lawrence, A., Laidlaw, K., Lee, D., Lewis, J., Lunney, D., McLay, S., Montgomery, D., Pickup, A., Read, M., Rees, N., Robson, I., Sekiguchi, K., Vick, A., Warren, S., and Woodward, B. (2007). The UKIRT wide-field camera. *A&A*, 467:777–784.

[Cassata et al., 2011] Cassata, P., Giavalisco, M., Guo, Y., Renzini, A., Ferguson, H., Koekemoer, A. M., Salimbeni, S., Scarlata, C., Grogin, N. A., Conselice, C. J., Dahlen, T., Lotz, J. M., Dickinson, M., and Lin, L. (2011). The Relative Abundance of Compact and Normal Massive Early-type Galaxies and Its Evolution from Redshift z ˜ 2 to the Present. *ApJ*, 743:96.

[Chilingarian et al., 2007a] Chilingarian, I., Prugniel, P., Sil'Chenko, O., and Koleva, M. (2007a). NBursts: Simultaneous Extraction of Internal Kinematics and Parametrized SFH from Integrated Light Spectra. In Vazdekis, A. and Peletier, R., editors, *IAU Symposium*, volume 241 of *IAU Symposium*, pages 175–176.

[Chilingarian et al., 2010] Chilingarian, I. V., Melchior, A.-L., and Zolotukhin, I. Y. (2010). Analytical approximations of K-corrections in optical and near-infrared bands. *MNRAS*, 405:1409–1420.

[Chilingarian et al., 2007b] Chilingarian, I. V., Prugniel, P., Sil'Chenko, O. K., and Afanasiev, V. L. (2007b). Kinematics and stellar populations of the dwarf elliptical galaxy IC 3653. *MNRAS*, 376:1033–1046.

[Chilingarian and Zolotukhin, 2012] Chilingarian, I. V. and Zolotukhin, I. Y. (2012). A universal ultraviolet-optical colour-colour-magnitude relation of galaxies. *MNRAS*, 419:1727–1739.

[Cimatti et al., 2008] Cimatti, A., Cassata, P., Pozzetti, L., Kurk, J., Mignoli, M., Renzini, A., Daddi, E., Bolzonella, M., Brusa, M., Rodighiero, G., Dickinson, M., Franceschini, A., Zamorani, G., Berta, S., Rosati, P., and Halliday, C. (2008). GMASS ultradeep spectroscopy of galaxies at z ˜ 2. II. Superdense passive galaxies: how did they form and evolve? *A&A*, 482:21–42.

[Coil et al., 2004] Coil, A. L., Newman, J. A., Kaiser, N., Davis, M., Ma, C.-P., Kocevski, D. D., and Koo, D. C. (2004). Evolution and Color Dependence of the Galaxy Angular Correlation Function: 350,000 Galaxies in 5 Square Degrees. *ApJ*, 617:765–781.

[Combes et al., 2012] Combes, F., Rex, M., Rawle, T. D., Egami, E., Boone, F., Smail, I., Richard, J., Ivison, R. J., Gurwell, M., Casey, C. M., Omont, A., Berciano Alba, A., Dessauges-Zavadsky, M., Edge, A. C., Fazio, G. G., Kneib, J.-P., Okabe, N., Pelló, R., Pérez-González, P. G., Schaerer, D., Smith, G. P., Swinbank, A. M., and van der Werf, P. (2012). A bright z = 5.2 lensed submillimeter galaxy in the field of Abell 773. HLSJ091828.6+514223. *A&A*, 538:L4.

[Conroy et al., 2013] Conroy, C., Dutton, A. A., Graves, G. J., Mendel, J. T., and van Dokkum, P. G. (2013). Dynamical versus Stellar Masses in Compact Early-type Galaxies: Further Evidence for Systematic Variation in the Stellar Initial Mass Function. *ApJL*, 776:L26.

[Cooper et al., 2012] Cooper, M. C., Newman, J. A., Davis, M., Finkbeiner, D. P., and Gerke, B. F. (2012). spec2d: DEEP2 DEIMOS Spectral Pipeline. Astrophysics Source Code Library.

[Coppin et al., 2008] Coppin, K. E. K., Swinbank, A. M., Neri, R., Cox, P., Alexander, D. M., Smail, I., Page, M. J., Stevens, J. A., Knudsen, K. K., Ivison, R. J., Beelen, A., Bertoldi, F., and Omont, A. (2008). Testing the evolutionary link between submillimetre galaxies and quasars: CO observations of QSOs at z ˜ 2. *MNRAS*, 389:45–62.

[Daddi et al., 2005] Daddi, E., Renzini, A., Pirzkal, N., Cimatti, A., Malhotra, S., Stiavelli, M., Xu, C., Pasquali, A., Rhoads, J. E., Brusa, M., di Serego Alighieri, S., Ferguson, H. C., Koekemoer, A. M., Moustakas, L. A., Panagia, N., and Windhorst, R. A. (2005). Passively Evolving Early-Type Galaxies at 1.4 <˜ z <˜ 2.5 in the Hubble Ultra Deep Field. *ApJ*, 626:680–697.

[Damjanov et al., 2013] Damjanov, I., Chilingarian, I., Hwang, H. S., and Geller, M. J. (2013). Discovery of Nine Intermediate-redshift Compact Quiescent Galaxies in the Sloan Digital Sky Survey. *ApJL*, 775:L48.

[Damjanov et al., 2014] Damjanov, I., Hwang, H. S., Geller, M. J., and Chilingarian, I. (2014). The Number Density of Quiescent Compact Galaxies at Intermediate Redshift. *ApJ*, 793:39.

[Damjanov et al., 2009] Damjanov, I., McCarthy, P. J., Abraham, R. G., Glazebrook, K., Yan, H., Mentuch, E., Le Borgne, D., Savaglio, S., Crampton, D., Murowinski, R., Juneau, S., Carlberg, R. G., Jørgensen, I., Roth, K., Chen, H.-W., and Marzke, R. O. (2009). Red Nuggets at z ˜ 1.5: Compact Passive Galaxies and the Formation of the Kormendy Relation. *ApJ*, 695:101–115.

[de Vaucouleurs, 1948] de Vaucouleurs, G. (1948). Recherches sur les Nebuleuses Extragalactiques. *Annales d'Astrophysique*, 11:247.

[Eggen et al., 1962] Eggen, O. J., Lynden-Bell, D., and Sandage, A. R. (1962). Evidence from the motions of old stars that the Galaxy collapsed. *ApJ*, 136:748.

[Faber et al., 2003] Faber, S. M., Phillips, A. C., Kibrick, R. I., Alcott, B., Allen, S. L., Burrous, J., Cantrall, T., Clarke, D., Coil, A. L., Cowley, D. J.,

Davis, M., Deich, W. T. S., Dietsch, K., Gilmore, D. K., Harper, C. A., Hilyard, D. F., Lewis, J. P., McVeigh, M., Newman, J., Osborne, J., Schiavon, R., Stover, R. J., Tucker, D., Wallace, V., Wei, M., Wirth, G., and Wright, C. A. (2003). The DEIMOS spectrograph for the Keck II Telescope: integration and testing. In Iye, M. and Moorwood, A. F. M., editors, *Instrument Design and Performance for Optical/Infrared Ground-based Telescopes*, volume 4841 of *Society of Photo-Optical Instrumentation Engineers (SPIE) Conference Series*, pages 1657–1669.

[Ferré-Mateu et al., 2012] Ferré-Mateu, A., Vazdekis, A., Trujillo, I., Sánchez-Blázquez, P., Ricciardelli, E., and de la Rosa, I. G. (2012). Young ages and other intriguing properties of massive compact galaxies in the local Universe. *MNRAS*, 423:632–646.

[Franx et al., 2008] Franx, M., van Dokkum, P. G., Schreiber, N. M. F., Wuyts, S., Labbé, I., and Toft, S. (2008). Structure and Star Formation in Galaxies out to z = 3: Evidence for Surface Density Dependent Evolution and Upsizing. *ApJ*, 688:770–788.

[Griffith et al., 2012] Griffith, R. L., Cooper, M. C., Newman, J. A., Moustakas, L. A., Stern, D., Comerford, J. M., Davis, M., Lotz, J. M., Barden, M., Conselice, C. J., Capak, P. L., Faber, S. M., Kirkpatrick, J. D., Koekemoer, A. M., Koo, D. C., Noeske, K. G., Scoville, N., Sheth, K., Shopbell, P., Willmer, C. N. A., and Weiner, B. (2012). The Advanced Camera for Surveys General Catalog: Structural Parameters for Approximately Half a Million Galaxies. *ApJS*, 200:9.

[Grogin et al., 2011] Grogin, N. A., Kocevski, D. D., Faber, S. M., Ferguson, H. C., Koekemoer, A. M., Riess, A. G., Acquaviva, V., Alexander, D. M., Almaini, O., Ashby, M. L. N., Barden, M., Bell, E. F., Bournaud, F., Brown, T. M., Caputi, K. I., Casertano, S., Cassata, P., Castellano, M., Challis, P., Chary, R.-R., Cheung, E., Cirasuolo, M., Conselice, C. J., Roshan Cooray, A., Croton, D. J., Daddi, E., Dahlen, T., Davé, R., de Mello, D. F., Dekel, A., Dickinson, M., Dolch, T., Donley, J. L., Dunlop, J. S., Dutton, A. A., Elbaz, D., Fazio, G. G., Filippenko, A. V., Finkelstein, S. L., Fontana, A., Gardner, J. P., Garnavich, P. M., Gawiser, E., Giavalisco, M., Grazian, A., Guo, Y., Hathi, N. P., Häussler, B., Hopkins, P. F., Huang, J.-S., Huang, K.-H., Jha, S. W., Kartaltepe, J. S., Kirshner, R. P., Koo, D. C., Lai, K., Lee, K.-S., Li, W., Lotz, J. M., Lucas, R. A., Madau, P., McCarthy, P. J., McGrath, E. J., McIntosh, D. H., McLure, R. J., Mobasher, B., Moustakas, L. A., Mozena, M., Nandra, K., Newman, J. A., Niemi, S.-M., Noeske, K. G., Papovich, C. J., Pentericci, L., Pope, A., Primack, J. R., Rajan, A., Ravindranath, S., Reddy, N. A., Renzini, A., Rix, H.-W., Robaina, A. R., Rodney, S. A., Rosario, D. J., Rosati, P., Salimbeni, S., Scarlata, C., Siana, B., Simard, L., Smidt, J., Somerville, R. S., Spinrad, H., Straughn, A. N., Strolger, L.-G., Telford, O., Teplitz, H. I., Trump, J. R., van der Wel, A., Villforth, C., Wechsler, R. H., Weiner, B. J., Wiklind, T., Wild, V., Wilson, G., Wuyts,

S., Yan, H.-J., and Yun, M. S. (2011). CANDELS: The Cosmic Assembly Near-infrared Deep Extragalactic Legacy Survey. *ApJS*, 197:35.

[Gwyn, 2012] Gwyn, S. D. J. (2012). The Canada-France-Hawaii Telescope Legacy Survey: Stacked Images and Catalogs. *AJ*, 143:38.

[Hambly et al., 2008] Hambly, N. C., Collins, R. S., Cross, N. J. G., Mann, R. G., Read, M. A., Sutorius, E. T. W., Bond, I., Bryant, J., Emerson, J. P., Lawrence, A., Rimoldini, L., Stewart, J. M., Williams, P. M., Adamson, A., Hirst, P., Dye, S., and Warren, S. J. (2008). The WFCAM Science Archive. *MNRAS*, 384:637–662.

[Hewett et al., 2006] Hewett, P. C., Warren, S. J., Leggett, S. K., and Hodgkin, S. T. (2006). The UKIRT Infrared Deep Sky Survey ZY JHK photometric system: passbands and synthetic colours. *MNRAS*, 367:454–468.

[Hogg, 1999] Hogg, D. W. (1999). Distance measures in cosmology. *ArXiv Astrophysics e-prints*.

[Hogg et al., 2002] Hogg, D. W., Baldry, I. K., Blanton, M. R., and Eisenstein, D. J. (2002). The K correction. *ArXiv Astrophysics e-prints*.

[Hopkins et al., 2006] Hopkins, P. F., Somerville, R. S., Hernquist, L., Cox, T. J., Robertson, B., and Li, Y. (2006). The Relation between Quasar and Merging Galaxy Luminosity Functions and the Merger-driven Star Formation History of the Universe. *ApJ*, 652:864–888.

[Hubble, 1958] Hubble, E. (1958). *The realm of the nebulae*.

[Hubble, 1936] Hubble, E. P. (1936). *Realm of the Nebulae*.

[Irwin, 2008] Irwin, M. J. (2008). Processing Wide Field Imaging Data. In Kaufer, A. and Kerber, F., editors, *2007 ESO Instrument Calibration Workshop*, page 541.

[Jester et al., 2005] Jester, S., Schneider, D. P., Richards, G. T., Green, R. F., Schmidt, M., Hall, P. B., Strauss, M. A., Vanden Berk, D. E., Stoughton, C., Gunn, J. E., Brinkmann, J., Kent, S. M., Smith, J. A., Tucker, D. L., and Yanny, B. (2005). The Sloan Digital Sky Survey View of the Palomar-Green Bright Quasar Survey. *AJ*, 130:873–895.

[Kniazev et al., 2002] Kniazev, A. Y., Grebel, E. K., Hao, L., and Strauss, M. A. (2002). A new extremely metal-poor galaxy discovered in the Sloan DIgital Sky Survey. In *Astronomische Gesellschaft Abstract Series*, volume 19 of *Astronomische Gesellschaft Abstract Series*, pages 106–106.

[Koekemoer et al., 2011] Koekemoer, A. M., Faber, S. M., Ferguson, H. C., Grogin, N. A., Kocevski, D. D., Koo, D. C., Lai, K., Lotz, J. M., Lucas, R. A., McGrath, E. J., Ogaz, S., Rajan, A., Riess, A. G., Rodney, S. A., Strolger, L., Casertano, S., Castellano, M., Dahlen, T., Dickinson, M., Dolch, T., Fontana, A., Giavalisco, M., Grazian, A., Guo, Y., Hathi, N. P., Huang, K.-H., van der Wel, A., Yan, H.-J., Acquaviva, V., Alexander, D. M., Almaini, O., Ashby, M. L. N., Barden, M., Bell, E. F., Bournaud, F., Brown, T. M.,

Caputi, K. I., Cassata, P., Challis, P. J., Chary, R.-R., Cheung, E., Cirasuolo, M., Conselice, C. J., Roshan Cooray, A., Croton, D. J., Daddi, E., Davé, R., de Mello, D. F., de Ravel, L., Dekel, A., Donley, J. L., Dunlop, J. S., Dutton, A. A., Elbaz, D., Fazio, G. G., Filippenko, A. V., Finkelstein, S. L., Frazer, C., Gardner, J. P., Garnavich, P. M., Gawiser, E., Gruetzbauch, R., Hartley, W. G., Häussler, B., Herrington, J., Hopkins, P. F., Huang, J.-S., Jha, S. W., Johnson, A., Kartaltepe, J. S., Khostovan, A. A., Kirshner, R. P., Lani, C., Lee, K.-S., Li, W., Madau, P., McCarthy, P. J., McIntosh, D. H., McLure, R. J., McPartland, C., Mobasher, B., Moreira, H., Mortlock, A., Moustakas, L. A., Mozena, M., Nandra, K., Newman, J. A., Nielsen, J. L., Niemi, S., Noeske, K. G., Papovich, C. J., Pentericci, L., Pope, A., Primack, J. R., Ravindranath, S., Reddy, N. A., Renzini, A., Rix, H.-W., Robaina, A. R., Rosario, D. J., Rosati, P., Salimbeni, S., Scarlata, C., Siana, B., Simard, L., Smidt, J., Snyder, D., Somerville, R. S., Spinrad, H., Straughn, A. N., Telford, O., Teplitz, H. I., Trump, J. R., Vargas, C., Villforth, C., Wagner, C. R., Wandro, P., Wechsler, R. H., Weiner, B. J., Wiklind, T., Wild, V., Wilson, G., Wuyts, S., and Yun, M. S. (2011). CANDELS: The Cosmic Assembly Near-infrared Deep Extragalactic Legacy SurveyThe Hubble Space Telescope Observations, Imaging Data Products, and Mosaics. *ApJS*, 197:36.

[Krist et al., 2011] Krist, J. E., Hook, R. N., and Stoehr, F. (2011). 20 years of Hubble Space Telescope optical modeling using Tiny Tim. In *Society of Photo-Optical Instrumentation Engineers (SPIE) Conference Series*, volume 8127 of *Society of Photo-Optical Instrumentation Engineers (SPIE) Conference Series*, page 0.

[Krogager et al., 2014] Krogager, J.-K., Zirm, A. W., Toft, S., Man, A., and Brammer, G. (2014). A Spectroscopic Sample of Massive, Quiescent z ˜ 2 Galaxies: Implications for the Evolution of the Mass-Size Relation. *ApJ*, 797:17.

[Kroupa, 2002] Kroupa, P. (2002). The Initial Mass Function of Stars: Evidence for Uniformity in Variable Systems. *Science*, 295:82–91.

[Lawrence et al., 2007] Lawrence, A., Warren, S. J., Almaini, O., Edge, A. C., Hambly, N. C., Jameson, R. F., Lucas, P., Casali, M., Adamson, A., Dye, S., Emerson, J. P., Foucaud, S., Hewett, P., Hirst, P., Hodgkin, S. T., Irwin, M. J., Lodieu, N., McMahon, R. G., Simpson, C., Smail, I., Mortlock, D., and Folger, M. (2007). The UKIRT Infrared Deep Sky Survey (UKIDSS). *MNRAS*, 379:1599–1617.

[Le Borgne et al., 2004] Le Borgne, D., Rocca-Volmerange, B., Prugniel, P., Lançon, A., Fioc, M., and Soubiran, C. (2004). Evolutionary synthesis of galaxies at high spectral resolution with the code PEGASE-HR. Metallicity and age tracers. *A&A*, 425:881–897.

[Lemson and Virgo Consortium, 2006] Lemson, G. and Virgo Consortium, t. (2006). Halo and Galaxy Formation Histories from the Millennium Simulation: Public release of a VO-oriented and SQL-queryable database for

studying the evolution of galaxies in the LambdaCDM cosmogony. *ArXiv Astrophysics e-prints*.

[Lintott et al., 2008] Lintott, C. J., Schawinski, K., Slosar, A., Land, K., Bamford, S., Thomas, D., Raddick, M. J., Nichol, R. C., Szalay, A., Andreescu, D., Murray, P., and Vandenberg, J. (2008). Galaxy Zoo: morphologies derived from visual inspection of galaxies from the Sloan Digital Sky Survey. *MNRAS*, 389:1179–1189.

[López-Sanjuan et al., 2012] López-Sanjuan, C., Le Fèvre, O., Ilbert, O., Tasca, L. A. M., Bridge, C., Cucciati, O., Kampczyk, P., Pozzetti, L., Xu, C. K., Carollo, C. M., Contini, T., Kneib, J.-P., Lilly, S. J., Mainieri, V., Renzini, A., Sanders, D., Scodeggio, M., Scoville, N. Z., Taniguchi, Y., Zamorani, G., Aussel, H., Bardelli, S., Bolzonella, M., Bongiorno, A., Capak, P., Caputi, K., de la Torre, S., de Ravel, L., Franzetti, P., Garilli, B., Iovino, A., Knobel, C., Kovač, K., Lamareille, F., Le Borgne, J.-F., Le Brun, V., Le Floc'h, E., Maier, C., McCracken, H. J., Mignoli, M., Pelló, R., Peng, Y., Pérez-Montero, E., Presotto, V., Ricciardelli, E., Salvato, M., Silverman, J. D., Tanaka, M., Tresse, L., Vergani, D., Zucca, E., Barnes, L., Bordoloi, R., Cappi, A., Cimatti, A., Coppa, G., Koekemoer, A., Liu, C. T., Moresco, M., Nair, P., Oesch, P., Schawinski, K., and Welikala, N. (2012). The dominant role of mergers in the size evolution of massive early-type galaxies since z ˜ 1. *A&A*, 548:A7.

[Maraston, 2003] Maraston, C. (2003). Stellar Population Models. In Kissler-Patig, M., editor, *Extragalactic Globular Cluster Systems*, page 237.

[Maraston and Strömbäck, 2011] Maraston, C. and Strömbäck, G. (2011). Stellar population models at high spectral resolution. *MNRAS*, 418:2785–2811.

[Marchesini et al., 2014] Marchesini, D., Muzzin, A., Stefanon, M., Franx, M., Brammer, G. G., Marsan, C. Z., Vulcani, B., Fynbo, J. P. U., Milvang-Jensen, B., Dunlop, J. S., and Buitrago, F. (2014). The Progenitors of Local Ultra-massive Galaxies Across Cosmic Time: From Dusty Star-bursting to Quiescent Stellar Populations. *ApJ*, 794:65.

[Martin et al., 2005] Martin, D. C., Fanson, J., Schiminovich, D., Morrissey, P., Friedman, P. G., Barlow, T. A., Conrow, T., Grange, R., Jelinsky, P. N., Milliard, B., Siegmund, O. H. W., Bianchi, L., Byun, Y.-I., Donas, J., Forster, K., Heckman, T. M., Lee, Y.-W., Madore, B. F., Malina, R. F., Neff, S. G., Rich, R. M., Small, T., Surber, F., Szalay, A. S., Welsh, B., and Wyder, T. K. (2005). The Galaxy Evolution Explorer: A Space Ultraviolet Survey Mission. *ApJL*, 619:L1–L6.

[Naab et al., 2009] Naab, T., Johansson, P. H., and Ostriker, J. P. (2009). Minor Mergers and the Size Evolution of Elliptical Galaxies. *ApJL*, 699:L178–L182.

[Naab et al., 2007] Naab, T., Johansson, P. H., Ostriker, J. P., and Efstathiou, G. (2007). Formation of Early-Type Galaxies from Cosmological Initial Conditions. *ApJ*, 658:710–720.

[Newman et al., 2012] Newman, A. B., Ellis, R. S., Bundy, K., and Treu, T. (2012). Can Minor Merging Account for the Size Growth of Quiescent Galaxies? New Results from the CANDELS Survey. *ApJ*, 746:162.

[Newman et al., 2010] Newman, A. B., Ellis, R. S., Treu, T., and Bundy, K. (2010). Keck Spectroscopy of z >1 Field Spheroidals: Dynamical Constraints on the Growth Rate of Red "Nuggets". *ApJL*, 717:L103–L107.

[Newman et al., 2013] Newman, J. A., Cooper, M. C., Davis, M., Faber, S. M., Coil, A. L., Guhathakurta, P., Koo, D. C., Phillips, A. C., Conroy, C., Dutton, A. A., Finkbeiner, D. P., Gerke, B. F., Rosario, D. J., Weiner, B. J., Willmer, C. N. A., Yan, R., Harker, J. J., Kassin, S. A., Konidaris, N. P., Lai, K., Madgwick, D. S., Noeske, K. G., Wirth, G. D., Connolly, A. J., Kaiser, N., Kirby, E. N., Lemaux, B. C., Lin, L., Lotz, J. M., Luppino, G. A., Marinoni, C., Matthews, D. J., Metevier, A., and Schiavon, R. P. (2013). The DEEP2 Galaxy Redshift Survey: Design, Observations, Data Reduction, and Redshifts. *ApJS*, 208:5.

[Onodera et al., 2012] Onodera, M., Renzini, A., Carollo, M., Cappellari, M., Mancini, C., Strazzullo, V., Daddi, E., Arimoto, N., Gobat, R., Yamada, Y., McCracken, H. J., Ilbert, O., Capak, P., Cimatti, A., Giavalisco, M., Koekemoer, A. M., Kong, X., Lilly, S., Motohara, K., Ohta, K., Sanders, D. B., Scoville, N., Tamura, N., and Taniguchi, Y. (2012). Deep Near-infrared Spectroscopy of Passively Evolving Galaxies at z $>\tilde{}$ 1.4. *ApJ*, 755:26.

[Oogi and Habe, 2013] Oogi, T. and Habe, A. (2013). Dry minor mergers and size evolution of high-z compact massive early-type galaxies. *MNRAS*, 428:641–657.

[Oser et al., 2012] Oser, L., Naab, T., Ostriker, J. P., and Johansson, P. H. (2012). The Cosmological Size and Velocity Dispersion Evolution of Massive Early-type Galaxies. *ApJ*, 744:63.

[Peng et al., 2002] Peng, C. Y., Ho, L. C., Impey, C. D., and Rix, H.-W. (2002). Detailed Structural Decomposition of Galaxy Images. *AJ*, 124:266–293.

[Poggianti et al., 2013] Poggianti, B. M., Moretti, A., Calvi, R., D'Onofrio, M., Valentinuzzi, T., Fritz, J., and Renzini, A. (2013). The Evolution of the Number Density of Compact Galaxies. *ApJ*, 777:125.

[Press and Teukolsky, 1997] Press, W. H. and Teukolsky, S. A. (1997). Numerical Recipes: Does This Paradigm Have a Future? *Computers in Physics*, 11:416.

[Quilis and Trujillo, 2013] Quilis, V. and Trujillo, I. (2013). Expected Number of Massive Galaxy Relics in the Present Day Universe. *ApJL*, 773:L8.

[Riechers et al., 2010] Riechers, D. A., Capak, P. L., Carilli, C. L., Cox, P., Neri, R., Scoville, N. Z., Schinnerer, E., Bertoldi, F., and Yan, L. (2010). A Massive Molecular Gas Reservoir in the z = 5.3 Submillimeter Galaxy AzTEC-3. *ApJL*, 720:L131–L136.

[Salpeter, 1955] Salpeter, E. E. (1955). The Luminosity Function and Stellar Evolution. *ApJ*, 121:161.

[Sánchez-Blázquez et al., 2006] Sánchez-Blázquez, P., Peletier, R. F., Jiménez-Vicente, J., Cardiel, N., Cenarro, A. J., Falcón-Barroso, J., Gorgas, J., Selam, S., and Vazdekis, A. (2006). Medium-resolution Isaac Newton Telescope library of empirical spectra. *MNRAS*, 371:703–718.

[Sanders et al., 1988] Sanders, D. B., Soifer, B. T., Elias, J. H., Madore, B. F., Matthews, K., Neugebauer, G., and Scoville, N. Z. (1988). Ultraluminous infrared galaxies and the origin of quasars. *ApJ*, 325:74–91.

[Saracco et al., 2011] Saracco, P., Longhetti, M., and Gargiulo, A. (2011). Constraining the star formation and the assembly histories of normal and compact early-type galaxies at 1 <z <2. *MNRAS*, 412:2707–2716.

[Saulder et al., 2013] Saulder, C., Mieske, S., Zeilinger, W. W., and Chilingarian, I. (2013). Calibrating the fundamental plane with SDSS DR8 data. *A&A*, 557:A21.

[Schinnerer et al., 2008] Schinnerer, E., Carilli, C. L., Capak, P., Martinez-Sansigre, A., Scoville, N. Z., Smolčić, V., Taniguchi, Y., Yun, M. S., Bertoldi, F., Le Fevre, O., and de Ravel, L. (2008). Molecular Gas in a Submillimeter Galaxy at z = 4.5: Evidence for a Major Merger at 1 Billion Years after the Big Bang. *ApJL*, 689:L5–L8.

[Sersic, 1968] Sersic, J. L. (1968). *Atlas de galaxias australes*.

[Simard et al., 2011] Simard, L., Mendel, J. T., Patton, D. R., Ellison, S. L., and McConnachie, A. W. (2011). A Catalog of Bulge+disk Decompositions and Updated Photometry for 1.12 Million Galaxies in the Sloan Digital Sky Survey. *ApJS*, 196:11.

[Springel et al., 2006] Springel, V., Frenk, C. S., and White, S. D. M. (2006). The large-scale structure of the Universe. *Nature*, 440:1137–1144.

[Stetson, 1987] Stetson, P. B. (1987). DAOPHOT - A computer program for crowded-field stellar photometry. *PASP*, 99:191–222.

[Strazzullo et al., 2010] Strazzullo, V., Rosati, P., Pannella, M., Gobat, R., Santos, J. S., Nonino, M., Demarco, R., Lidman, C., Tanaka, M., Mullis, C. R., Nuñez, C., Rettura, A., Jee, M. J., Böhringer, H., Bender, R., Bouwens, R. J., Dawson, K., Fassbender, R., Franx, M., Perlmutter, S., and Postman, M. (2010). Cluster galaxies in XMMU J2235-2557: galaxy population properties in most massive environments at z ˜ 1.4. *A&A*, 524:A17.

[Szomoru et al., 2012] Szomoru, D., Franx, M., and van Dokkum, P. G. (2012). Sizes and Surface Brightness Profiles of Quiescent Galaxies at z ˜ 2. *ApJ*, 749:121.

[Tacconi et al., 2006] Tacconi, L. J., Neri, R., Chapman, S. C., Genzel, R., Smail, I., Ivison, R. J., Bertoldi, F., Blain, A., Cox, P., Greve, T., and Omont, A. (2006). High-Resolution Millimeter Imaging of Submillimeter Galaxies. *ApJ*, 640:228–240.

[Taylor et al., 2010] Taylor, E. N., Franx, M., Glazebrook, K., Brinchmann, J., van der Wel, A., and van Dokkum, P. G. (2010). On the Dearth of Compact, Massive, Red Sequence Galaxies in the Local Universe. *ApJ*, 720:723–741.

[Toft et al., 2012] Toft, S., Gallazzi, A., Zirm, A., Wold, M., Zibetti, S., Grillo, C., and Man, A. (2012). Deep Absorption Line Studies of Quiescent Galaxies at z ˜ 2: The Dynamical-mass-Size Relation and First Constraints on the Fundamental Plane. *ApJ*, 754:3.

[Toft et al., 2014] Toft, S., Smolčić, V., Magnelli, B., Karim, A., Zirm, A., Michalowski, M., Capak, P., Sheth, K., Schawinski, K., Krogager, J.-K., Wuyts, S., Sanders, D., Man, A. W. S., Lutz, D., Staguhn, J., Berta, S., Mccracken, H., Krpan, J., and Riechers, D. (2014). Submillimeter Galaxies as Progenitors of Compact Quiescent Galaxies. *ApJ*, 782:68.

[Toft et al., 2007] Toft, S., van Dokkum, P., Franx, M., Labbe, I., Förster Schreiber, N. M., Wuyts, S., Webb, T., Rudnick, G., Zirm, A., Kriek, M., van der Werf, P., Blakeslee, J. P., Illingworth, G., Rix, H.-W., Papovich, C., and Moorwood, A. (2007). Hubble Space Telescope and Spitzer Imaging of Red and Blue Galaxies at z ˜ 2.5: A Correlation between Size and Star Formation Activity from Compact Quiescent Galaxies to Extended Star-forming Galaxies. *ApJ*, 671:285–302.

[Toomre, 1977] Toomre, A. (1977). Mergers and Some Consequences. In Tinsley, B. M. and Larson, D. Campbell, R. B. G., editors, *Evolution of Galaxies and Stellar Populations*, page 401.

[Trujillo et al., 2009] Trujillo, I., Cenarro, A. J., de Lorenzo-Cáceres, A., Vazdekis, A., de la Rosa, I. G., and Cava, A. (2009). Superdense Massive Galaxies in the Nearby Universe. *ApJL*, 692:L118–L122.

[Trujillo et al., 2006] Trujillo, I., Förster Schreiber, N. M., Rudnick, G., Barden, M., Franx, M., Rix, H.-W., Caldwell, J. A. R., McIntosh, D. H., Toft, S., Häussler, B., Zirm, A., van Dokkum, P. G., Labbé, I., Moorwood, A., Röttgering, H., van der Wel, A., van der Werf, P., and van Starkenburg, L. (2006). The Size Evolution of Galaxies since z˜3: Combining SDSS, GEMS, and FIRES. *ApJ*, 650:18–41.

[van de Sande et al., 2013] van de Sande, J., Kriek, M., Franx, M., van Dokkum, P. G., Bezanson, R., Bouwens, R. J., Quadri, R. F., Rix, H.-W., and Skelton, R. E. (2013). Stellar Kinematics of z ˜ 2 Galaxies and the Inside-out Growth of Quiescent Galaxies. *ApJ*, 771:85.

[van der Wel et al., 2012] van der Wel, A., Bell, E. F., Häussler, B., McGrath, E. J., Chang, Y.-Y., Guo, Y., McIntosh, D. H., Rix, H.-W., Barden, M., Cheung, E., Faber, S. M., Ferguson, H. C., Galametz, A., Grogin, N. A., Hartley, W., Kartaltepe, J. S., Kocevski, D. D., Koekemoer, A. M., Lotz, J., Mozena, M., Peth, M. A., and Peng, C. Y. (2012). Structural Parameters of Galaxies in CANDELS. *ApJS*, 203:24.

[van der Wel et al., 2014] van der Wel, A., Franx, M., van Dokkum, P. G., Skelton, R. E., Momcheva, I. G., Whitaker, K. E., Brammer, G. B., Bell, E. F.,

Rix, H.-W., Wuyts, S., Ferguson, H. C., Holden, B. P., Barro, G., Koekemoer, A. M., Chang, Y.-Y., McGrath, E. J., Häussler, B., Dekel, A., Behroozi, P., Fumagalli, M., Leja, J., Lundgren, B. F., Maseda, M. V., Nelson, E. J., Wake, D. A., Patel, S. G., Labbé, I., Faber, S. M., Grogin, N. A., and Kocevski, D. D. (2014). 3D-HST+CANDELS: The Evolution of the Galaxy Size-Mass Distribution since z = 3. *ApJ*, 788:28.

[van der Wel et al., 2008] van der Wel, A., Holden, B. P., Zirm, A. W., Franx, M., Rettura, A., Illingworth, G. D., and Ford, H. C. (2008). Recent Structural Evolution of Early-Type Galaxies: Size Growth from z = 1 to z = 0. *ApJ*, 688:48–58.

[van der Wel et al., 2009] van der Wel, A., Rix, H.-W., Holden, B. P., Bell, E. F., and Robaina, A. R. (2009). Major Merging: The Way to Make a Massive, Passive Galaxy. *ApJL*, 706:L120–L123.

[van der Wel et al., 2011] van der Wel, A., Rix, H.-W., Wuyts, S., McGrath, E. J., Koekemoer, A. M., Bell, E. F., Holden, B. P., Robaina, A. R., and McIntosh, D. H. (2011). The Majority of Compact Massive Galaxies at z ˜ 2 are Disk Dominated. *ApJ*, 730:38.

[van Dokkum et al., 2008] van Dokkum, P. G., Franx, M., Kriek, M., Holden, B., Illingworth, G. D., Magee, D., Bouwens, R., Marchesini, D., Quadri, R., Rudnick, G., Taylor, E. N., and Toft, S. (2008). Confirmation of the Remarkable Compactness of Massive Quiescent Galaxies at z ˜ 2.3: Early-Type Galaxies Did not Form in a Simple Monolithic Collapse. *ApJL*, 677:L5–L8.

[van Dokkum et al., 2009] van Dokkum, P. G., Kriek, M., and Franx, M. (2009). A high stellar velocity dispersion for a compact massive galaxy at redshift z = 2.186. *Nature*, 460:717–719.

[Whitaker et al., 2011] Whitaker, K. E., Labbé, I., van Dokkum, P. G., Brammer, G., Kriek, M., Marchesini, D., Quadri, R. F., Franx, M., Muzzin, A., Williams, R. J., Bezanson, R., Illingworth, G. D., Lee, K.-S., Lundgren, B., Nelson, E. J., Rudnick, G., Tal, T., and Wake, D. A. (2011). The NEWFIRM Medium-band Survey: Photometric Catalogs, Redshifts, and the Bimodal Color Distribution of Galaxies out to z ˜ 3. *ApJ*, 735:86.

[Willett et al., 2013] Willett, K. W., Lintott, C. J., Bamford, S. P., Masters, K. L., Simmons, B. D., Casteels, K. R. V., Edmondson, E. M., Fortson, L. F., Kaviraj, S., Keel, W. C., Melvin, T., Nichol, R. C., Raddick, M. J., Schawinski, K., Simpson, R. J., Skibba, R. A., Smith, A. M., and Thomas, D. (2013). Galaxy Zoo 2: detailed morphological classifications for 304 122 galaxies from the Sloan Digital Sky Survey. *MNRAS*, 435:2835–2860.

[Williams et al., 2014] Williams, C. C., Giavalisco, M., Cassata, P., Tundo, E., Wiklind, T., Guo, Y., Lee, B., Barro, G., Wuyts, S., Bell, E. F., Conselice, C. J., Dekel, A., Faber, S. M., Ferguson, H. C., Grogin, N., Hathi, N., Huang, K.-H., Kocevski, D., Koekemoer, A., Koo, D. C., Ravindranath, S., and

Salimbeni, S. (2014). The Progenitors of the Compact Early-type Galaxies at High Redshift. *ApJ*, 780:1.

[Willmer et al., 2006] Willmer, C. N. A., Faber, S. M., Koo, D. C., Weiner, B. J., Newman, J. A., Coil, A. L., Connolly, A. J., Conroy, C., Cooper, M. C., Davis, M., Finkbeiner, D. P., Gerke, B. F., Guhathakurta, P., Harker, J., Kaiser, N., Kassin, S., Konidaris, N. P., Lin, L., Luppino, G., Madgwick, D. S., Noeske, K. G., Phillips, A. C., and Yan, R. (2006). The Deep Evolutionary Exploratory Probe 2 Galaxy Redshift Survey: The Galaxy Luminosity Function to z˜1. *ApJ*, 647:853–873.

[Wuyts et al., 2010] Wuyts, S., Cox, T. J., Hayward, C. C., Franx, M., Hernquist, L., Hopkins, P. F., Jonsson, P., and van Dokkum, P. G. (2010). On Sizes, Kinematics, M/L Gradients, and Light Profiles of Massive Compact Galaxies at z ˜ 2. *ApJ*, 722:1666–1684.

[Yun et al., 2012] Yun, M. S., Scott, K. S., Guo, Y., Aretxaga, I., Giavalisco, M., Austermann, J. E., Capak, P., Chen, Y., Ezawa, H., Hatsukade, B., Hughes, D. H., Iono, D., Johnson, S., Kawabe, R., Kohno, K., Lowenthal, J., Miller, N., Morrison, G., Oshima, T., Perera, T. A., Salvato, M., Silverman, J., Tamura, Y., Williams, C. C., and Wilson, G. W. (2012). Deep 1.1 mm-wavelength imaging of the GOODS-S field by AzTEC/ASTE - II. Redshift distribution and nature of the submillimetre galaxy population. *MNRAS*, 420:957–985.